Fundamental Studies of Dust Fouling and Mitigation Approaches for PV Modules

BY

Husam Walwil

A Thesis Presented to the

DEANSHIP OF GRADUATE STUDIES

KING FAHD UNIVERSITY OF PETROLEUM & MINERALS

DHAHRAN, SAUDI ARABIA

In Partial Fulfillment of the
Requirements for the Degree of

MASTER OF SCIENCE

In

MECHANICAL ENGINEERING

JAN-2014

KING FAHD UNIVERSITY OF PETROLEUM & MINERALS

DHAHRAN- 31261, SAUDI ARABIA

DEANSHIP OF GRADUATE STUDIES

This thesis, written by **Husam Mohammad Walwil** under the direction his thesis advisor and approved by his thesis committee, has been presented and accepted by the Dean of Graduate Studies, in partial fulfillment of the requirements for the degree of **MASTER OF SCIENCE IN MECHANICAL ENGINEERING.**

Dr. Syed Said
(Advisor)

Dr. Zuhair Gasem
Department Chairman

Dr. Nasser Al-Aqeeli
(Member)

Dr. Salam A. Zummo
Dean of Graduate Studies

Dr. Kamal Youcef-Toumi
(Member)

14/1/14

Date

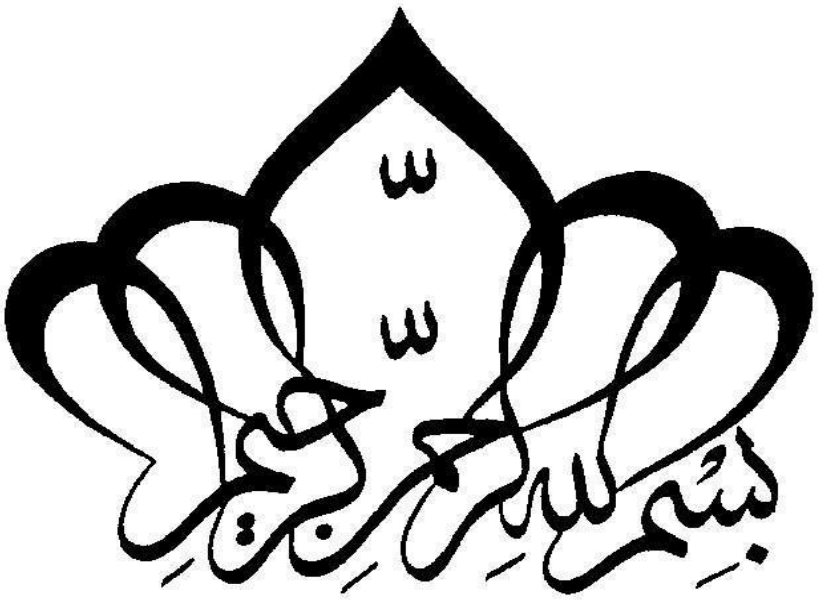

"قل إن صلاتي ونسكي ومحياي ومماتي لله رب

العالمين لا شريك له وبذلك أمرت وأنا أول المسلمين"

In the name of Allah, the Most Gracious and the Most Merciful

To my lovely parents, sisters, and brothers…

ACKNOWLEDGMENTS

All praise and thanks are due to Almighty Allah. He bestowed upon me health, knowledge and patience to complete this work.

I acknowledge, with deep gratitude and appreciation, the encouragement, Valuable time and continuous guidance given to me by my thesis advisor, Dr. Syed Said. I am highly grateful to my thesis committee members Dr. Kamal Youcef-Toumi (MIT) and Dr. Nasser Al-Aqeeli (KFUPM) for their valuable guidance, suggestions and motivation. Also, I am highly grateful to Dr. Kripa Varanasi for his valuable guidance, suggestions and motivation. Thanks to all KFUPM, MIT and Harvard lab's technicians, engineers for their help and guidance in conducting some of experimental works related the study. Acknowledgement is due to KFUPM for the support extended towards my research and for granting me the opportunity to pursue graduate studies. My heartfelt thanks are due to my Family (mother, sisters and brothers) for their prayers, guidance, and moral support throughout my academic life. Finally, special thanks are due to my senior colleagues at KFUPM for their Help and prayers.

TABLE OF CONTENTS

LIST OF TABLES

LIST OF FIGURES

LIST OF ABBREVIATIONS

γ_{sl}	:	Interfacial energies of solid-liquid
γ_{sv}	:	Interfacial energies of solid-gas
γ_{lv}	:	Interfacial energies of liquid-gas
CA	:	Contact angle
θ_{Rough}	:	Contact angle on rough surface
θ_{Flat}	:	Contact angle on flat surface
$\emptyset_s$	:	Fractions of solid contacting the liquid
$\emptyset_v$	:	Fractions of air contacting the liquid
θ_c	:	Critical angle
CAH	:	Contact angle hysteresis
γ_l	:	Liquid surface tension
FF	:	Fill Factor
Pmax	:	Maximum power rating
Voc	:	Open circuit voltage
Isc	:	Short circuit current
Vmp	:	Maximum power voltage
Imp	:	Maximum power current
A	:	Temperature coefficient of current
B	:	Temperature coefficient of voltage
RH	:	Relative Humidity
Ca	:	Capillary Number

LFM	:	Lateral Force Microscopy
SEM	:	Scanning Electron Microscope
EDS	:	Energy Dispersive Spectroscopy
XRF	:	X-Ray Fluorescence
XRD	:	X-Ray Diffraction
AFM	:	Atomic Force Microscopic
MV	:	Mean Volume Diameter
MA	:	Mean Area Diameter
MN	:	Mean Number Diameter
Ra	:	Average Roughness
Rq	:	Root mean square Roughness
Ski	:	Skewness
Kg	:	Kurtosis
ΔP	:	Laplace Pressure
F_s	:	Surface Tension Force
F_P	:	Laplace Force
W_I	:	Work of adhesion
F_h	:	Hydrostatic Force
$\bar{P}$	:	Hydrostatic pressure at centroid point
τ_a	:	Average shear strengths of the dry contact
τ_l	:	Average shear strengths of the liquid film
A	:	Fraction of un-lubricated area.

ABSTRACT

Full Name : Husam Mohammad Wahid Walwil

Thesis Title : Fundamental Studies of Dust Fouling and Mitigation Approaches for PV Modules

Major Field : Mechanical Engineering

Date of Degree : Jan 2014

The Kingdom of Saudi Arabia (KSA) is rich in resources and is a rapidly developing country. Its need for electrical power is growing at an annual average rate of 10%. KSA falls within solar belt, which avail a large opportunity and great potential for utilizing solar energy to meet some of the growing electrical energy demand. Realizing this fact, the KSA have established King Abdullah City for Atomic and Renewable Energy (KA-CARE). KA-CARE has announced an ambitious plan for solar energy utilization during the coming 15 years. The plan includes installation of 1.4 GW worth of PV system during the coming 4 years. Also more than 20MW of PV system have already been installed and in operation. One of the major challenges for effective utilization of solar energy systems in the Gulf region and hence KSA is the dust fouling on the surface of PV modules glass cover. Therefore; this study focuses on understanding the nature of dust fouling effects on PV modules performance and potential mitigation techniques. A number of PV modules were tested at outdoor conditions inside KFUPM campus. The average PV module power reduction due to dust accumulation was about 20% after 5 weeks of exposure without cleaning. It is observed that anti-reflective glass enhances the power output of modules, at the same time it relatively reduces the amount of dust accumulation. The accumulated dust particles have irregular and various forms but in general tend to be spherical in shape. Analysis of the chemical composition of

accumulated dust samples indicated that oxygen is the highest concentration followed by calcium, and silicon elements. Calcite and quartz compounds occupied more than 50% of the dust particles. Most of particles have a diameter less 2μm with presence of few large particles (≥10μm). In an attempt to look into potential mitigating techniques; dry and wet hydrophobic surfaces were synthesized. Since surface adhesion properties play the big role in the amount of dust accumulation; silica particle adhesion and friction properties were measured on both dry and wet hydrophobic surfaces using colloidal probe technology. Systematic silica particle-adhesion measurements indicated that the vertical particle-adhesion force strength either on wet or dry hydrophobic surfaces is dependent on texture and decreases with increasing spaces between the texture posts. Also, measured results indicated that silica particle vertical adhesion strength on lubricant impregnated textured silicon surfaces is larger than those on dry textured surfaces. Qualitative friction measurements indicated that LIS showed lower friction properties compared to dry surfaces. At high humidity level dry hydrophobic surfaces showed a drastic increase in the vertical adhesion. On the contrary, it was found out that humidity or vapor condensation doesn't affect the adhesion properties of LIS.

ملخص الرسالة

الاسم الكامل: حسام محمد وحيد ولويل

عنوان الرسالة:دراسات عن تأثير تراكم الغبار على أداء الوحدات الفولتوضوئية و طرق التخلص منها

التخصص:الهندسة الميكانيكية

تاريخ الدرجة العلمية: يناير 2014

تعد المملكة االعربية السعودية الدولة الاكثر استهلاكا للطاقة الكهربائية مقارنة بالدول المجاورة لها في الشرق الأوسط , حيث يقدر معدل النمو في المملكة بحوالي 10% سنويا. في الوقت ذاته تقع المملكة ضمن الحزام الشمسي للكرة الأرضية و هذا بدوره يكسبها غناً في مصادر الطاقة المتجددة و بالأخص الطاقة الشمسية منها. و من أجل الاستفادة من الطاقة الشمسية أعلنت عدد من الخطط المتضمنة على بناء أنظمة توليد طاقة كهربائية من الطاقة الشمسية. تعد أنظمة الوحدات الفولتوضوئية من الأنظمة الأمثل للتحويل المباشر للطاقة الشمسية؛ ولهذا وضعت مدينة الملك عبد الله للطاقة المتجددة و الذرية خطةً لبناء ما يقارب 1,4 جيجا وات خلال الأربع سنوات القادمة مستخدمةً الوحدات الفولتوضوئية. أيضا تم بناء ما يتجاوز 20 ميجاوات من أنظمة الوحدات الفولتوضوئية في مناطق مختلفة حول المملكة مثل أرامكو, الخفجي, جازان و جامعة الملك عبد الله للعلوم و التكنولوجيا في جدة. لكن التحدي الصعب ألان هو التغلب على الظروف الجوية كالحراره العالية و الرطوبة إضافةً إلى العواصف الرملية و التي من شأنها التأثير سلباً على أداء أنظمة الوحدات الفولتوضوئية من خلال تراكم طبقات الغبار على أسطح الوحدات. حيث قدرت بعض الدراسات أنه قد يصل مقدار التناقص في الطاقة المنتجة من الوحده الفولتوضوئية إلى ما يقارب 50% بعد ستة أشهر من التعريض للجو الخارجي؛ لهذا أتت هذه الرسالة لتضع عدد من الدراسات الأساسية لفهم و تقييم مشكلة تراكم الغبار من خلال البحث في الطبيعة الفيزيائية و الكيميائية لحبات الغبار المتراكم، فهم الطبيعة الفيزيائية لقوى التلاصق بين حبات الغبار و أسطح الوحدات الضوئية، و الذي من شأنه يقود لوضع الخصائص المرجوة لبناء أسطح ذات طبيعة طاردة للغبار و المياه في انٍ واحدٍ فضلاً عن قدرتها على تحمل الظروف الجوية الصعبة للجو الصحراوي. في هذا العمل تم تعريض عدد من الوحدات الفولتوضوئية للجو الخارجي من أجل تقييم مقدار التناقص في أدائها نتيجة تراكم الغبار. النتائج أظهرت خسارة بقدر 15% من الطاقة المنتجة من الوحدة بعد 5 أسابيع من التعريض للجو الخارجي. أيضا في هذه الرسالة تبين أن أقطار ذرات الغبار تتراوح بين 0.5 و 170 ميكرون و أنها ذات أشكال غير منتظمة

لكنها تميل إلى الشكل الدائري إضافة إلى كون الأوكسجين و الكالسيوم و السيليكون شكلوا النسب الأكبر في التركيب الكيميائي للغبار. أيضا في هذه الرسالة تم بناء أسطح هيدروفوبكية مختلفة من شرائح السليكون قادره على طرد الغبار و تقليل تراكمها مع الأخذ بعين الاعتبار المحافظة على نفاذية ضوئية عالية للسطح. يتميز السطح بقدرته على طرد المياه بطريقة تحاكي قدرة أوراق اللوتس على ذلك. و للتأكد من قدرة السطح على تقليل تراكم الغبار، تمت دراسة قوى التلاصق بين حبات الغبار و السطوح المطوره . النتائج أظهرت أن القوى التلاصق بين حبات الغبار و السطح المطور تقلصت إلى أكثر من 80% من قيمتها الأصلية على الأسطح العادية معتمدة في ذلك على تضاريس السطح. أيضا تم في هذا الرسالة دراسة طبيعة تلاصق حبات الغبار على الأسطح الزيتية . حيث حافظت هذه السطوح على قوى تلاصق أقل منها على السطوح المستوية الجافه. و لكنها تميزت بقدره هائلة على تقليل الاحتكاك بين حبات الغبار و السطح. أيضا تضمنت هذه الرسالة على دراسة أثر الرطوبة و تكاثف بخار الماء على قوى التلاصق بين حبات الغبار و السطح. النتائج أظهرت قفزة في مقدار قوى التلاصق في حالة الأسطح الجافة المستوية منها و المفبركة. أما في حالة الأسطح الزيتية، فلم يظهر أي أثر للرطوبة على قوى التلاصق.

CHAPTER 1

INTRODUCTION

The Kingdom of Saudi Arabia (KSA) is experiencing fast growth in electric power consumption due to increase the population and ambitious development projects. The average annual growth is around 10%. The KSA is considered to be the largest energy consumer in Gulf region with around 50 GW and on world scale; it occupies the second rank after Canada in the rate of energy consumption per capita. Meanwhile, it is important to realize that electricity generation in the KSA is oil and gas based as well as its income completely depends on exporting gas and oil. Currently around one-quarter of KSA total oil production (2.8 million barrels per day (mb/d)) is consumed domestically. For KSA to meet the planned electrical energy demand in the coming 20 years, it might end up using all its oil and gas production domestically.

Such projection has leaded the KSA to look seriously into alternative source of energy as well as implementing energy conservation resources. The electricity and co-organization regulatory authority (ECRA) announced that the KSA formulated a plan to reduce peak demand by 14% and energy consumption by 8% by 2021. Renewable energy sources are one of the advents that considered in such plan. The recently established King Abdullah City for Atomic and Renewable Energy (K.A.CARE) announced an ambitious huge plan for the utilization of solar energy in electrical power production sector. It is that the kingdom of Saudi Arabia will install 1481 megawatts worth of PV system during the coming 4 years. Besides KA-CARE

plans, a number of large Solar Photovoltaic installations have been installed or under construction such examples include the 500kW Farasan Island , KAUST 2 MW PV systems that provides electric power for the laboratories and the largest solar PV car park built by Saudi Aramco. Saudi Aramco is aiming to cover 7–10% of its electricity demand from renewable sources (solar PV, solar thermal and wind) by 2020.

On the level of Golf countries a number of ambitious plans for deployment of renewable energy infrastructure have been announced. For example, Qatar has announced plans to install 1.8 GW of PV power plants capacities by 2014 and Dubai aims to satisfy 5% of its power supply from solar energy by 2030.

The KSA lies in the solar belt, i.e. region abundant with high solar radiation (More than 6 kWh/m^2/day) and clear sky for more than 80% of the time throughout the year **[1]**. This is very favorable for the utilization of solar energy technologies, but at the same time indicates scarcity of rain, high ambient temperature and high humidity in the region close to sea. In addition; the Gulf countries including the KSA suffer from dust storms. In fact this type of harsh climatic conditions post a real unique challenge that need to be overcome to achieve high performance of solar energy systems. The combination effect of high temperature and humidity as well as dust fouling increases the complexity of the problem. The literature reported that the reduction on PV modules output reach as high as 50% due to dust accumulation **[2]**. On the economic side it is indicated that the dust deposition density of the order of 1 g/m^2 reduced PV-panel's energy production by up to 6.5% thus resulting in an annual income loss of almost 40€/kWp **[3]**.

To recover the performance of PV modules, an appropriate dust mitigation approaches should be developed. So far the reported dust mitigation methods in the literature can be divided into four categories: First, spontaneous which depends on the natural resources of cleaning like

raining, wind, and gravity effect. Second, mechanical and electromechanical which underlines on physical way of cleaning like mechanical wiping or blowing system that are controlled by microprocessor and Programmable Logic Controller (PLC). Third, generate repulsive electrostatic force to repel the fouling dust particle which is defined electrostatics shields. The last one is creating super-hydrophobic surface that is described with high self-cleaning efficiency; so that small amount of water is needed to remove the dust particles.

Micro/nano textured hydrophobic surfaces showed the potential to be self-cleaning surfaces with extremely non-wetting and transmissivity properties. Such type of surface can enhance the cleaning efficiency and reduce the water cleaning frequency through reduction the adhesion forces between the particle and surface, and making high contact angle between water droplet and surface .The latter prevents water droplet sticking and promotes its mobility along the surface, and as a result light air blowing or tiny amount of water can be enough to clean the surface. Hydrophobic surfaces can be categorized into two types based on trapped fluid between surface textures: Dry hydrophobic which traps air inside its textures, and wet hydrophobic where the textures are filled with lubricant.

Lubricant impregnated surfaces have a lot of advantages over dry hydrophobic ones, for example ability to sustain high impact pressure, humidity and vapor condensations, self-healing, and enhances surface transmissivity. In addition to that wet hydrophobic surface exhibit extremely low contact angle hysteresis thus better much self-cleaning and slippery properties.

However, in this thesis, I will first study the effect of dust fouling on PV modules performance and corresponding effect on its glass cover transmittance. I will then present intensive study for the accumulated dust particle, with a specific focus on its size distribution and

chemical composition. Furthermore, the nature of dust particle adhesion on flat silicon substrate will be explained and discussed using atomic force microscopy. I will then present study on effect of surface texturing and lubricant impregnation on silica particles adhesion forces .Finally, I will discuss the results to extract conclusion about the amount of PV performance reduction due to dust fouling, and about adhesion on dry and wet hydrophobic surfaces.

CHAPTER 2

LITERATURE REVIEW

There is an increasing enthusiasm in expanding the usage of renewable green sources of energy. This trend was driven by increased prices of fossil fuel, debatable effects on global warming, air quality deterioration, oil spills, and acid rain. One clean energy generation method is Photovoltaic. PV systems have gained an edge over other methods due to their reliability, low maintenance cost, absence of noise generation and safety. But despite new developments of higher performance materials, the biggest disadvantage of Photovoltaic systems remains their limited efficiency level which ranges between 12-20%.

PV systems performance degradation is mainly due to climate and environmental conditions. Although significant advances have been made in PV systems in the last few decades, designers still face challenges related primarily to climate conditions effects on PV system performance. In practice, one finds that PV module performance is much lower when operating outdoors than in laboratory conditions**[4]**. As summary, key climatic conditions that strongly affect PV module performance include solar irradiance, wind speed and direction, temperature, relative humidity, and dust **[5, 6].**

Studies have been conducted on the effects of different climatic conditions on PV systems performance. The study by **Mekhilef et al. [7]** reviewed the effects of dust accumulation, humidity level and air velocity. They concluded that each condition influences the other, and therefore they should be considered together. **Mani** and **Pillai [8]** revised the dust effect on PV

module performance during two time periods, namely 1940-1990 and 1990-2010. They developed and used an appropriate cleaning/maintenance cycle for their PV systems and considered the prevalent climatic and environmental conditions. The following sections present factors influencing PV module performance, particularly the effects of dust on glass surface transmittance and hence on PV module performance.

2.1. Effect of Climatic Conditions on PV Module Performance

There is disparity in the climate conditions from location to location around the world; so the corresponding effect on PV module performance also differs. The longitude and latitude of the region determine the nature of the environment. The parameters of such nature include the solar radiation, wind velocity, rain rate, temperature, humidity and probability of dust presence. The following sub-section summarizes the effect(s) each of these conditions on PV module performance.

2.1.1. Effect of Wind Velocity

Wind speed and direction can have both positive and negative effects on PV modules. The wind wipes away dust particles from the PV module surface, and hence it reduces the dust deposition. On the other hand, the wind enhances the dissipated convection heat transfer from the module, thereby reduces its temperature and maintains the solar module's conversion efficiency.

However, the wind could also have a negative effect by transferring and spreading the dust and sand particles in the atmosphere which may lead to increase dust deposition layers. In order to simulate the effect of wind speed and direction on the amount of dust deposition/accumulation as well as on PV modules performance, **Goossens et al. [9]** built a wind tunnel experiment. They indicated that the wind direction effects the dust deposition more than wind speed. Also

Goossens et al.[10] observed that the reduction in PV module performance due to dust accumulation is larger as wind speed increases.

2.1.2. Effect of Temperature

Temperature effects primarily depend on PV module encapsulating material as well as the atmospheric parameters. First, as the temperature increases, the band gap of the cells usually decreases resulting in absorption of longer wavelength photons. In addition, as temperature increases, the minority carrier lifetime generally increases. Both of these factors will slightly increase the light generated current I_{sc}, but in the same time lead to reduce the cell's open circuit voltage (V_{oc}). A decrease in V_{oc} is large rapid than the increase in I_{sc}, resulting in an overall reduction in the cell's fill factor, and hence, efficiency **[11]**. The module encapsulating material, such as thermal dissipation and absorption properties, as well as the atmospheric parameters which include irradiance level, ambient temperature and wind speed, dictate the effects of temperature **[12]**. During high temperature time, an obvious drop in PV performance was observed **[2, 13, 14]. Katkar et al. [15]** used an environmental chamber to test the effect of temperature on performance of industrial solar cell. It was concluded that the efficiency of solar cell increased from 9.702 % at 31^0C to 12.04% at 36^0C after that the efficiency started to decrease as shown in Fig.2.2b.

2.1.3. Effect of Humidity

Humidity adversely affects the performance of PV module by scattering solar incident beam and due to water vapor ingress into solar cell enclosure. Suspended water droplet in atmosphere which has a size larger than solar beam wavelength can scatter the solar light which in turn drive to reduction the amount of solar flux that reach to the solar module thus the power output as **Gwandu et al.[16]** reported and as represented in Fig.2.1a&b**.** An increase in solar panel

efficiency is observed at low relative humidity and the reason for this is the increase in solar flux **[12-14]**.

High level of surrounding humidity affects the performance of PV module**.** Presence the PV module in humid environment like humidity chamber caused an adverse effect on its performance due to water vapor, moisture and oxygen ingress to solar cell enclosure which leads to promote the corrosion/power degradation rates as shown in Fig.2.2a **[17-20]**.

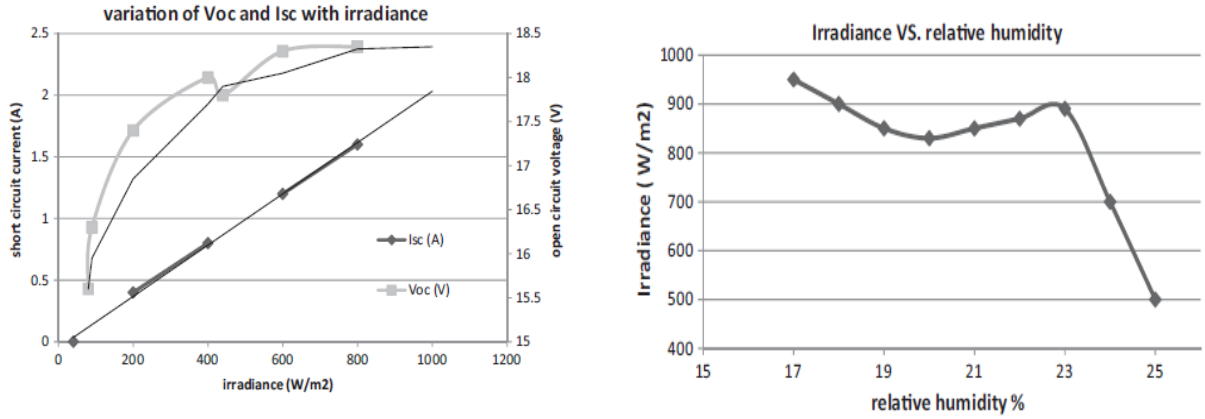

a. Variation of V_{oc} and I_{sc} with irradiance level **b. Variation of irradiance level with relative humidity**

Figure 2.1 Humidity effects on irradiance level as well open circuit voltage and short circuit current[21]

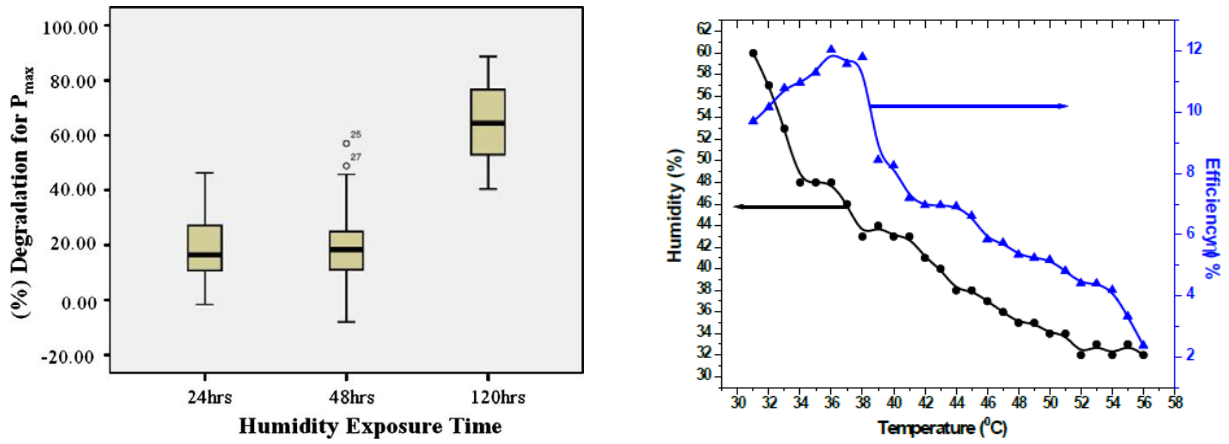

a. Humidity effect on PV module power output[22] **b. Efficiency Vs Temperature, Humidity[18]**

Figure 2.2 Humidity and temperature effects

2.1.4. Effect of Dust

There are two scenarios for the dust effect. First one is dimming the solar radiation due to the suspended dust particle in atmosphere. Dust particles have size larger than solar beam wavelength which may cause a scattering for solar light. The effect becomes worse when dust particles combine with air pollutants **[23].** Consequently, more than 60% reduction of PV module energy output is observed; due to the presence of dust and air pollutants in atmosphere **[24]**. The second scenario is forming thick layer of dust particle on PV module surface cover. Dust layers can change the surface optical properties through promote light reflection and absorption subsequently reduce the surface transmissivity and as result PV module performance.

There is a disparity in dust accumulation effect from region to another. It can be attributed that to site conditions such as wind velocity, humidity and rainfall, PV module technology, source of dust particle and its nature and the type of PV module surface cover.

The average degradation of PV module performance due to dust fouling is not uniform; since it is highly dependent on the site and weather conditions. Wide ranges of loss rates of PV module performance have been reported. High rate of reduction in regions suffer from lack of rainfall during the year are reported. A 50% reduction is reported in PV power output after six months of outdoor exposure in Dhahran-KSA **[2, 25]**. 2.78% reduction per day in short circuit current is reported in Arar-KSA **[26]**. 10% power output lost within 5 weeks is reported in UEA **[27]** which has almost similar KSA environment. 10% reduction in PV module efficiency after 100 days of testing is observed in Qatar **[14]**. 5 to 6% decrease in the solar panel efficiency in one week is reported in Palestine **[28]**. 60-70% power reduction in duration of six months is reported in Egypt **[29]**. A corresponding glass transmissivity reduction of around 20% is reported after one month of exposure **[29, 30]**.

The extent of dust effect either on PV module performance or PV cover transmissivity primarily relies on dust deposition rate. In general, increasing dust deposition leads to decrease PV module performance **[31-33]**, and its cover spectral and overall transmissivity **[29-31]**. To be precise the relation is not exactly linear and the reason beyond that is the nature of dust particle distribution on PV cover surface **[32, 34]**. Number of studies have quantified the amount of PV performance reduction at different dust deposition rates for example, the reduction in the conversion efficiency was 10%, 16% and 20% for 12.5g/m^2, 25g/$m^2$and 37.5g/m^2 dust deposition respectively **[35]**. Also, it is observed that PV module efficiency reduction ranges between 0 to 26% when increase dust deposition from 0 to 22 g/m^2 **[18].**

It is not totally true to say that the dust deposition increases by exposure time. It is mainly depends on climatic conditions during test period **[36]**. However, it is reported that increasing the time of exposure leads to increase the dust accumulation thus more PV performance degradation **[2, 3, 26, 29, 30].** For this reason, it is recommended to employ an appropriate cleaning cycle to recover PV module performance which also is governed to the climatic conditions **[2, 8, 28]**. In other region, dust deposition is decreasing by the time due to the continuity of raining **[37]**.

Dust accumulation differs from a surface to another. **Garg [38]** studied the effect of dust accumulation on glass and plastic plate's transmittance for two months in India. The results indicated that the plastic plate showed more transmittance reduction. Similar conclusion was reached by **Nahar et al. [39]** who observed that the PVC plate has more transmittance reduction followed by acrylic then glass.

The size of dust effect on PV performance depends on its technology. It is observed that for dust concentration 8.5 mg/cm^2, amorphous silicon showed 33% reduction in the spectral

photocurrent, compared with the crystalline silicon and copper indium gallium diselenide (CIGS) technologies which showed almost the same reduction (28.5%) **[31]**. In South Africa **Meyer et al. [11]** indicated that the performance of the Copper Indium Diselenide (CIS) module degraded by more than 20%. They also reported that the amorphous silicon (a-Si) module degraded by about 60%, and the a-SiGe module degraded by approximately 13% after an initial outdoor exposure of 130 kWh/m^2 (130 sun hours). Also, it is observed a 6% reduction in the electrical power for monocrystalline and polycrystalline modules and a 12% for the amorphous silicon module after three weeks of outdoor testing in Sonora, Mexico.

The nature of dust particles such as chemical composition and size distribution plays a big role in the amount of reduction of PV performance and its glass cover transmissivity. For example the red soil caused more energy reduction in PV compared with limestone when the same amount of each of them has been deposited on PV module surface. This difference due to the variation in the color, composition, and range of red soil particle size **[33]**. Also, $28g/m^2$ deposition rate of carbon showed more reduction in PV module power output than $73g/m^2$ of cement or $250g/m^2$ of limestone deposition rates. The reason for this being the origin of carbon particulates are the combustion process, hence carbon particles do effectively absorb the solar radiation which affect adversely PV performance **[40]**.

Fine particles showed more crucial effect on PV module performance. Comparative studies have been carried out by depositing the same density of different limestone particle sizes on PV module surface. The finer one caused more power reduction. This is attributed to the uniformity of fine particle distribution on the surface **[40]**. Furthermore, it is observed that during relatively high wind speed, more coarse particle be removed than fine ones **[34]**.

Another issue is the role of humidity in promotion the dust fouling. Vapor condensation on the surface formulates capillary bridges in gaps between the particle and surface and as a result large meniscus forces will be generated. Those forces can effectively enhance the adhesion between the particle and surface thereby encourages the dust build up **[19, 21, 41, 42]**. Practically, it is noticed an increase in the amount dust accumulation as the absolute humidity is increased **[17, 27]**.

2.2. Dust Mitigation Approaches

One of the effective ways to reduce dust accumulation effect on the performance of PV modules is creating micro/nano textured surfaces with low adhesion and non-wetting properties .Such surfaces are called hydrophobic surfaces. It can enhance the cleaning efficiency and reduce the frequency of cleaning, hence less water usage. The chemistry and morphology of such surfaces can reduce adhesion forces between the particles and the surface, make high contact angle between water droplets and the surface, prevents water droplets sticking and promote its mobility along the surface. Hence, light air blowing or small amount of water can be enough to clean the surface. The wetting behavior of the surface is described by contact angle and contact angle hysteresis which mainly depend on surface morphologies and chemistry.

2.2.1. Wetting on Surface

Wetting is one of the surface properties. It describes the behavior of deposited liquid droplets on a surface **[43]**. Wetting is characterized by contact angle between liquid droplets and a surface. Young **[44]** introduced equation (2.1) which relates liquid drops contact angle on homogenous and smooth surface with the specific interfacial energies of solid-gas, solid-liquid ,and liquid-gas as shown in Fig.2.3:

$$cos\theta_{flat} = \frac{\gamma_{sv}-\gamma_{sl}}{\gamma_{lv}} \quad (2.1)$$

Based on equation (2.1), it can be concluded that solid-air interfacial energy is the key factor that determines surface wetting properties. In other words, decreasing the surface energy (i.e. solid-air energy) leads to enhance the surface hydrophobicity.

Another fundamental process to enhance the hydrophobicity is surface texturing. According to Wenzel relation **[45]**, increasing the roughness of hydrophobic surface tends to improve its non-wetting properties and vice versa. The following Wenzel equation relates contact angle with surface roughness **[45]**:

$$cos\theta_{Rough} = rcos\theta_{Flat} \quad (2.2)$$

where θ_{Rough} is contact angle of a rough surface, θ_{Flat} is contact angle of a flat surface, and r is roughness factor of the rough surface. The roughness factor is defined as the ratio of the total surface area of the rough surface to the projected area of the rough surface **[46]**.

Cassie Baxter assumes that liquid droplet do not completely wet the surface texture due to the presence of trapped air between posts of the surface texture. Consequently , the surface has two interfaces , solid-liquid and air-liquid as shown in Fig.2.4 and described in the following relation**[47]**:

$$cos\theta_{Rough} = \emptyset_s cos\theta_{Flat} + \emptyset_v cos\theta_{LV} = \emptyset_s cos\theta_{Flat} - (1 - \emptyset_s) \quad (2.3)$$

where $\emptyset_s$ and $\emptyset_v$ are the fractions of solid and air contacting the liquid. The contact angle between air and water equals 180°. Based on equation (2.3), solid fraction is the key parameter that can control the wetting properties of the surface.

Substitution equations (2.2) into (2.3) leads to introducing a definition of critical contact angle given by **[48]**:

$$cos\theta_c = \frac{1-\emptyset_s}{r-\emptyset_s} \qquad (2.4)$$

Equation (2.4) indicates that liquid contact angle on a flat surface is more than the critical angle; the liquid will tend to partially wet the surface (i.e. Cassie Baxter). Otherwise the surface will be completely wetted as shown in Fig.2.4 (i.e. Wenzel state).

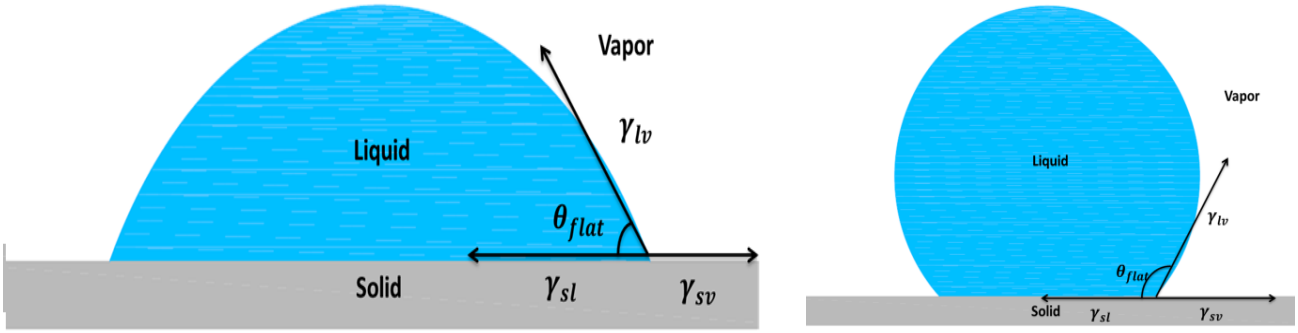

Figure 2.3 Water contact angle on hydrophobic and hydrophilic surfaces

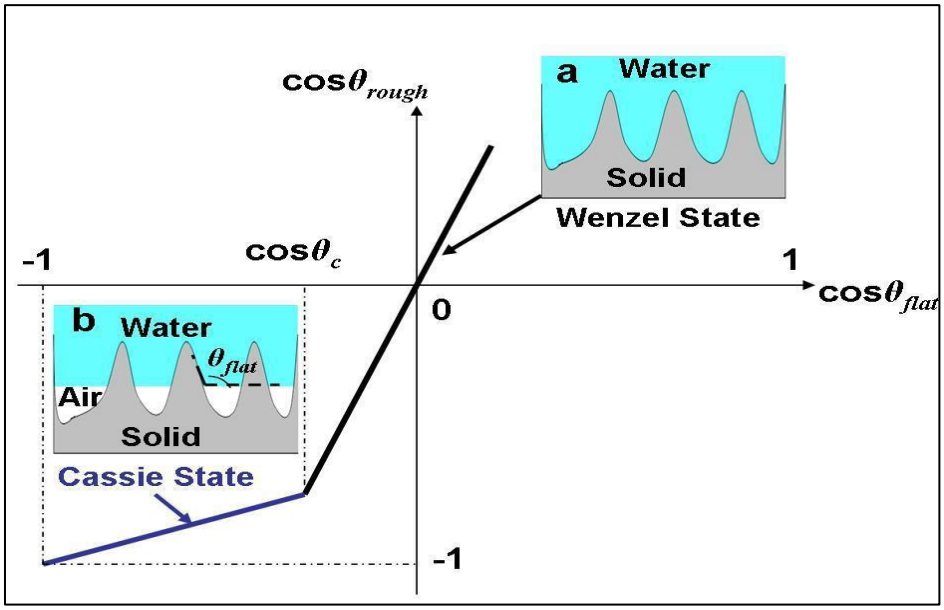

Figure 2.4 Wenzel and Cassie Baxter wetting states[49]

2.2.2. Contact Angle Hysteresis

Contact angle hysteresis (CAH) determines the sliding and rolling properties of liquid droplets along the surface. It is a type of dynamic contact angles. When inflating a droplet, there is a threshold value of contact angle beyond which the line of contact start move (i.e. increase in area of contact) which is implied with advancing angle. Likewise, when deflating a droplet, there is as a threshold value of contact angle beyond which the line of contact start move (i.e. decrease in area of contact) which is implied with receding angle **[43].** CAH equals the difference between advancing and receding contact angles. CAH depends on the type of deposited liquid **[50]** ,surface texture posts spaces and morphologies **[51-54]** and the type of impregnated liquid in case of lubricant impregnated surfaces **[55, 56]**.

Hydrophobic surfaces can be categorized into two categories based on the type of fluid being trapped between the posts of surface texture: Dry hydrophobic which traps air inside its textures, and wet hydrophobic where the spaces between the texture posts are filled with lubricant.

2.2.3. Dry Hydrophobic Surface

Mimicking the morphologies of natural superhydrophobic surface like the lotus leaf structure is the first step to come up with hydrophobicity properties. Template-based techniques, plasma treatment, self-assembly and self-organization, chemical deposition, layer-by-layer (LBL) deposition, colloidal assembly, phase separation and electrospinning are some of the main methods to develop hydrophobic surfaces **[21, 22, 57]**. A number of studies on developing self-cleaning solar module glass cover surface with high optical properties are reported in the literature. **Park et al. [58]** developed superhydrophobic surface with contact angle higher than 150° and a hysteresis of lower than 20° by fabricating an ordered microshell array on transparent and flexible polydimethylsiloxane (PDMS) elastomer surface without a need to a low surface

energy chemical coating. **Verma et al. [59]** created superhydrophilic nano-structured glass with contact angle less than 5° by deposition of thin film of nickel on glass substrates, followed by annealing to create nickel nanoparticles. Their result showed an improvement in the solar cell performance, since net optical transmission increased and the surface is proven to be self-cleaning. **Hee et al. [37]** using a simple method deposited different thicknesses of TiO_2 film on glass surface. They observed that dust accumulation was decreased due to the deposition effect and this effect became more significant when increasing the film thickness.

However, such dry hydrophobic surfaces do have their limitations for example. It cannot sustain high impact pressure. During the vapor condensation, surface loses its non-wetting properties. In addition micro-textures can enhance the light reflection. Lubricant impregnated surfaces do overcome limitations. In addition to that wet hydrophobic surface exhibit extremely low contact angle hysteresis thus provides better self-cleaning and slippery properties.

2.2.4. Wet Hydrophobic Surfaces

Texturing the hydrophobic surfaces enhances the non-wetting properties by increasing the surface geometry while the trapped air between the surface texture posts leads to a superhydrophobic behavior, because the droplets sit partially on air **[48]**. However, the challenge is to keep air pockets stable between the texture posts. But in case of humid conditions like KSA environment, the air pockets can collapse due to dew condensation or evaporation. This occurs at a nanoscale throughout the texture and in turn leads to a highly wetted textured surface **[48]**. Such effect draw the attention to develop non-wetting surfaces with self-healing properties are maintained by creating pockets of liquid instead of air by impregnating the texture with lubricant. The lubricant is stabilized by capillary wicking arises from the Mirco or Nano texture **[60]**. **Lui et al. [61]** fabricated LIS by filling organogel-based film on substrate with oil. The

surface showed low contact angle hysteresis and self-cleaning efficiency. **Wong et al. [50]** prepared LIS through impregnating ordered epoxy-resin-based nanostructured surfaces and a random network of Teflon nano fibrous membranes with lubricant perfluorinated fluids. It has been showed that LIS has the ability to repel different types of low and high surface tension liquids such as water, Glycerol, and Ethylene glycol. Furthermore, matching the refractive indexes of lubricant fluid and substrate leads to render the micro-texture high transparent **[50, 56]**. Also, LIS demonstrated self-healing properties .In case of any surface physical damage, the oil can flow and fill cracks and retain its surface properties **[50]**. On the other hand, LIS can sustain high drop impact pressure **[50],** reduce ice accretion **[50, 62, 63]** and enhances condensation and heat transfer dissipation **[64, 65]**.

The lowest total interface energy state of water droplet represents the thermodynamics stable configuration. It depends on surface texture and impregnated liquid properties such as viscosity , spreading coefficient and density **[55].** Viscosity of oil plays a role in droplet sliding angle and velocity. High viscous oil leads to reduce the droplet rolling speed and increases the sliding angle **[55, 56, 61].** On the other side , using high viscous oil can enhance the shearing sustainability of the surface **[50].**

2.3. Sphere-Plane Surface Dry Adhesion Forces

Adhesion between a particle and a surface depends mainly on particle size as well the surface energy based on Johnson-Kendal-Roberts (JKR) **[66]** and Derjaguin-Müller-Toporov (DMT) **[67]** models. JKR and DMT models describe the adhesion forces between smooth particle and smooth substrate. The adhesion force is a linear function of particle size and effective solid surface energy for both particle and substrate.

However, early measurement showed discrepancy between the measured and predicted adhesion force magnitudes. The reasons being the effect of surface irregularities and roughness of the particles as well substrate. Surface roughness reduces the real area of contact between solid surfaces **[68-70]**, due to the presence of higher asperities which keep the surfaces apart and break the adhesions occurring at the lower asperities **[71].** In general, there is a proportionality relation between surface roughness and adhesion force **[72-74]**. But, to have a drastic reduction in adhesion force two preconditions should be fulfilled: the surface must be appropriately rough and the peak-to-peak distance between the roughness posts must be in the right proportion ; to minimize the density between the two adhering partners **[75]**. A number of methods have been experimented to measure adhesion forces. These include: atomic force microscopy **[70, 72, 74, 76, 77]**, vibration method **[78]**, direct separation method **[79]**, electric field detachment method **[80, 81]**, impact method **[82]** and Centrifugal method **[83, 84].** Theoretically, a number of models have been developed to simulate the effect of surface heterogeneity of plane substrate and colloid particle. Surface roughness is represented as spherical cores on the outer shell of the particles **[85],** small hemispherical asperity **[86-88]**, close-packed hemispherical asperity caps and troughs with peak to peak asperity distance **[72]**.

2.4. Sphere-Plane Surface Meniscus Adhesion Forces

Capillary force is caused by condensing water or presence of thin film of liquid between a probe and a planar surface.

At high humidity conditions, meniscus of condensed vapor is formed. Kelvin described the relation between vapor pressure and the curvature of condensed liquid surface by the following equation **[44]**:

$$RT.In\left[\frac{p}{p_o}\right] = \gamma_L V_m \left(\frac{1}{r_1} + \frac{1}{r_2}\right) \quad (2.5)$$

where R=8.314 J/mol.K is the molar gas constant, T is the temperature, P_0 is the saturation vapor pressure over a planar liquid surface, P is the saturation vapor pressure with a liquid of curvature ($1/r_1+1/r_2$), r_1 and r_2 are the two principal radii of curvature, γ_L is liquid surface tension and V_m is the molar volume of the liquid. The right side of equation represents the Laplace pressure, which is the difference between the pressures at meniscus interface.

The combination between Laplace pressure and the surface tension of the liquid causes an attractive force that leads to enhance the particle adhesion. An increase in capillary forces is observed with increasing relative humidity **[76, 89, 90]**. But, it is found that the nature of liquid meniscus and the effect of RH humidity differ due to particle shape **[91]**, size **[77, 92]**, surface chemistry **[77, 90-93]** and surface morphology or roughness either for particle or surface **[77, 90, 92, 94]**.

Different behaviors of humidity effect on capillary force between Atomic Force Microscopy (AFM) tips and planar surfaces have been reported. Adhesion force between AFM tip and plane surface showed an increase due to increase in humidity but after a certain humidity level, adhesion force started to decrease even with increase in humidity. The reason being that when the humidity exceeds the threshold value the meniscus radius becomes larger than tip radius. Hence, the Laplace pressure becomes positive and its effect converts to repulsive force **[91]**.

The effect of surface roughness on meniscus force depends on surface asperity height and humidity level. At low humidity level where there is no obvious vapor condensation (i.e. the radius of meniscus is less than asperity height), the roughness can play a role in preventing

meniscus formulation by creating weak capillary bridges between the top of roughness posts and sphere. At high humidity, the capillary neck radius becomes larger, thus the meniscus force forms between sphere and flat surface instead of forming between roughness peaks and sphere**[44, 89, 90, 92]**.

There is no considerable effect of humidity on the adhesion forces between hydrophobic surfaces. Hydrophobic surfaces reduce the probability of vapor condensation especially at low humidity. The non-wetting properties of the surface prevent capillary bridge creation which is on the contrary happened in case of hydrophilic surfaces. However, the effect of humidity becomes larger and effective if the interaction surfaces are hydrophobic-hydrophilic**[76, 91]**.

2.5. Adhesion Forces on Liquid Film

The force between solid particle and liquid surface is fundamentally different than between solid-solid interaction. The dominant force in case of solid-liquid interface is the capillary force. The formulated capillary bridge is resulted from the effects of capillary pressure and surface tension forces. The particle keep under force effect even after retracted from the solid surface beneath the liquid film. Adhesion depends mainly on the liquid film properties such viscosity **[95]**, density and surface tension **[95, 96]** in addition to film thickness and detachment speed **[95]**. Furthermore, because the viscous effect and dynamics of miscues formulation additional force are needed to detach a particle from a film, the maximum force during detachment is not necessarily at the position where the particle breaks away from the interface **[96]**.

A distortion is observed in AFM solid-liquid force curves. The reasons being the attractive interaction between the bead and liquid surface due to Van der Waal and electrostatic forces **[97,**

98]. And a results of the jump contact point, film thickness and meniscus stability will be altered **[42, 93, 99, 100]**.

Even though a number of published studies indicated the significant impact of climatic conditions particularly dust fouling on PV module performance, still number of questions do remain to be answered. For example, the nature of dust particles number such as size distribution, and chemical composition. Another fundamental issue is related to the nature of adhesion mechanism and adhesion forces quantification between dust particles and flat or textured surfaces.

The present study besides investigating the overall effect of dust on PV module power output, it investigates the characteristic of dust, module glass and forces between dust particles and glass cover that affect the dust deposition. Also, the study looks into possible cleaning techniques of reducing the dust effect.

2.6. Objectives

The overall objective of this M.S. thesis is ***to understand the nature of dust fouling effects on the cover glass surface of PV modules****. The specific objectives include:*

1. Quantify the magnitude of dust effect on PV modules performance.
2. Analyze the chemistry and physical properties of dust particles.
3. Understand the nature of dust particle adhesion mechanism.
4. Study the adhesion on wet and dry hydrophobic surfaces.

CHAPTER 3

EXPERIMENTAL INVESTIGATION

The exerimental investigation is divided into two main parts. First part includes test of PV module performance at outdoor condition and characterization of dust and PV module glass cover. Second part includes farbrication of different length scales of dry and wet hydrophobic surfaces and testing the adhesion and friction properties of the fabricated surfaces. The following sections discribe in details the procedures of each experiment.

3.1. Site Environment Description

The test facility in this study is located in Dhahran, Saudi Arabia (Lat. 26^{o}17'N, Long. 50^{o}09'E, Alt. 24 m). Both the average diurnal and annual temperature ranges are quite large (both about 15^{o}C). High humidity is more pronounced during the peak cooling season (June to September). Rainfall is scarce and the total average annual rainfall is about 80 mm, mostly occurring during the winter. The sky is clear, except for a few scattered days in winter, but the atmosphere is quite turbid. Consequently, solar radiation is intense and at noon may exceed 1000 W/m^{2}.

3.2. Tested PV Modules and their Glass Covers Description

14 of PV modules were tested at the outdoor conditions in Dhahran-KSA as shown in Fig.3.1. The modules were installed at an inclination 26°. All modules are identical and have same electrical specifications. The modules are mono-crytalline cell based and each one has six

cells. The module Maximum power voltage (Vmp) is 3.6 V, Maximum power current (Imp) equal 7.5 A, and maximum power equal 27 watt. The specification of tested modules are given in Table 3.1.

The difference between the modules is the type of its glass cover. Plane surface and plane coated with anti-reflective material were used as PV glass cover. The glasses were provided from different manufacturers. Glass thickness ranges from 2.9mm to 3.2mm and their transmittance is more than 90% as shown in Table 3.2. The modules rack cointains two rows of PV modules as shown in Fig.3.1. The PV modules in the top row were left without cleaning during the test period, while the ones on the bottom row were being cleaned daily.

Figure 3.1 Outdoor PV modules test facility at KFUPM

Table 3.1 PV modules specification (cell-data)

Manufacturer	Fraunhofer ISE
Cell type	Mono Crystalline
Number of cells	6
Cell efficiency	18.22 – 18.43
Dimensions	60x40x5cm^3
Fill Factor (FF)	78.7 – 78.9 %
Power Tolerance	+/- 1.5 % rel.
Maximum power rating (Pmax)	4.39 – 4.44 Wp
Open circuit voltage (Voc)	625 mV
Short circuit current (Isc)	8.920 A
Maximum power voltage (Vmp)	525 mV
Maximum power current (Imp)	8.380 A
Temperature coefficient of current(α)	+0.04 %/K
Temperature coefficient of voltage(β)	-0.33 %/K

Table 3.2 PV modules glass cover specification

Glass Manufacturer	Glass Name	Glass Type	Glass Surface	Glass Thickness	Light Trans.
Saint Gobain	Securit Diamant	extra-white float	plane	2.9 mm	90-91%
CentroSolar	Centrosol C+ HiT	extra-white float	plane, 1xAR	3 mm	94.82 %
CentroSolar	Centrosol C+	extra-white float	plane	3 mm	91.69 %

3.3. PV Modules Electrical Performance Testing

The different electrical PV modules parameters as well as ambient condition one are measured and recorded using a data acquisition unit as shown in Fig.3.2. The unit is located inside an air conditioned portable room in the vicinity of PV module test area. The core element of the unit is the electronic loads. Each module has been connected with separated load via special control cables. The unit is programmed to record I-V curve of each module every ten minutes. PT 100 temperature sensors are fixed on the middle back of each module and connected to the unit. In order to measure the incident irradiance on the plane of installed modules, standard calibrated Pyranometer and reference cell were fixed at the left hand corner of stand as shown in

Fig.3.1. The fluctuation in radiation is determined and recorded through comparing the reading of both Pyranometer and reference cell. Also, the system includes Vaisala Weather Transmitter WXT520 to record metrological data such as ambient temperature, humidity, rain rate, and wind speed and direction.

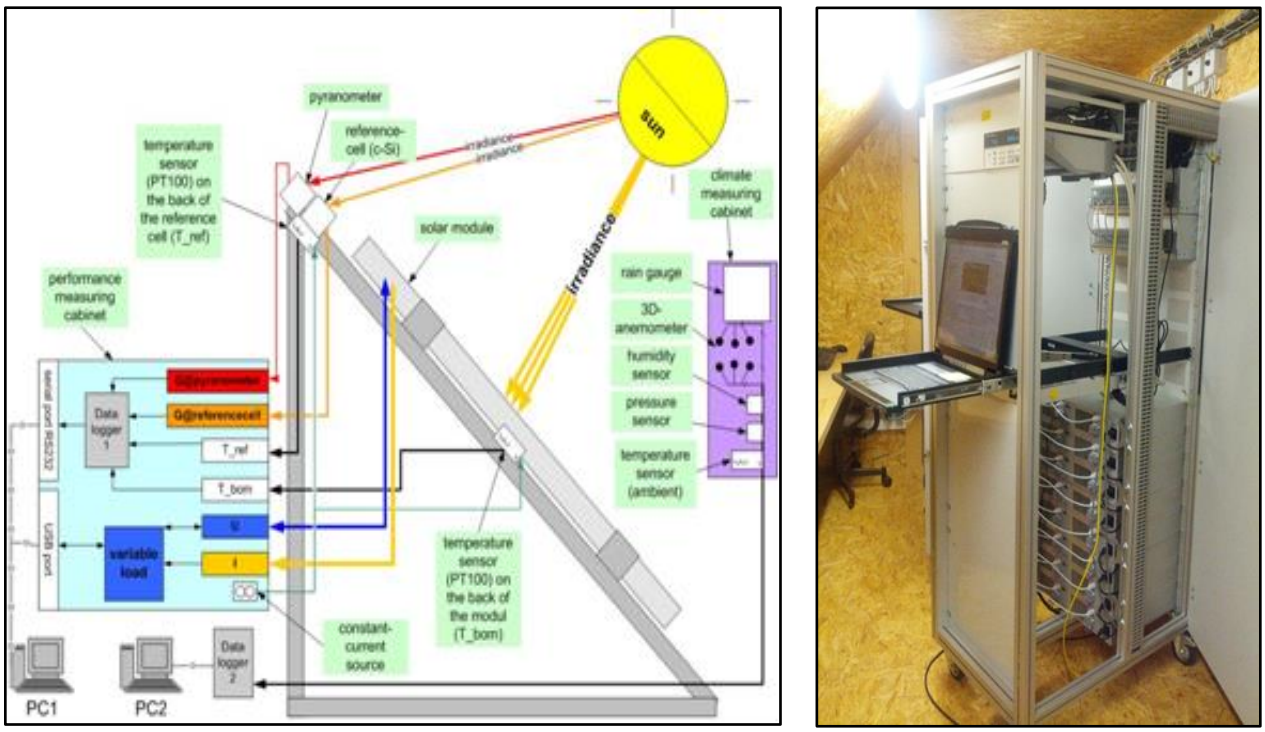

Figure 3.2 Schematic assembly of the measurement equipment and PV modules monitoring unit

Figure 3.3 shows the monitoring unit flow chart that illustrates the typical measurement sequence which includes:

- Measuring open circuit voltage (V_{oc}) of the modules (source off), then setting electronic load to 0.98 V_{oc}, source on.
- Measuring ambient variables (POA irradiance, irradiance of reference cell, and temperature)
- Parallel scan mode: the loads records the IV curves each and keeps them in their memory, simultaneously measure the back of module temperatures

- Again measuring the reference cell irradiance to record the irradiance fluctuation during the scan, get IV curve to the computer , extract point of interest and store the whole IV curve for later analysis
- Drive the module MPP, V_{oc}, or I_{sc} and keep them until the next cycle, gather value in between.

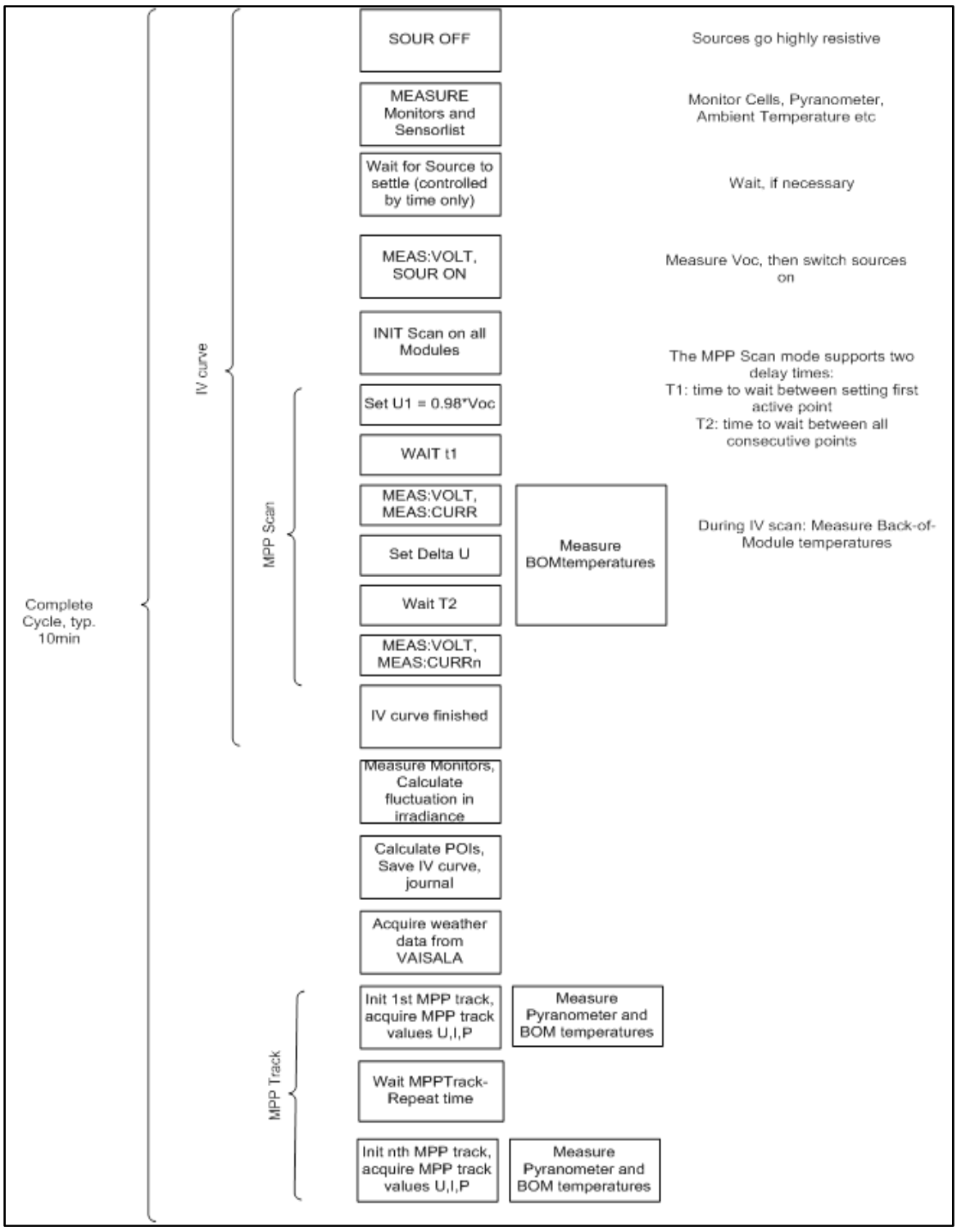

Figure 3.3 PV modules monitoring unit flow chart

3.4. Glass Surface Characterization

The surface topography and roughness of samples of PV module glass were determined using Atomic Force Microscopy (AFM). Also the wetting properties of PV module glass cover were characterized using contact angle measurement. The optical measurements for spectral transmittance of glass cover were conducted using a spectrometer; in order to determine the effect of dust deposition on glass transmissivity. The following sub-sections describe in details the procedures of each test.

3.4.1. Glass Surface Morphology

The nature of surface morphologies plays a big role in particle adhesion and surface transmissivity. Three different types of glass covers were characterized in this study. Agilent 5500 atomic force microscopy were used to extract surface topography images and roughness parameters as shown in Fig.3.4. Tapping mode was applied to make 10x10um scanning area; the speed of scanning was identical for all the 3 surfaces to avoid any effect on roughness analysis. Tapping mode silicon nitride tip with 4N/m spring constant and 12nm tip radius was utilized. The scanning were carried at the lab condition (T=25° C and RH=40%) for all the 3 surfaces. The roughness analysis and topography images have been processed using Pico View software.

3.4.2. Glass Wetting Properties

In order to determine the difference between the self-cleaning efficiencies of all tested glasses, contact angle were measured in the presence of air using KYOWA goniometer (see Figure 3.5). 5 μl water droplets were deposited; sessile droplet method was used to calculate the water contact angle at the lab condition (T=25° C and RH=40%).

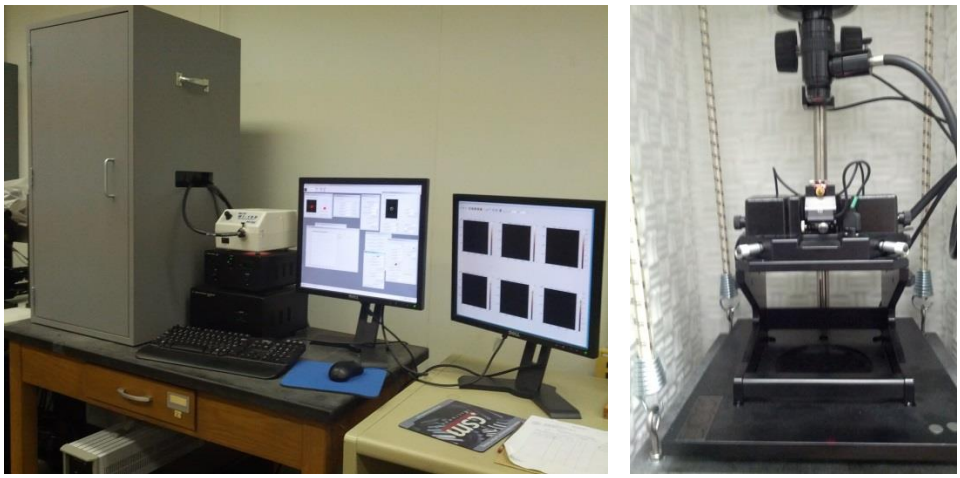

Figure 3.4 Agilent 5500 Atomic Force Microscopy

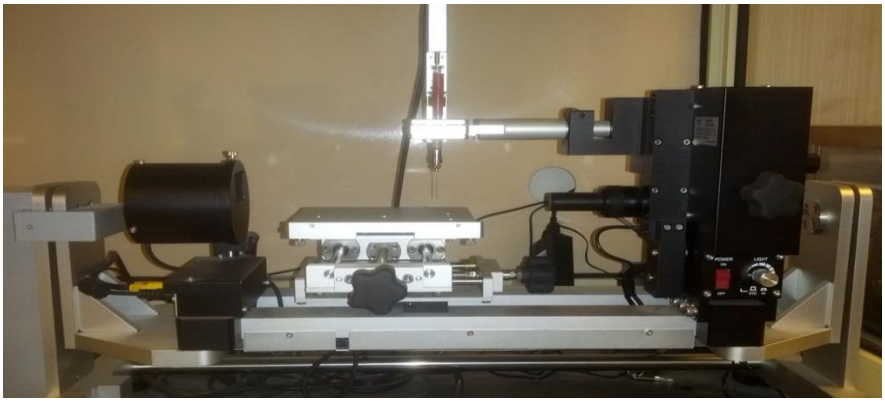

Figure 3.5 KYOWA contact angle measurement

3.4.3. Glass Optical Measurements

Optical measurements included spectral transmittance tests for all types of glass that used in the tested modules. Thermoelectric spectrophotometer was used to measure the glass surface transmissivity. Spectral transmittance was recoded between 300 and 850 nm wavelength.

The spectral transmittance tests were conducted for Centrosol C+, Centrosol C+ HiT, and Saint Gobain plane samples. Firstly, test stand that are capable of holding a number of glass samples at 26 tilt was made to expose the glass samples. A photo of the test stands is shown in Fig.3.6a. The stand was facing the south. The glass samples were not cleaned for 45 days during

the months of February and March 2013. During the exposure period, glass sample spectral transmittance was being measured periodically.

a. 26º stand **b. Spectrophotometer**

Figure 3.6 Aluminum stand that used for exposing the glass samples and Spectrophotometer

3.5. Dust Particles Characterization

Knowing the nature of dust particles is the first step toward designing a surface with low adhesion properties. Dust samples were taken from the accumulated dust on the surface of PV modules glass cover using fine brush. More than ten samples were picked up during the year. Each sample was subjected to systematic characterization tests that included chemical composition, size analysis and morphologies.

3.5.1. Chemical Composition

The dust sample particle chemical element analysis was carried using TESCAN Field Emission Scanning Electron Microscope (FESEM), Energy Dispersive Spectroscopy (EDS), BRUKER X-ray Fluorescence (XRF) and Rigaku Ultima IV X-ray diffraction (XRD). A photo of these instruments is shown in Fig.3.7. A brief description of the test conditions carried out by each of these instruments is as follows:

EDS: During EDS tests; small amount of dust powder were placed on circular base cover with carbon tape. The dust layer was coated with 5nm film of gold to enhance conductive properties. EDS analysis were conducted at several locations on scan area. The averages of all spectrum point of interest were determined. The beam voltage ranged from 15-20KV. The scan area ranged from 1-50um to be able to see small and large particle sizes. In order to get high quality images, beam current and voltage and working distance were optimized.

XRF: During XRF tests; the dust powders were placed between MYLAR films. The analysis was run under vacuum. The operating conditions were: 40 KeV beam energy, 200 uA tube current and 50 KV tube voltage.

XRD: During XRD tests; dust samples were grounded to fine powder and placed on holders. The energy of X-Ray was 40 kV; the speed of scan was 2.0deg/min. The scan range was between 4.0 and 80.0deg with step width 0.02 deg and incident slit 2/3 deg.

a. FESEM **b. XRF** **c. XRD**

Figure 3.7 Dust chemical analysis instruments

3.5.2. Size Distribution

Microtrac S3500 Particle Size Analyzer supported by Microtrac FLEX Software was used to characterize the particle size distribution of the dust particles. A photo of the analyzer is shown by Fig.3.8. Wet and Turbotrac dry approached were carried out. The system was capable

of measuring particles size in the range of 0.25µm up to 2800µm. Small amount of dust powder were placed inside the channel in case of dry and inside the liquid cell in case of wet approach. The distribution of the number, surface area and volume of the dust sample under test as a function of particle size (diameter of the particle)**,** mean volume diameter(**MV)**, mean number diameter **(MN)** , mean area diameter(**MA**), and number of statistical parameters such as standard deviation ,skewness,and peakedness were determined using the Microtrac FLEX software. The tests were repeated for a number of collected dust samples.

Figure 3.8 Wet and dry Microtrac size analyzer

3.5.3. Microscopic Images

TESCAN Field Emission Scanning Electron Microscope (FESEM) shown in Fig.3.8 was used to determine the morphology of dust particles as well as the nature of interaction between the particles. Small amount of dust powder were placed on the circular base covered with carbon tape. The dust layer was coated with 5nm film of gold to enhance conductive properties. The beam voltage was ranged from 15-20KV. The scan area ranged between 1-50um to be able to see the small particle size. In order to get high quality images, beam current and voltage and working distance were optimized.

3.6. Hydrophobic Surfaces Fabrication

Micro and nano-textures of silicon substrate were developed using standard photolithography and deep reactive ion etching. The samples were then treated with a low-energy silane (octadecyltrichlorosilane-OTS) by solution deposition. The samples were impregnated with lubricant by slowly dipping them into a reservoir of the lubricant. The following sub-sections explain in details the samples preparation procedures.

3.6.1. Micro-texture Surfaces Fabrication

Three main steps were required to prepare a micro-texture surface: Photolithography, Etching, and cleaning respectively. Figure 3.9 illustrates all fabrication steps. All the processes were carried out inside a clean room at the Center of Nanoscale System (CNS)-Harvard University.

1. Photolithography

Photolithography includes three processes started with spin coating followed by UV exposure, and chemical developing. Brief description of each process is given below:

A. Spin coating

Silicon wafer (n-type<100>) with 300 mm diameter and 775 µm thickness was used for micro-texture surface fabrication. In the beginning, the silicon wafer was heated at 200° C for 10 minutes to remove any moisture. Then the wafer was coated with HMDS primer (recommended for use with photoresist) using spin coater at 2000 RPM for 30 seconds (based on HMDS primer data sheet). After this the wafer was baked at 115° C for 2 minutes to remove any moisture and to strengthen the film adherence. Then wafer was coated with

S1813 photoresist using spin coater at 4000 RPM for 40s and again baked at 115° C for 2 minutes. The thickness of photoresist is around 1.3 microns.

B. Exposure

The next process was exposing the wafer to UV-light. A photo-mask with three different micro-textures was placed on the top of wafer using Mask Aligner. The exposure time was calculated by dividing 150 Joules on value of tool's UV light intensity (J/s). After exposure, the wafer was baked at 115° C for 10min.

C. Developing

To develop the exposed photo-resist areas, the wafer was placed in a beaker of CD-30 chemical developer. The beaker was agitated to promote the developing for 1-2 minutes. After that, the wafer was cleaned with water and dried using nitrogen gas.

2. Etching (Deep Reactive Ion Etching ,DRIE)

First, the system was conditioned with a blank wafer using an O_2 gas. To make the system ready a blank wafer was placed inside the system, and then Si etch recipe was run for 10 minutes. After that, blank wafer was replaced with real one, and again Si etch recipe was run for 10 minutes. The etch rate, type of gases and gases flow rate were optimized to get 10 micron height posts.

3. Cleaning

The final process included cleaning the etched wafer with a typical Piranha cleaning solution (3 parts H_2SO_4 to 1 part H_2O_2). The cleaning was carried out at 125° C temperature for 20 minutes. The post height was checked using an optical profiler.

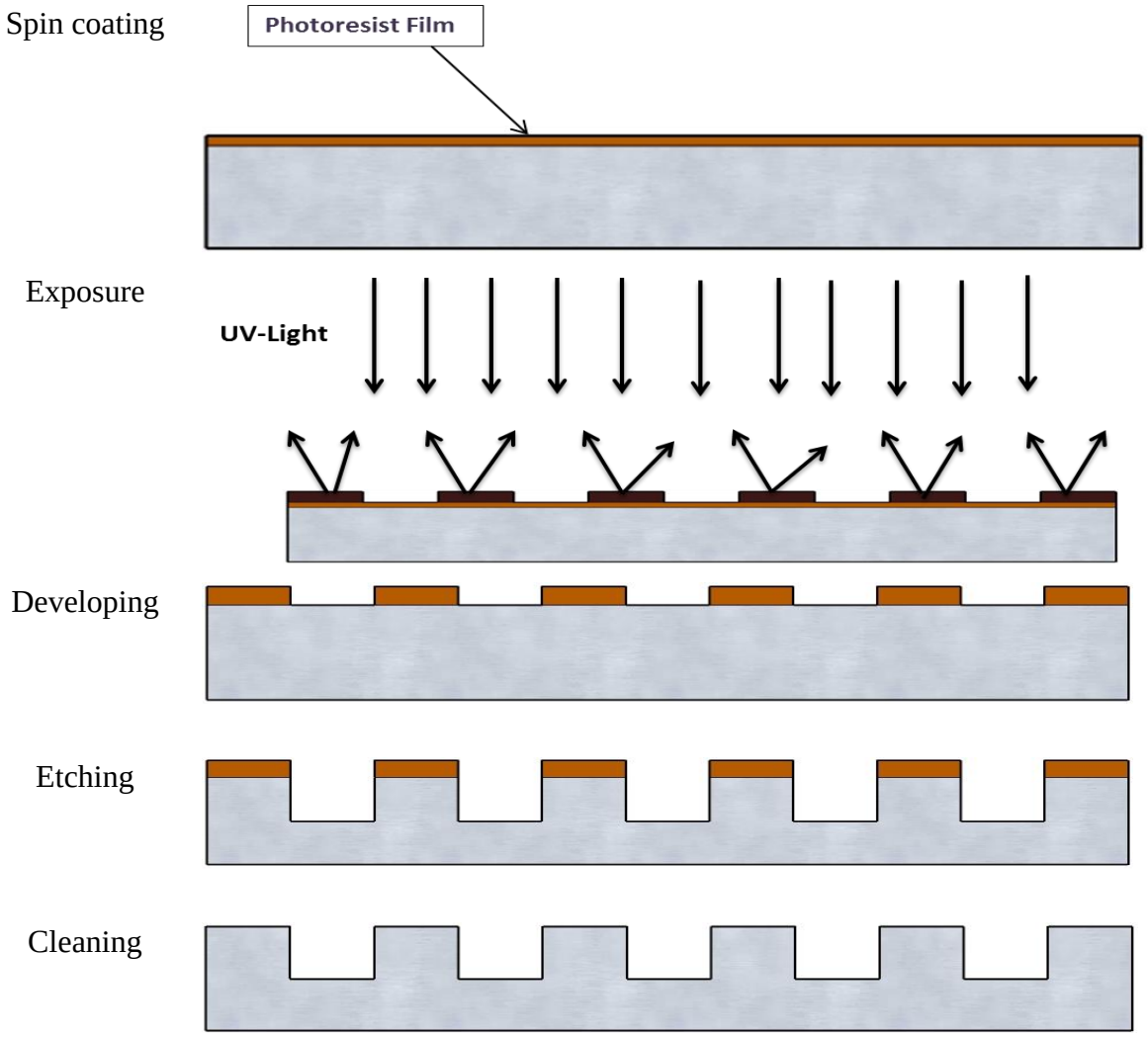

Figure 3.9 Micro-texture fabrication procedures

The developed micro-textures are arrays of square microposts with width a = 10 μm, height h = 10 μm, and varying edge-to-edge spacing b = 5, 10, 25 as shown in Fig.3.10.

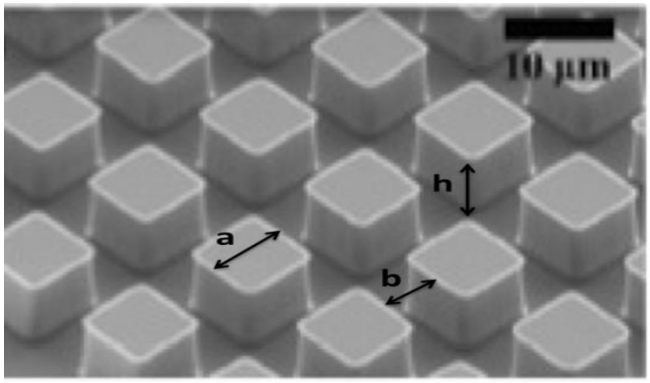

Figure 3.10 SEM image for 10x10um texture

3.6.2. Nano-grass Surfaces Fabrication

To develop a nano-grass texture, only Deep Reactive Ion Etching process was required. Silicon wafers (n-type<100>) with 50 mm diameter and 350 µm were used. At the beginning, the wafer was heated at 200° C for 10 minutes to remove any moisture. Then the Si wafer was placed inside the system. Etching was carried out using 100 cc/min of SF_6 and 75cc/min of O_2 for 10 minutes. Figures (3.11&3.12) show the topography image for fabricated nano-grass texture. The average and root mean square roughness measured by AFM were 62nm, and 49nm respectively.

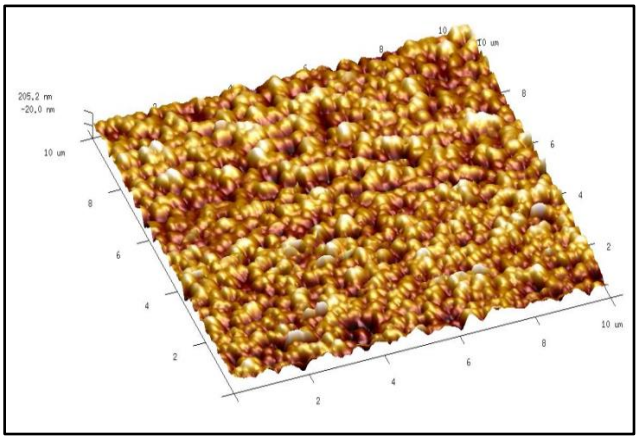

Figure 3.11 AFM nano-grass topography image

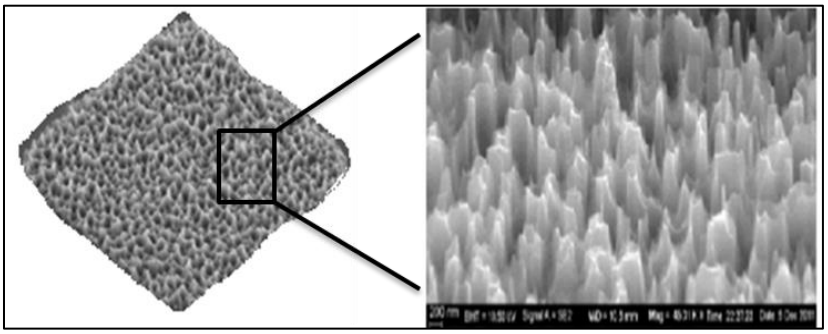

Figure 3.12 SEM image for nano-grass topography

3.6.3. Surface Silanization

Solution deposition method was used to achieve the surface silanization. 0.125 ml (octadecyltricholorosilane –OTS) silane, 62.5ml toluene, 0.162 ml of water and 50 ml of acetone were required to silanized the surface. The process included the following steps:

1. Dissolving 0.125 ml silane in 37.5ml toluene in staining dish and then started sonication until fully dissolved.
2. Stirring 0.162 ml of water into 25 ml of toluene in beaker to form emulsion.
3. Placing the sample inside the staining dish on the sonicator.
4. The beaker was lift from the sonicator and then directly the emulsion was added to the staining dish. After two minutes of sonication, the sample was removed from the staining dish and directly rinsed with acetone then sonicated in acetone for another 2 minutes.
5. Finally the sample was cleaned using isopropyl alcohol before the acetone had dried and completely dried using nitrogen gas.

3.6.4. Surface Oil Impregnation

The silanized samples were impregnated with lubricants by dipping them in a reservoir of the lubricating liquid with a dip-coater (KSV Nima multi vessel dip coater) and then carefully withdrawing them at a controlled rate. Samples were withdrawn at a rate V such that the capillary number, $Ca = \mu V/\gamma$, corresponding to an impregnating lubricant with viscosity μ and surface tension γ, was less than 10^{-5}. This ensured that no excess lubricant remained on the post tops. Figure 3.13 shows ESEM images for the 10um space texture impregnated with 10cs viscosity silicon oil. The bright color of the top of square microposts suggests that the tops were not covered with thick film of oil.

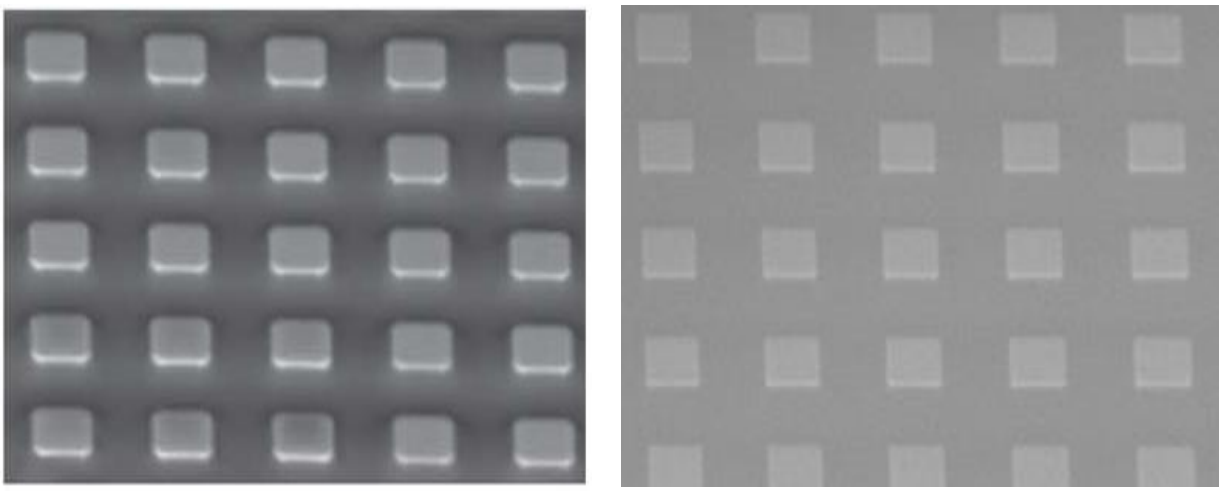

Figure 3.13 ESEM image for 10x10um texture impregnated with 10cs viscosity Si oil

3.7. Particle Adhesion Measurements

The nature of adhesion forces on flat silicon substrate, effect surface texturing on particle adhesion as well as the difference between particle adhesion behavior in dry and wet surface were determined using Atomic force microscopy (AFM). The below sections describe the Atomic Force Microscopy and the method of particle adhesion measurements.

3.7.1. Atomic Force Microscopy (AFM)

Atomic Force Microscopy (AFM) was invented in 1986 by **Binning et. al.[101]** and since then has been used as a tool for surface topography imaging. Now, it is widely used for surface force measurement. The unique capability of the AFM is to measure forces locally and with high sensitivity. Thus, this makes it possible to obtain information about the interaction between molecular pairs and material properties such as Hamaker constant and adhesion **[102]**. Using AFM, the interaction between the particles in a liquid can be studied. Also AFM can be employed to study the effect of humidity or temperature on adhesion between a surface and spherical particles. AFM has gained an edge over the other force measurement methods such as vibration and direct impact. In this study AFM was used to measure adhesion forces on flat and

textured silicon substrates. Multimode BRUKER and Asylum MFP 3D AFMs as shown in Fig.3.14 have been used for measurements. Colloid probe technique which was introduced by **Ducker et al. [103]** was employed to overcome the problem of tip' size , chemical composition and shape ,by attaching smooth spherical silica particle to the end of tipless AFM cantilever (represent dust particle). The cantilever spring constant has been calibrated using thermal noise method **[104]**. Friction properties of different flat and textured silicon substrates have been carried out by orienting the scanning direction perpendicular to the long axis of the cantilever. Humidity effect on vertical adhesion has been studied using humidity sensing cell. The following sub-sections describe in detail all the measurements using AFM.

Figure 3.14 Multimode BRUKER and Asylum MFP 3D AFMs

3.7.2. Silica Bead Attachment

Two approaches have been implemented to attach 5, 10, 20, and 48 um silica particles on AFM tipless cantilever. The manual (handy) approach was used to attach the 48um silica beads. The AFM approach was employed to attach 5, 10, and 20 um silica beads.

3.7.2.1.Manual Approach

The first step in the manual approach is to prepare two micro brushes by fixing brow hairs on the edge of sticks as shown in Fig.3.15a. One brush was used to apply epoxy, the other

to pick up the particles. Then, small amount of 2-ton epoxy was spilled on clean glass slide. At the same time the AFM cantilever and silica particle (beads were bought from Corpuscular) were placed under a good microscope with decent illumination. After that, the head of micro brush was carefully dipped with epoxy to avoid much amount of epoxy glue and directly under the microscope the head of AFM tipless cantilever was wetted with the epoxy glue. Then, using other brush, 48um silica bead was picked up (it will stick to the eye brow hair by static forces), and deposited on the epoxy on cantilever (The epoxy's meniscus forces will grab it and pull it off the eye brow hair) as shown in Fig.3.15b.

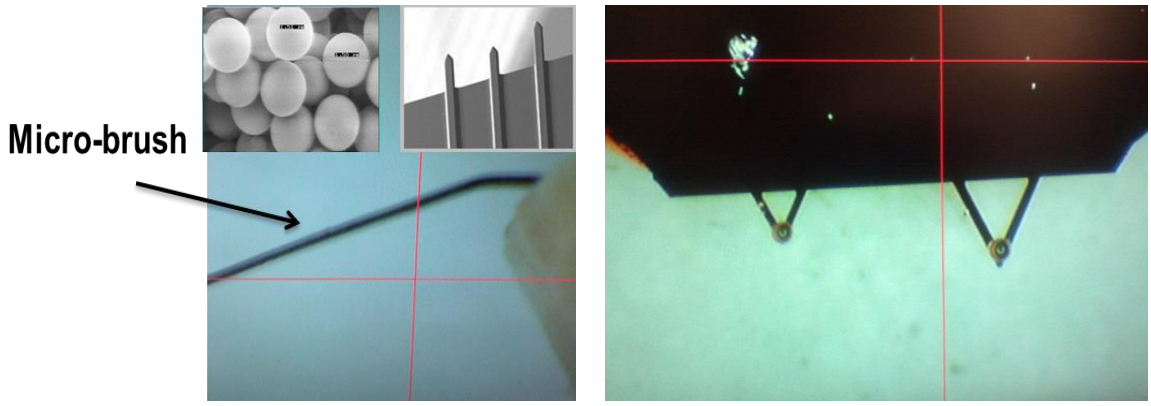

a. **b.**

Figure 3.15 Bead attachment using micro-brush

3.7.2.2.AFM Approach

The AFM approach consists of the following steps:

1. A thin layer of glue (2-ton epoxy) was made on one side of the clean glass slide and the silica beads were spilled on the other side as illustrated by Figure.3.16a.
2. At the same time, AFM tipless cantilever was installed and then started approaching the cantilever towards the glass slide manually using AFM screws such that the end of cantilever carefully touched the glue contaminated area of the glass slide.

3. The contaminated cantilever was manually retracted and moved to find a well isolated silicon bead.
4. Approached to the bead and in the meantime, the X-Y position of the stage was adjusted so that the end of the cantilever touched the bead in the middle of the tip (Figure.3.16b).
5. Gentle pushing on the bead is needed to be sure that beads attached to the cantilever.
6. The cantilever was slowly retracted from the surface. Now the bead is attached to the end of the cantilever. Before using it was kept for short time to get dried.

Figure 3.17 presents SEM images for 48um silica beads which were attached on Tip AFM cantilever with 5-10 N/m spring constant.

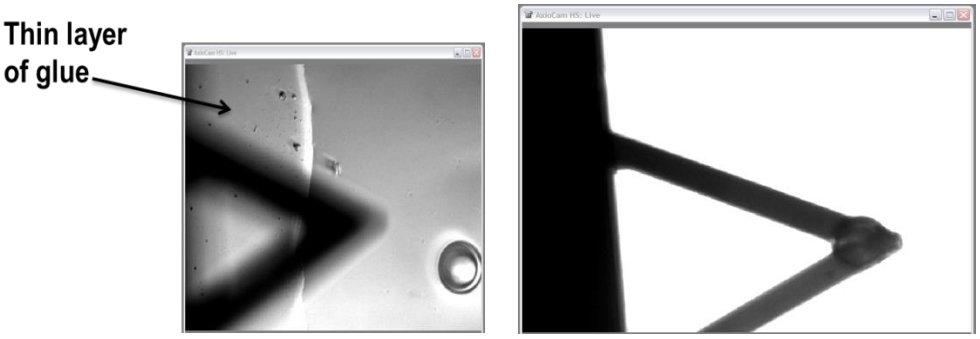

a. **b.**

Figure 3.16 Bead attached using AFM manipulator

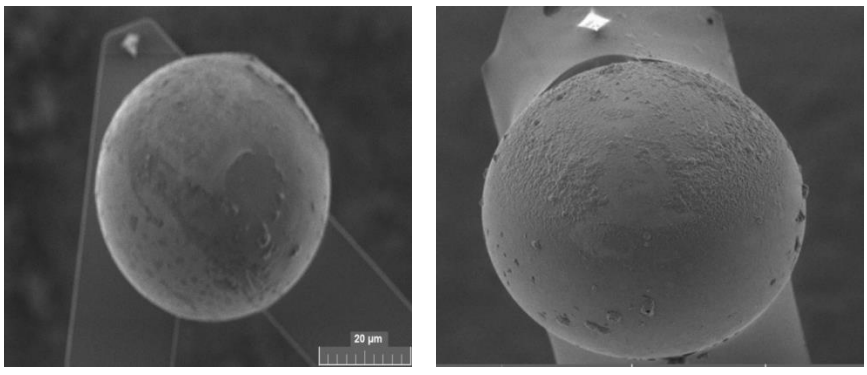

Figure 3.17 SEM images for attached 48um silica bead on AFM cantilevers

3.7.2.3. AFM Cantilever Silanization

For adhesion measurements on lubricant impregnated surfaces, the cantilevers were silanized prior to attaching the bead to prevent the chance of cantilever wetting thus losing the AFM forces curves stability. The clean cantilevers and an empty glass slide were placed inside the desiccator. Then 4 to 5 drops of the Trichloro (1*H*, 1H, 2H, and 2H-perfluorooctyl) silane were deposited on the empty glass slide. After that, the desiccator was closed and sealed under vacuum condition. After more than 4 hours the cantilevers were released from the desiccator. Small water droplets were deposited on the cantilever surface to check it hydrophobicity.

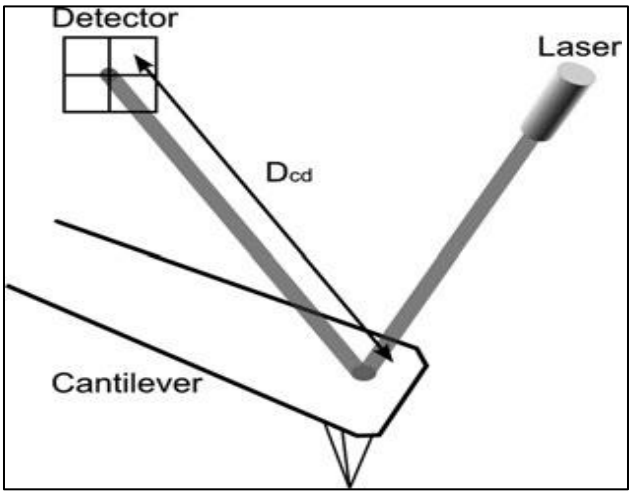

Figure 3.18 Reflected laser beam on the position sensitive detector [105]

3.7.3. Mechanics of Vertical Adhesion

The force measurement using AFM underlines basically on moving the cantilever or the sample up and down by applying a voltage on the piezoelectric translator, onto which the sample was mounted. Meanwhile the deflection of the cantilever was recorded using optical lever technique. A laser beam was targeted toward the end of cantilever back, so any cantilever deflection would be detected through the new position of reflected laser beam on the position sensitive detector as shown in Fig.3.18. The back of cantilever is usually coated with a thin film

of gold or aluminum to promote the surface reflectivity. Force curve presents the maximum vertical deflection of AFM cantilever when it was brought close to the surface, indented into it, and afterward retracted away to return to its initial position.

Figure 3.19 illustrates the mechanics of force measurement using AFM. In the beginning, the cantilever is far from the surface (point 1). Once voltage is applied, the probe starts moving downward. As the probe gets close to the surface, an attractive or repulsive force might deflect the cantilever either downward or upward. As soon as the generated attractive force during cantilever approaching become larger than the cantilever spring constant, the probe jumps into contact with the surface (point 2). Then the cantilever continues moving downward due to the applied voltage. So the cantilever deflection increases. The relation between the applied voltage and cantilever deflection which is implied as "cantilever sensitivity" can be extracted from the constant compliance region (i.e. linear region between point 2&3).The cantilever sensitivity primarily depends on material properties of cantilever and surface. At a certain voltage value, the process is reversed. At point 4, the cantilever starts retracting until reach to the zero deflection point (align with point 2). During the contact time with the surface, adhesion and bonds form, and as a result more deflection is needed to overcome the generated forces. The maximum cantilever deflection that is needed to retract the probe from the surface (distance between point 5&6) multiplied by the cantilever spring constant represents the magnitude of adhesion. After the bond is broken between the probe and surface, cantilever returned back to its initial free position (point 6).

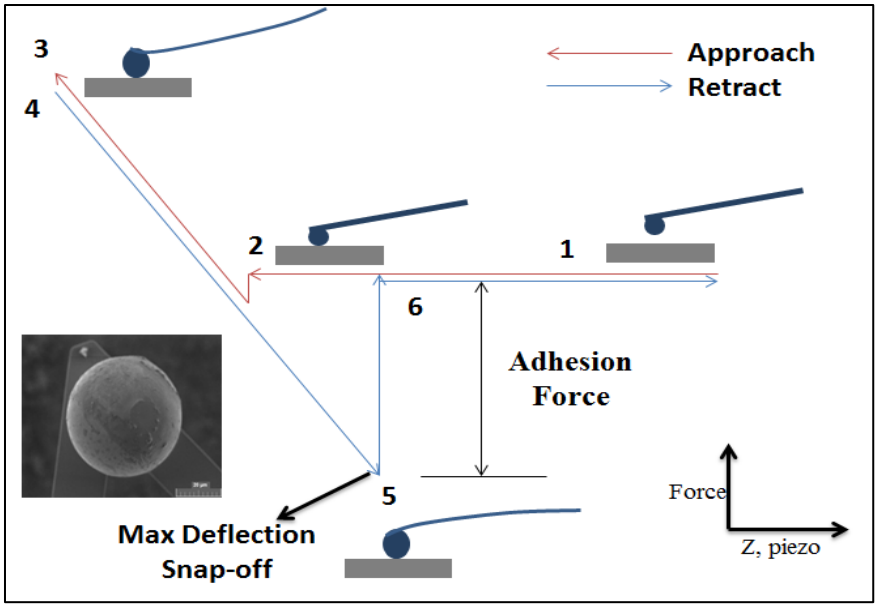

Figure 3.19 Approaching and refraction AFM force curves

3.7.4. Spring Constant Calibration

To obtain quantitative force measurements versus distance information, precise knowledge of the cantilever spring constant is a prerequisite especially that spring constants values of the cantilever given by the manufacturers are often not very reliable particularly after attaching bead on the cantilever. In this study, thermal noise method had been employed to calibrate the cantilever spring constant. The thermal noise method is based on the Equipartition Theorem of statistical mechanics that states that the mean thermal energy of any harmonic system at temperature T is equal to $k_B T/2$ per degree of freedom. The mean square deflection of a cantilever due to thermal fluctuations must satisfy the following condition:

$$\langle x^2 \rangle = \frac{k_B T}{K_c} \tag{3.1}$$

Practically, the thermal noise of the cantilever is recorded by measuring the deflection of the cantilever for some time while it is free in air far from any surface. Using recorded signals, the power spectrum P (ν), which is a plot of x^2 versus frequency, was calculated by fast Fourier

transform. The total value of x^2 would then be determined by the integral of the power spectrum given as:

$$\langle x^2 \rangle = \int_0^\infty P(\nu)\, d\nu = \frac{k_B T}{K_c} \tag{3.2}$$

The first resonance peak was fitted after subtracting background noise. Since thermal excitation acts as a white noise driving force, the power spectrum should follow the response function of a simple harmonic oscillator. The power spectrum is given by:

$$P(\nu) = \frac{A\nu_o^4}{(\nu^2 - \nu_o^2) + \left(\frac{\nu\nu_o}{Q}\right)^2} \tag{3.3}$$

Where, ν_0 and Q are the resonance frequency and quality factor of the first resonance peak. By combining eqs. (3.2&3.3) and solving the integral, we obtain:

$$K_c = \frac{2k_B T}{\pi A \nu_o Q} \tag{3.4}$$

3.7.5. Lateral Force Measurements

Lateral force microscopy (LFM) mode was used to determine the friction properties. The scan direction in this mode was perpendicular to the long axis of the cantilever. A friction force between the tip and the substrate will then lead to torsion of the cantilever and this in turn induced a lateral movement of the laser beam on the detector. By using a quadrant photodiode as shown in Fig.3.21, this lateral shift was recorded and allowed simultaneous recording of surface topography and friction.

A typical lateral deflection signal recorded for a single left/right scan cycle along a scan line is plotted in Fig 3.22. The upper and lower parts of this so-called friction loop results from trace (scanning left) and retrace (scanning right back on the same line). The width of the friction loop, which means the difference between the average values from trace and retrace, is proportional to the friction force.

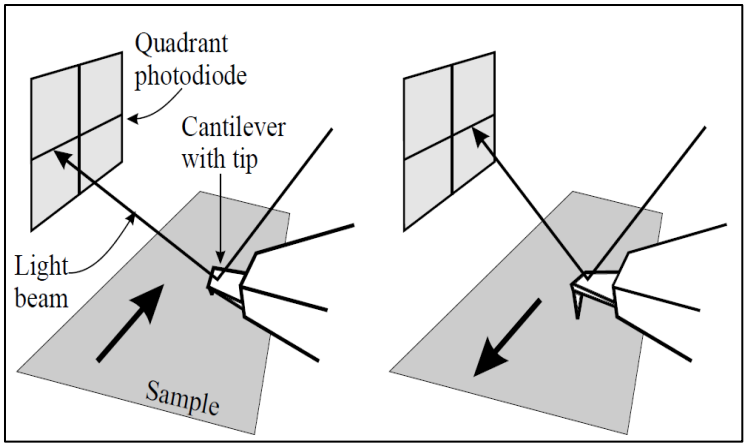

Figure 3.21 AFM lateral scanning microscope[44]

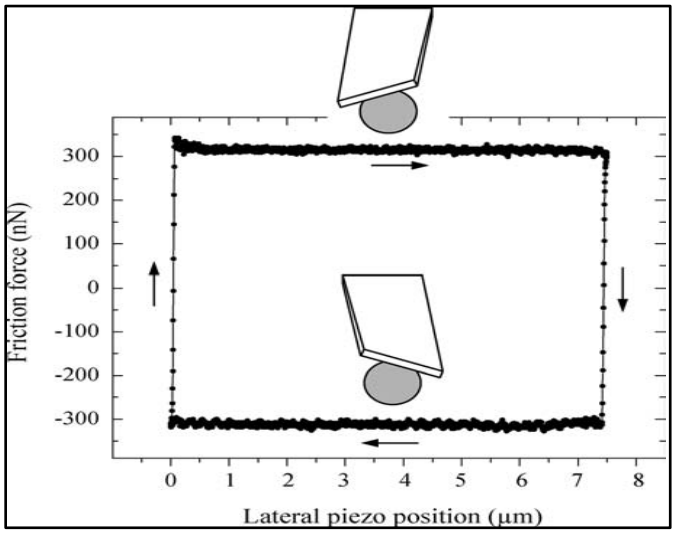

Figure 3.22 lateral movement of the laser spot on the photodetector (Friction Loop)[44]

3.8. Humidity Effect

Asylum MFP 3D AFM has been used to measure the surface forces under different relative humidity of surrounding gas. Humidity sensing cell was employed to control the humidity level. The Humidity Sensing Cell is a small sealed sample chamber with a dedicated side access port for the solid state humidity sensor. The sensor measures the relatively humidity of the air surrounding the sample and transmits it back to the AFM controller. The MFP-3D software displays humidity as a function of time. The sample cell is based on the Closed Fluid

Cell (Model CCELL) which accepts samples of up to 30mm in diameter. Samples were mounted on a glass disc which forms the bottom of the cell. Optical access is available from above and below the sample. A clamp and FKM (Viton® equivalent) membrane fit on the top of the cell for an air tight seal as shown in Fig.3.21c.

A Humidity control has been accomplished by flowing a mixture of dry and wet nitrogen gas through one of the access ports as shown in Fig.3.21a&b. The sensor is used to confirm the relative humidity value of the supplied gas and serves as a guide for adjusting the valves to the desired relative humidity level. The cell has four available 1/16" diameter access ports and three 0.036" ports.

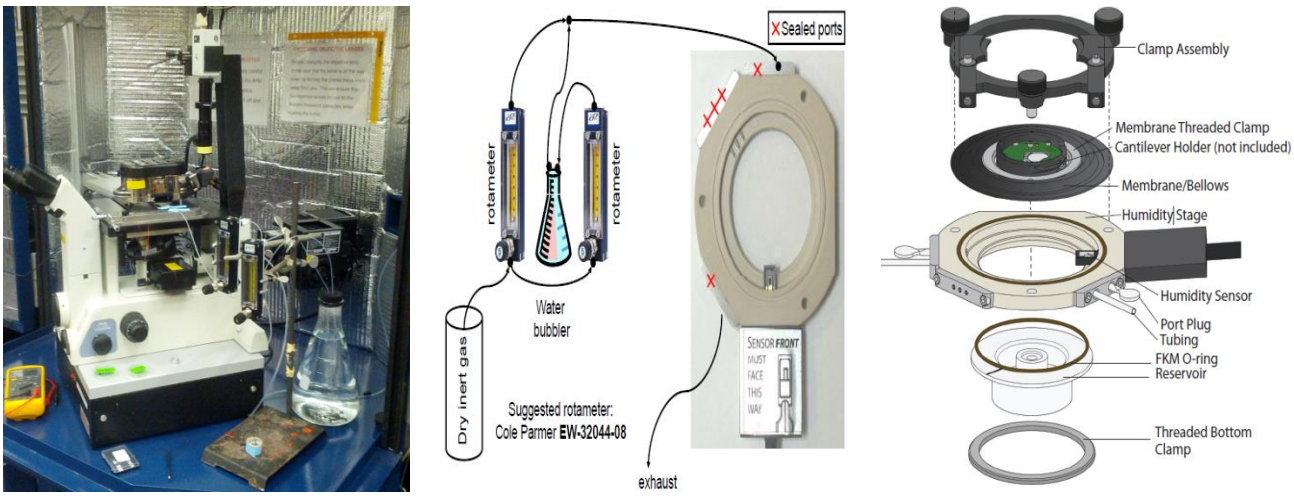

a. **b.** **c.**

Figure 3.21 Asylum MFP 3D AFM Humidity Sensing Cell and Control

CHAPTER 4

RESULTS & DISCUSSION

4.1. PV Modules Performance

The effect of solar radiaon on PV module power output , effect of temperture on module efficiency , effect of dust accumulation on PV module power output and the role of glass anti-reflective coating in enhancing the module performance are presented in the following sections:

4.1.1. Module Power Output and Solar Radiation

The power output of PV modules is proportional to the magnitude of solar radiation. Fig.4.1 shows variation of solar radiation and module generated power output during the day time. The module has maximum power at noon because of high solar radiation and because of the direct incidence of solar beam. After noon time, the generated power starts decreasing due to reduction the solar intensity and the change of angle of solar beam incidence. The PV module short-circuit current, open-circuit voltage, Fill Factor, and efficiency are all dependent on the intensity of solar radiation. Increase in solar radiation increases the generated short circuit current and as a result module power output as shown in Fig.4.2.

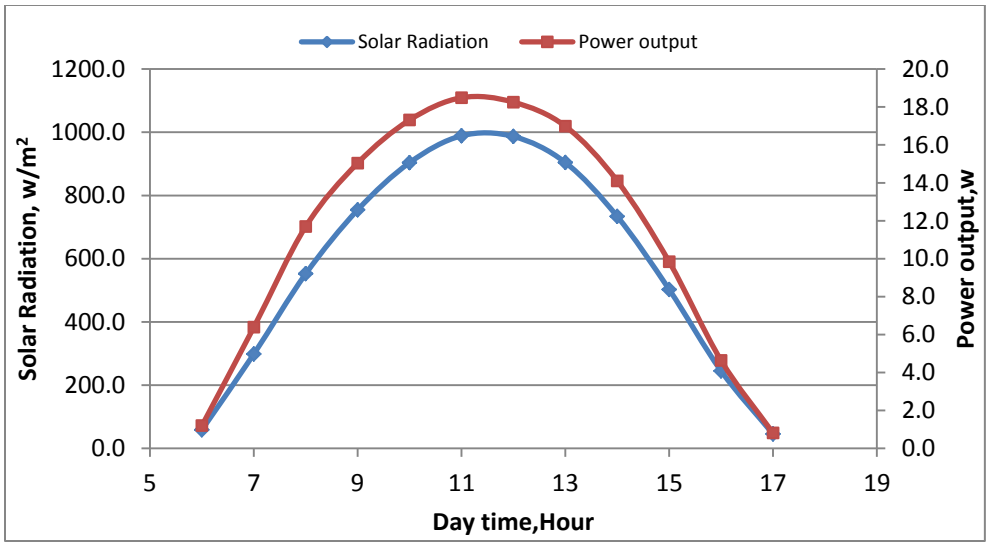

Figure 4.1 Solar radiation effects on module power output

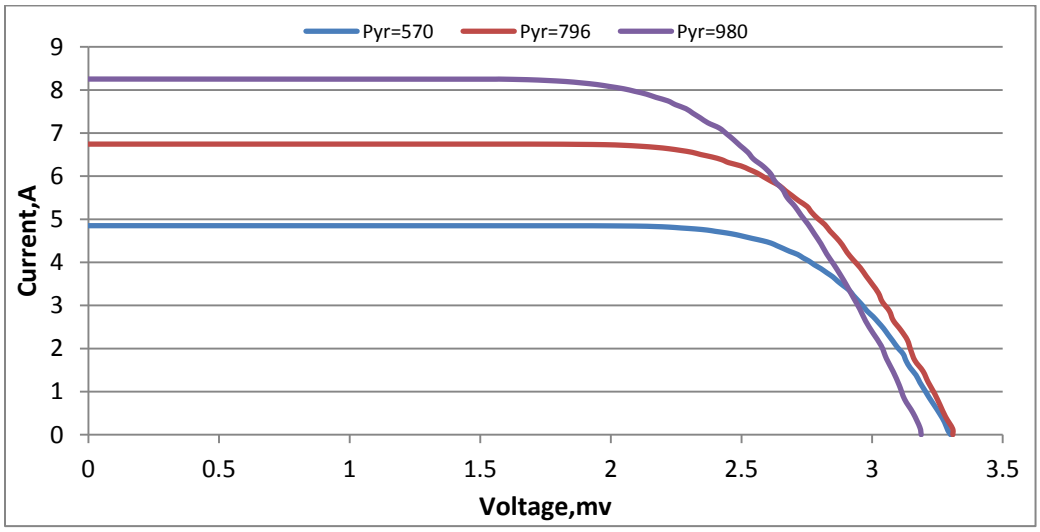

Figure 4.2 Solar radiation effect on module I-V curves

4.1.2. Module Temperature and Fill Factor/Efficiency

The back temperature of PV modules depends primarily on the PV module encapsulating material as well as the atmospheric parameters. Figure 4.3 shows that increasing module temperature reduces module power output and hence its efficiency. As the module temperature increases; the band gap of the encapsulated cells usually decreases resulting in absorption of longer wavelength photons. In addition, as module temperature increases, the minority carrier

lifetime generally increases. Both of these factors will slightly increase the light generated current I_{sc}, but lead to reduction in the cell's open circuit voltage (V_{oc}). The decrease in V_{oc} is large rapid than the increase in I_{sc}, resulting in an overall reduction in the module's fill factor, and hence, its efficiency as shown in Figs (4.3&4.4).

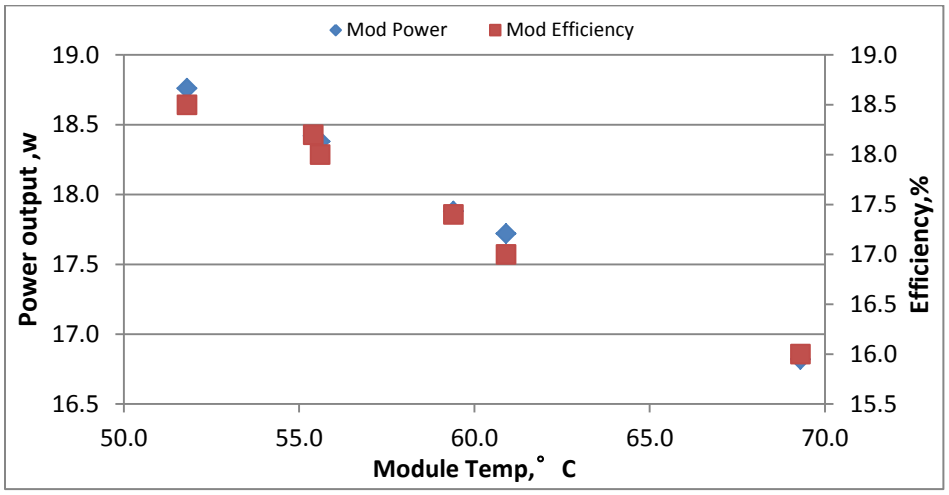

Figure 4.3 Effect of module temperature on module power output and efficiency

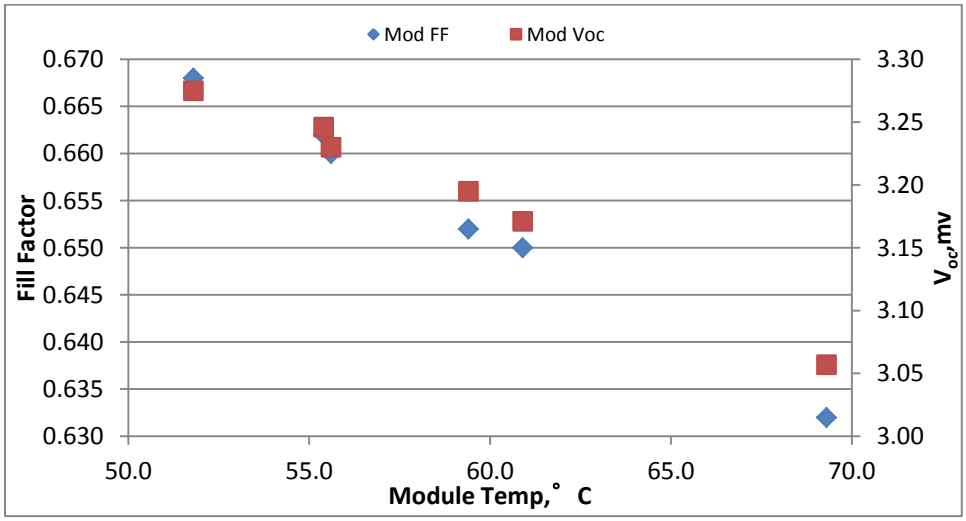

Figure 4.4 Effect of module temperature on module open circuit voltage fill factor

4.1.3. PV Modules Power Output

Figure 4.6 presents the normalized weekly average maximum power output for three PV modules. The difference between the modules is the type of glass cover. Centrosol C+ and SG plane modules have plane glass surface. Centrosol C+HiT has a surface coated with anti-reflective material.

Centrosol C+ HiT module showed the largest power output as shown in Fig.4.6. The reason for that is reffered to the effect of anti-reflective coating which enhances the surface optical properties. More surface transmissivity leads to more transmissivity of solar flux which in turn increases the amount of genereated current as well as the voltage as shown in Fig.4.7.

The power output decreases with the increase in the duration of outdoor exposure for all types of PV modules; due to the dust accumulation on the PV modules glass cover. The average power reduction after five weeks of outdoor exposure is around 15%. Centrosol C+ HiT module exhibited the maximum power output. The reason being the low reduction of Centrosol C+ HiT transmittance due to dust compared with the other types of modules as shown in Fig.4.14. After the sixth week of expsure , the modules recover their rated power due the rainful.

The dust accumualtion maily affects the short circuit current ;since the generated current mainly depends on surface transmittance (i.e. transmitted solar flux). Thus it is sensetive to any small change in surface trasmissivity due to dust accumulation. The average reduction in the short circuit current is around 20% after 5 weeks of exposure as shown by Fig.4.7.

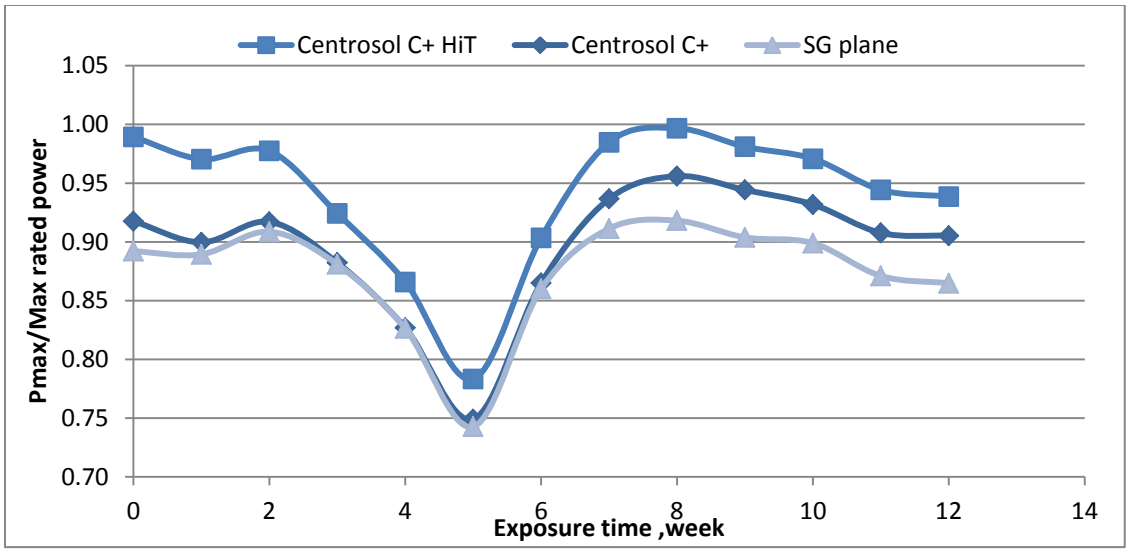

Figure 4.5 Weekly normalized maximum power output

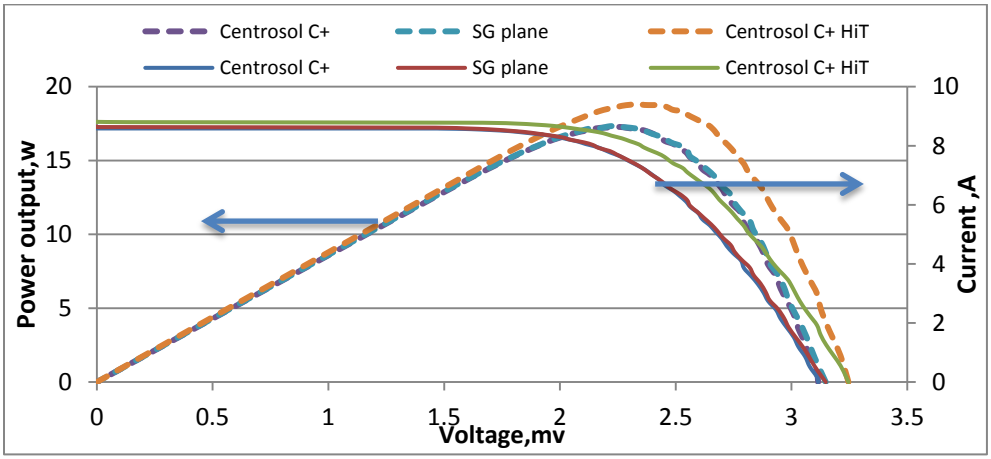

Figure 4.6 I-V and P-V curves for clean modules

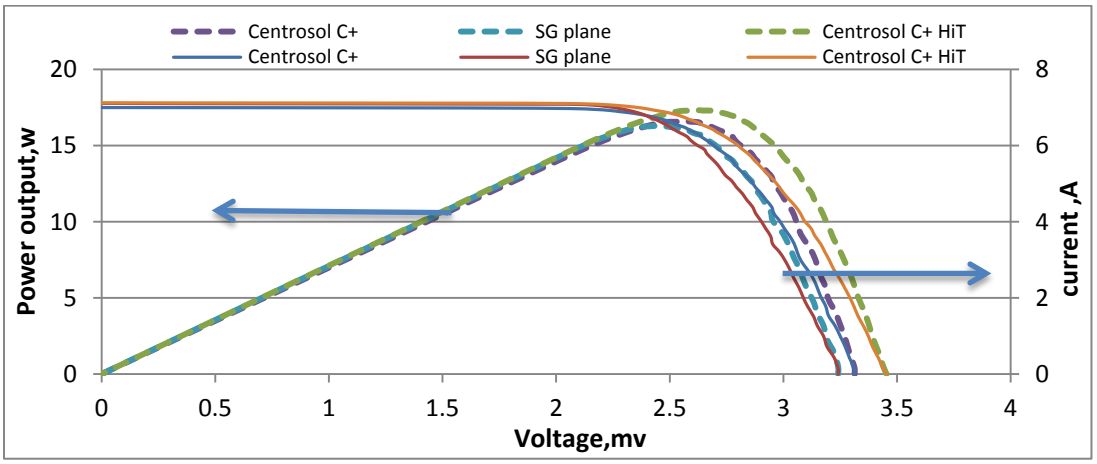

Figure 4.7 I-V and P-V curves for dusty modules

Centrosol C+HiT module temperature was slightly larger than the temperature of the other modules. This is atrribtuted to fact that the anti-reflective coating enhances the trasnmissivity of solar radiation and this in turn lead to more heat absorpion by the module particularly during the noon time as shown in Fig.4.8.

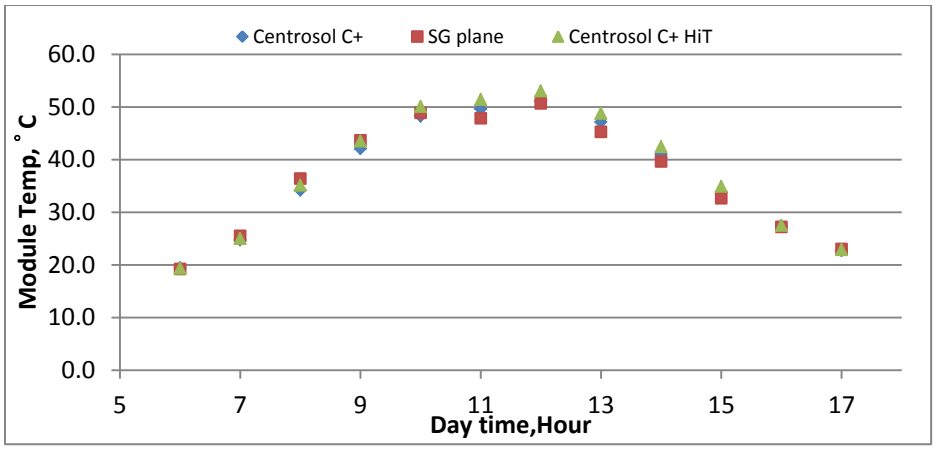

Figure 4.8 Clean module temperatures during the day time

Centrosol C+HiT showed better performance during the period 9:00AM to 2:00PM which indicates the ability of nano-textured surface in enhancing the surface transmissivity by capturing diffuse radiation in addition to direct one as shown in Fig.4.9.

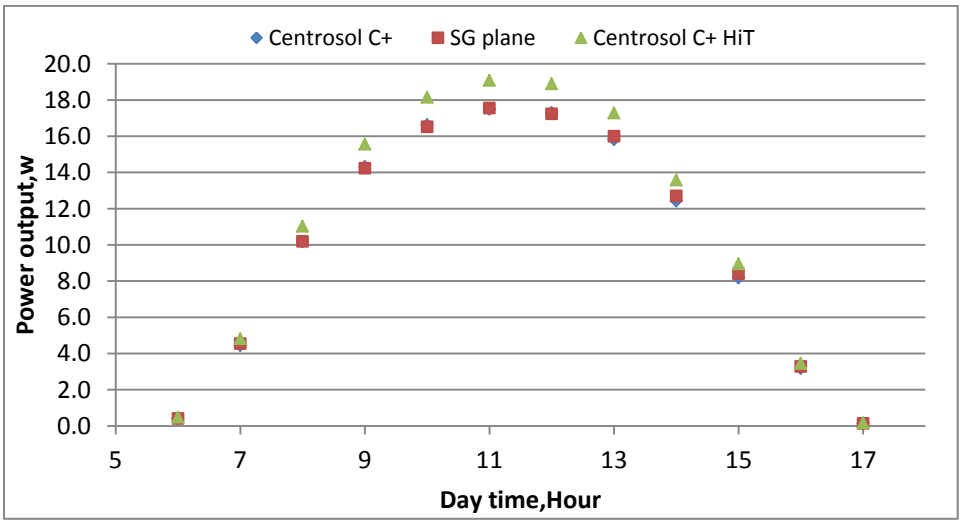

Figure 4.9 Clean module power output during the day time

4.2. PV Modules Glass Cover

The glass surface roughness , glass surface wetting properties and the glass spectral transmittance reduction due to dust fouling are discussed in the following sub-sections:

4.2.1. Glass Surface Roughness

Figure.4.10 shows AFM topography images for the three tested glasses. It is clear that Saint Gobain plane has the smoothest surface with around 0.6 RMS roughness compared to Centrosol C+ which has 1.5 RMS roughness as shown in Table 4.1. Coating the surface with thin film of anti-reflective materials leads to enhance roughness properties as indicated by Centrosol C+ HiT RMS and average roughness values.

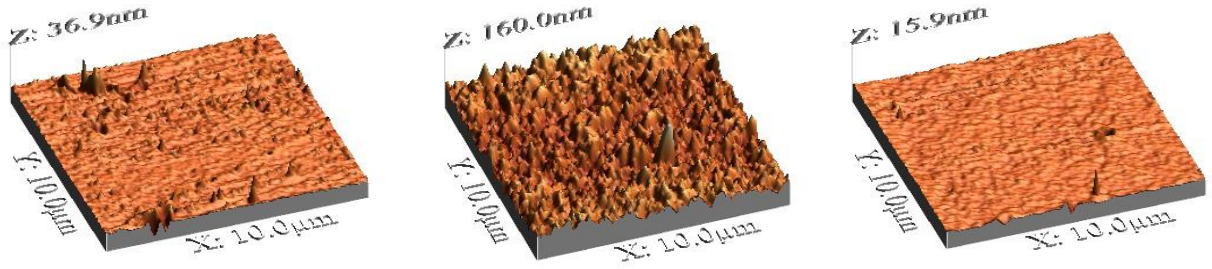

Centrosol C+ **Centrosol C+ HiT** **Saint Gobain Plane**

Figure 4.10 Glass surface topography

Table 4.1 RMS and average surface roughness parameters

Glass Type	RMS Roughness(nm)	Average Roughness(nm)
Centrosol C+	1.5275	0.7875
Centrosol C+ HiT	12.9	10
Saint Gobain Plane	0.566	0.356

4.2.2. Glass Surface Wetting Properties

Wetting properties test indicated that all tested glass types are considered hydrophilic; because their contact angle is less than 90° as shown in Table 4.2. The differences between the contact angle values of the tested glass types is attributed to the difference in their surface

roughness as can be explained by Wenzel equation for wetting **[46]**. Wenzel reported that increasing the surface roughness of hydrophilic surface leads to enhance its wetting properties, in other words reducing the contact angle as indicated by the case of Centrosol C+ HiT. There is no significant difference between the values of contact angles for saint Gobain and Centrosol C+, because of the small difference between the values of their surface roughness.

In case of hydrophilic surface , water droplet stick on the surface and a by the time the area of contact starts to expanding along the surface which drive to reduction the contact angle as shown in Fig.4.11.

Table 4.2 Contact angle measurements

Glass Type	Contact Angle , deg
Centrosol C+	40.50±8
Centrosol C+ HiT	33.30±5
Saint Gobain Plane	47.10±10

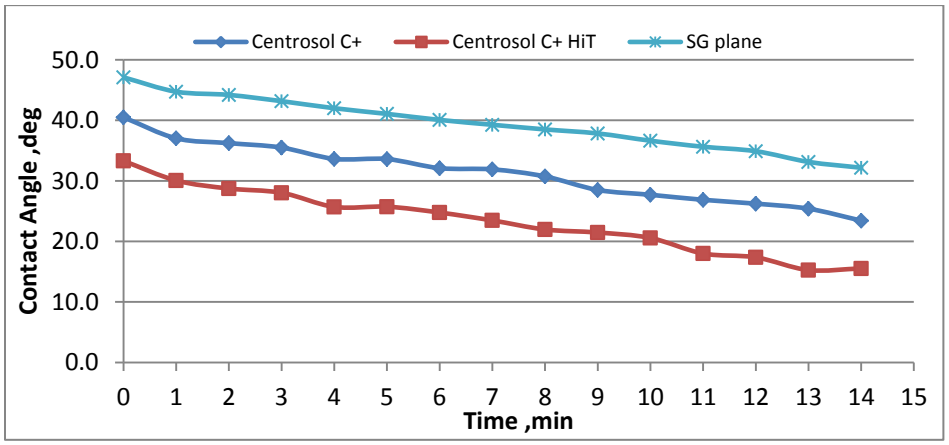

Figure 4.11 Contact angle time variations

4.2.3. Glass Optical Properties

Surface roughness reduces the amount of scattered light. Figs (4.12-4.14) indicate that Centrosol C+ HiT has the best transmittance properties. The reason being the effect of anti-reflective coating. The presence of thin film made the surface more rough and this in turn lead to

enhance internal reflection and reduction outward reflection of solar irradiance **[106, 107]**. This is true if the scale of surface roughness is less than wavelength of incoming solar irradiance.

The morphology of glass surface plays a role in the amount of dust deposition. Van der Waal adhesion force primarily depends on contact area between particle and surface. Roughening the surface causes a reduction in area of contact and increases the distance between particle and surface. This explains why Centrosol C+ HiT showed the lowest transmittance reduction as shown in Fig.4.14.

More days of exposure means more dust accumulation and hence more solar irradiance transmittance reduction. The normal plane glasses (Centrosol C+ and saint Gobain) experienced around 37% reduction in transmissivity compared to anti-reflective coated glass which experienced less than 30% reduction as indicated in Figs (4.12-4.14). However, the amount of transmittance reduction is not uniform and depends on climatic conditions and frequency of sand storms.

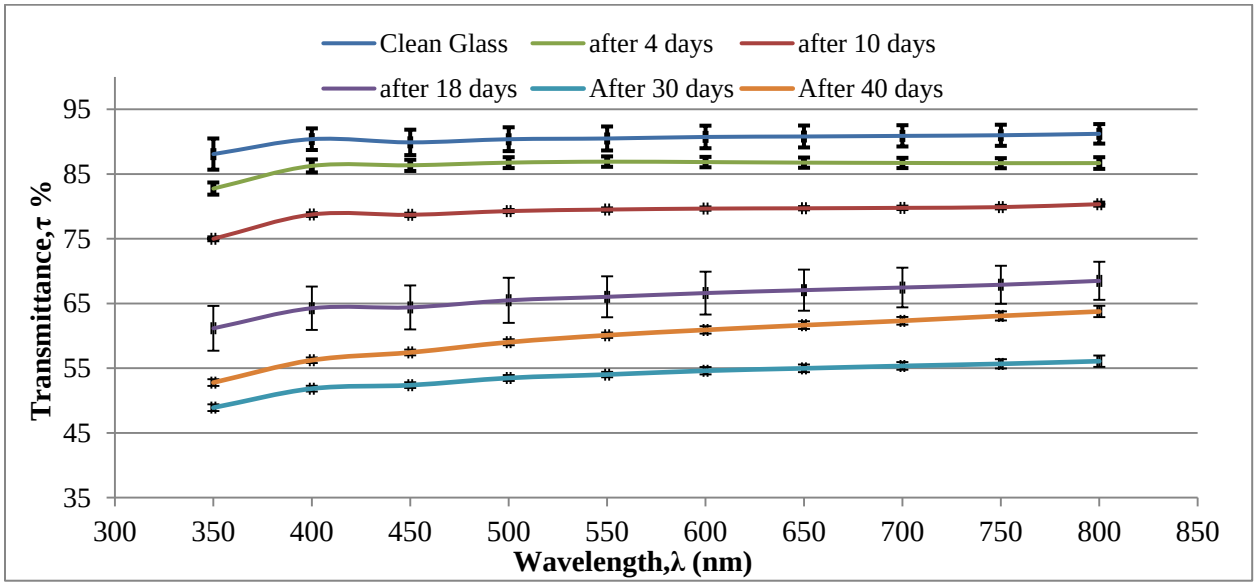

Figure 4.12 The spectral transmittance for Centrosol C+ glass for different exposure periods

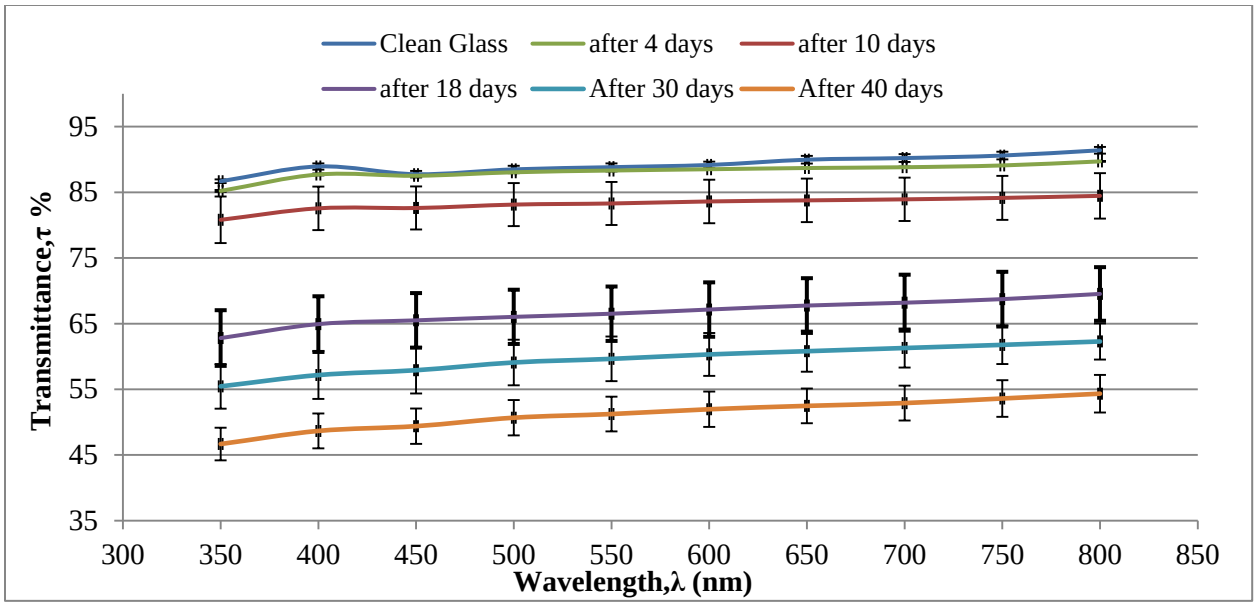

Figure 4.13 The spectral transmittance for Saint Gobain Plane glass for different exposure periods

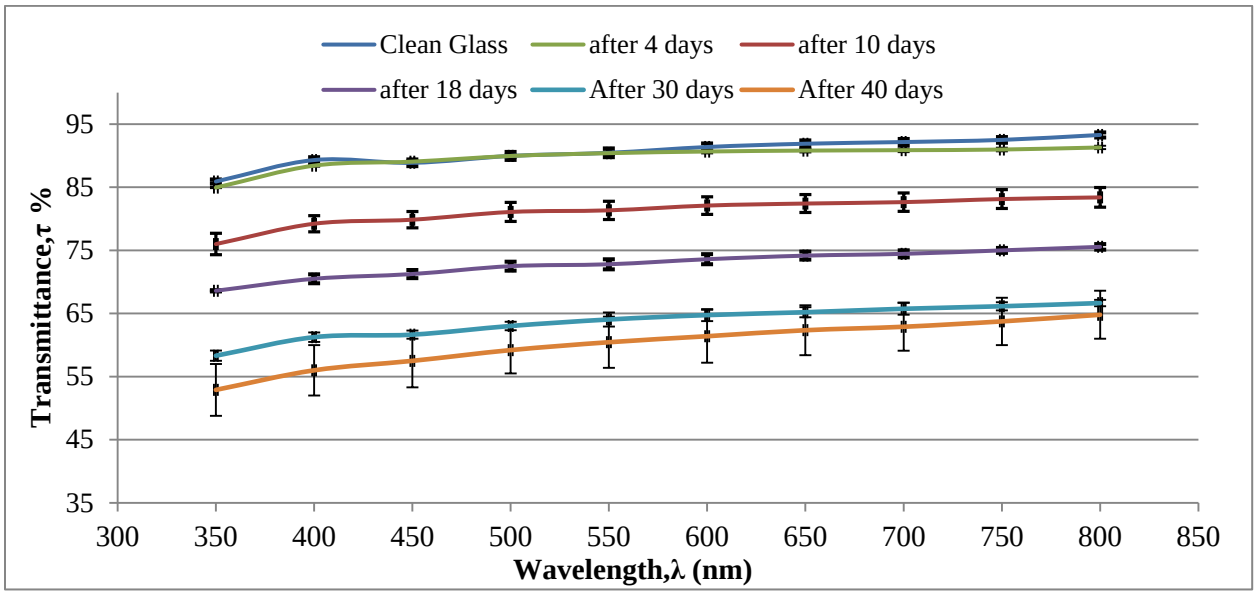

Figure 4.14 The spectral transmittance for Centrosol C+ HiT glass for different exposure periods

4.3. Dust Particle Characterization

The dust characterization study included dust chemical composition analysis , dust particle size analysis and dust particles morphologies and interactions as shown in the following sub-sections:

4.3.1. Dust Particle Chemical Analysis

The elecmetal anylasis for the chemical composition of dust particle were carried out using Energy Despersive Spectroscopy (EDS), X-Ray Flourecence (XRF) and X-Ray Diffraction (XRD).

4.3.1.1. Chemical Elements Analysis

Figure.4.15 shows the average element percentage weight of XRF and EDS chemical element analysis for number of dust samples. It is observed that oxygen has the highest chemical concentration followed by calcium, silicon, sulfur, and iron. The rest of composition includes magnesium, sodium, potassium, aluminum, chlorine, and titanium.

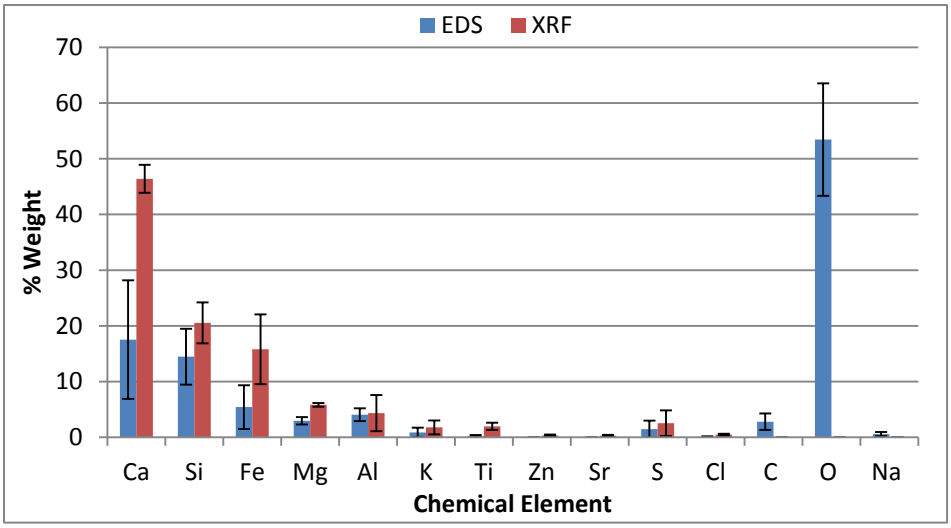

Figure 4.15 EDS and XRF chemical element analysis

4.3.1.2.Chemical Compound Analysis

In order to quantify the chemical compound of dust particles, qualitative and quantitative analysis were carried out. Figure 4.16 shows the XRD peaks for three different dust samples. The samples were collected from different modules. It can be observed that there is no obvious difference in the samples chemistry. The factors that can influence the dust chemical

composition are installation site and human activities around it. The samples were collected from the same testing site. It is observed that calcite and quartz compounds occupied more than 50% of dust particle content as shown in Fig.4.17 and Table 4.3.

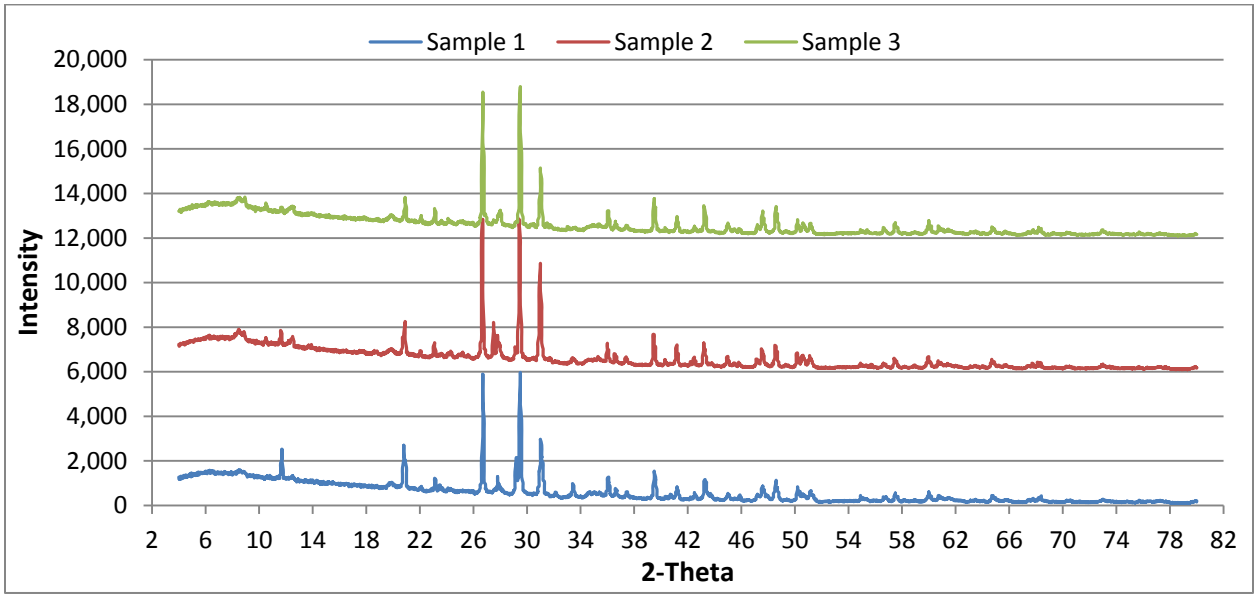

Figure 4.16 XRD peaks for three different dust samples

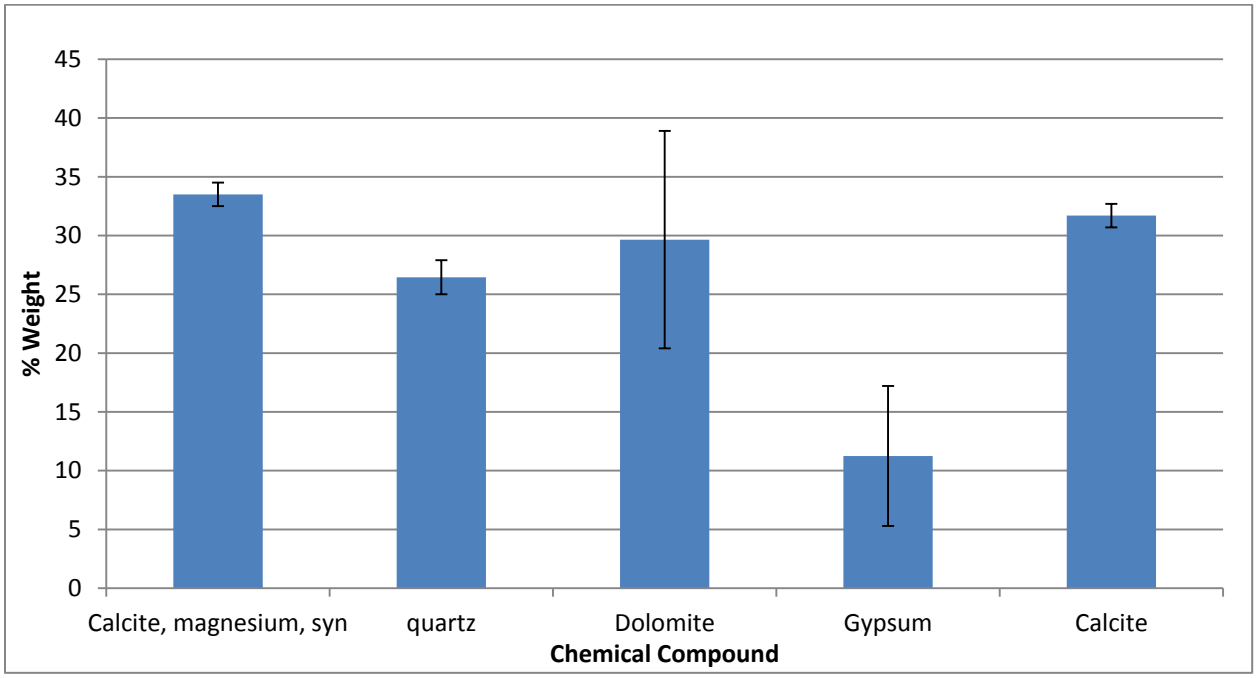

Figure 4.17 XRD qualitative and quantitative analysis

Table 4.3 XRD qualitative and quantitative analysis

Phase name	Phase Symbol	AVG(%Content)	STD
Calcite, magnesium	(Mg0.03 Ca0.97) (C O3)	33.5	1
quartz	Si O2	26.45	1.45
Dolomite	Ca Mg (C O3)2	29.65	9.25
Gypsum	Ca (S O4) (H2 O)2	11.25	5.95

4.3.2. Particle Sizing Analysis

The distribution of the number, surface area and volume as a function of particle size (diameter of the particle) are reported in Table 4.4 and Fig.4.18. It is worth to mention that the fractions are not absolute values, but are relative to the totals in each case. The system is capable of measuring particles size in the range of 0.25µm up to 2800µm. The % of the fraction of particles distributions are shown in Fig.4.18. The relative distribution of the number of particles indicates that most of the particles have a diameter in the range between 0.5 and 1.5 µm. The maximum population particle size is around 0.60 µm, and the mean number diameter (MN) is about 0.80 µm. It is observed that the particles mean area diameter (MA) is around 5.25 µm, and that around 90% of the total area is occupied by particles that have a diameter less than 13 µm size. In case of volume distribution, mean volume diameter (MV) is 17.5 µm and around 90% of the total volume is occupied by particles that have less than 35 µm size.

In general, it can be concluded that the minimum particle size is 0.5µm and the maximum one is176 µm. Figure 4.19 shows that the Graphic Skewness is 0.35 and this means that the fine particle has more influence on particle distribution. On the other hand, Kurtosis (peakedness) of the plot of the number distribution is positive and more than 1 which in turn indicates that the particles concentrate in a small size range .Such type of curve is called leptokurtic (Greek meaning “slim”). However most of the particles have a size less 2µm as shown by the curve for area and number distribution. In fact that particle size is enough to reflect and scatter the light

beam and hence reduce the amount of transmitted light through the glass surface. Also, the results indicate that there are a small number of large particles (more than 10µm size to be precise) which occupy a largest fraction of the total volume and have greater impact in scattering the light beam.

Table 4.4 Number, area, and volume Software selectable Percentile Points in microns

Number Percentiles		Area Percentiles		Volume Percentiles	
%Tile	**Size(um)**	**%Tile**	**Size(um)**	**%Tile**	**Size(um)**
10	0.464	10	0.598	10	2.246
20	0.502	20	0.763	20	4.58
30	0.539	30	1.017	30	6.92
40	0.577	40	1.459	40	9.29
50	0.623	50	2.177	50	11.84
60	0.681	60	3.35	60	14.82
70	0.76	70	5.28	70	18.65
80	0.89	80	8.23	80	24.38
90	1.196	90	13.43	90	36.07
95	1.644	95	19.01	95	54.06

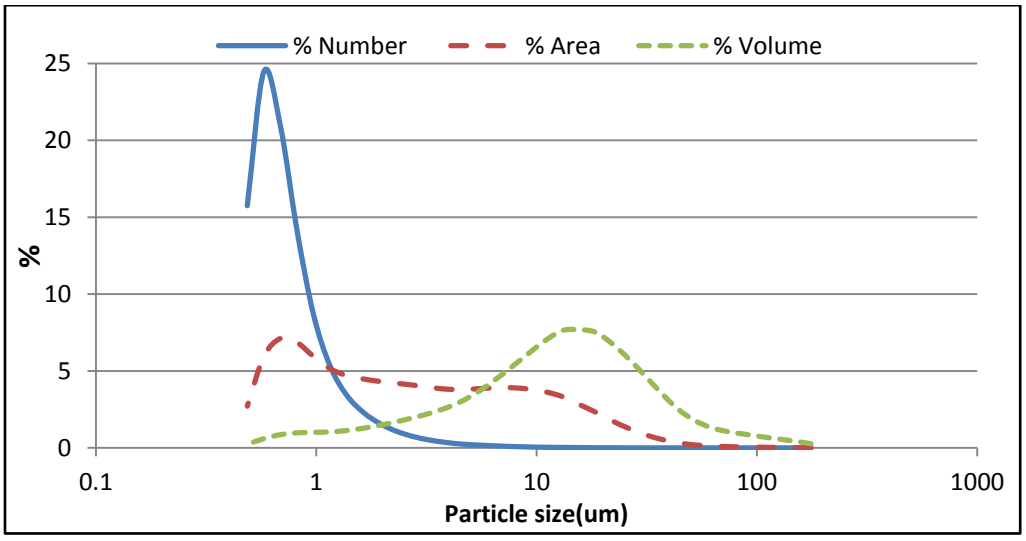

Figure 4.18 Distribution transformation

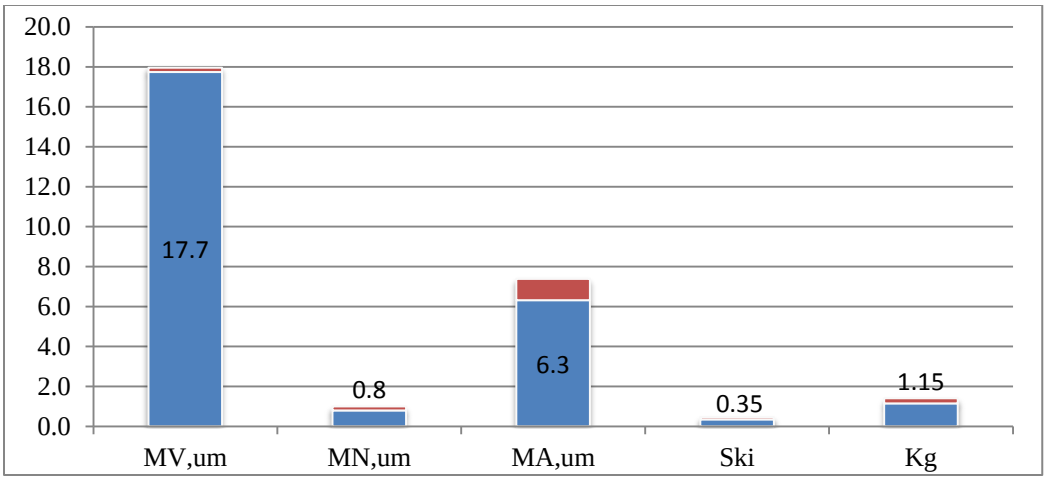

Figure 4.19 Distribution statistical parameters

4.3.3. Morphology and Interaction

Field Emission Scanning Electron Microscope (FESEM) was used to determine the morphology of dust particle as well as the nature of interaction between the dust particles. Figures (4.20-4.22) indicate that the dust particles have various and irregular shapes, but in general, tend to be spherical. **Otsuka et. al. [82]** reported that the shape of the particle has a strong effect on the adhesion force. The adhesion force increases as the particles become more spherical in shape; because the contact area with the surface is larger for the spherical particles. Regarding the irregular shape particles, the contact area depends on the orientation of these particles. From the particle sizing analysis and SEM images, it can be observed that dust samples contain fine and coarse particles. The fine particles are the largest in number which confirmed what was concluded in particle analysis section.

Fine particles tend to reduce the adhesive force between the coarse, large particles and the surface. Figure 4.20 indicates that fine particles settle on the surface of the large particles. If a surface is covered with fine particles this leads to reduction in the contact area between the large particles and the surface due to gap formation as indicated by **Otsuka et. al.[82]**.

Figure 4.21 shows groups of spherical particles. The important observation that can be made is the high cohesion forces between the spherical particles, compared to irregular particles.

Figure 4.22 shows dust particle settlement on glass surface. It can be observed that the fine particles stuck strongly and are uniformly distributed on the surface. On the contrary; large or coarse particles showed weak sticking to the surface that surface inclination or air blowing is enough to remove them. This is due to the morphology of dust particles which is described as rough. As result the adhesion force will be reduced due decrease in the contact area between large particles and the surface.

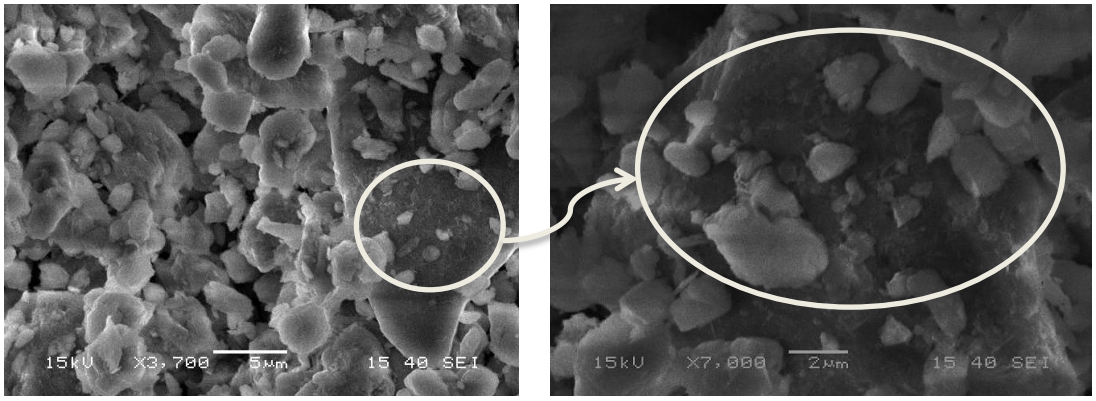

Figure 4.20 The SEM images of the fine particles

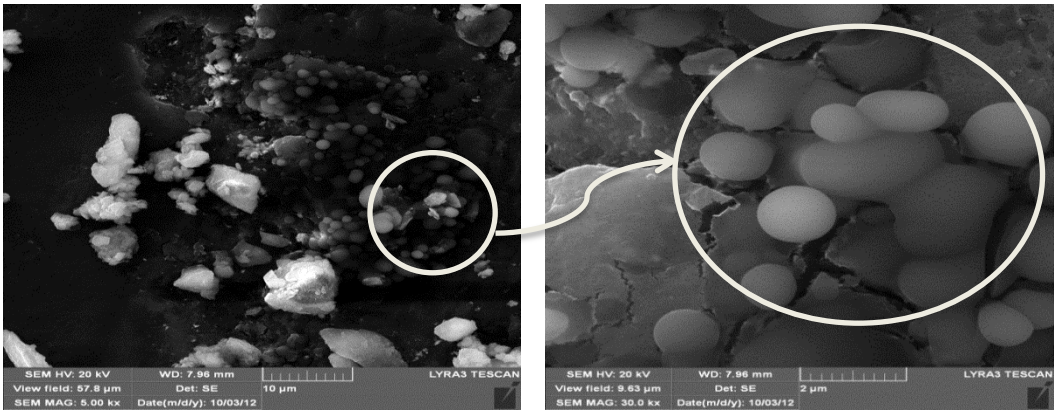

Figure 4.21 The SEM images of the cohesion spherical dust particles

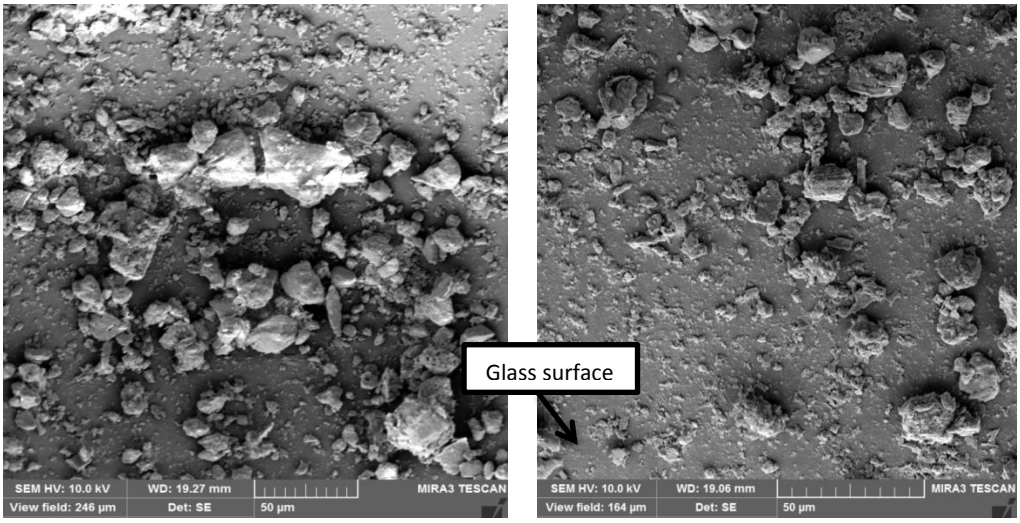

Figure 4.22 The SEM images for fine particles distribution

4.4. Particle-Surface Adhesion

The magnitude of adhesion force between different sizes of silica particle and flat silicon substrate , effect of surface texturing on partcile adhesion , adhesion force on liquid surface and the effect of humidity on particle adhesion forces are presented in the following sections:

4.4.1. Adhesion on Flat Silicon Substrate

Adhesion between a particle and a surface depends mainly on contact area between the particle and the surface. Hence; particles with large size do experience large adhesion force. The adhesion between different sizes of silica particle (Beads) and a flat silicon substrate are measured using AFM and calculated using Johnson-Kendal-Roberts (JKR) **[66]** and Derjaguin-Müller-Toporov (DMT)**[67]** models. JKR and DMT models describe the adhesion forces between smooth particles and smooth substrate. Adhesion force is a linear function of particle size and effective solid surface energy for both particle and substrate. Johnson-Kendal-Roberts model is written as:

$$F_{JKR}=3\pi\gamma R \qquad (4.1)$$

While Derjaguin-Müller-Toporov model is written as:

$$F_{DMT}=4\pi\gamma R \qquad (4.2)$$

Where: γ is surface energy, J/m^2, and R is particle radius

Both measured and calculated results are shown in Fig.4.23. The average surface roughness of silicon substrate is 0.5nm. The measured values of adhesion were compared with value obtained using DMT and JKR models. There is a clear discrepancy between the two values due to irregularities of the surface morphology of substrate and particles, surrounding effects such as humidity and temperature, electrostatic effect and instrument accuracy **[108]**. Surface energy has been calculated by substituting the measured adhesion value in eqs.4.1&4.2 and compared with published values **[109]**. The average calculated value was around $0.02J/m^2$ which is in a good agreement with published data.

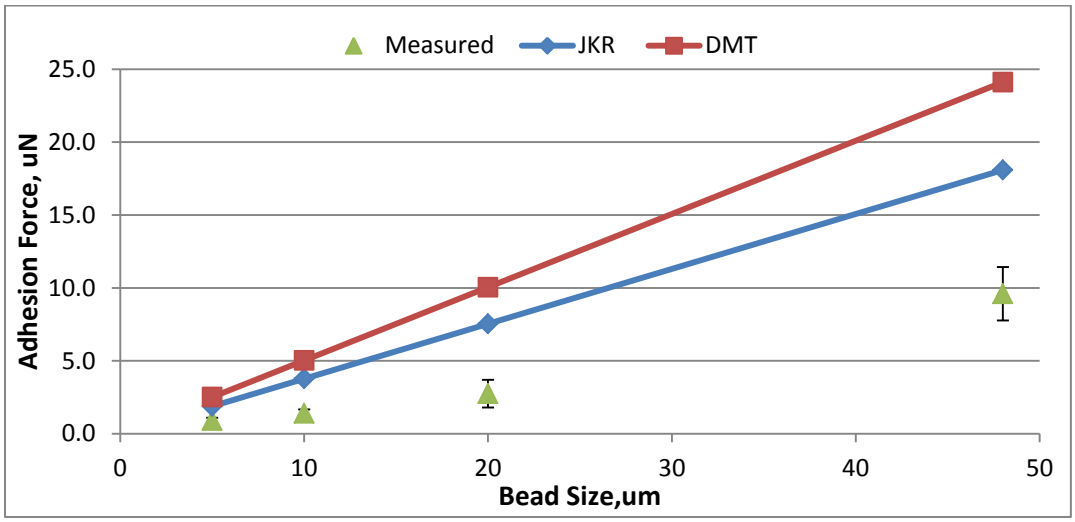

Figure 4.23 Effect of particle size on adhesion force

4.4.2. Adhesion on Dry Flat Silicon Substrate - Effect of humidity

In order to understand the effect of humidity and water vapor condensation on the magnitude of adhesion forces between particles and a planar surface ;a systematic adhesion force measurements between AFM tip/silica particle and hydrophobic/hydrophilic planar surfaces have

been carried out under different humidity levels. The presence of condensed water in the gap between the particle and surface leads to build capillary bridges. The nature of capillary bridge depends on humidly level as well as particle and the surface morphologies and shapes. The capillary force between a particle or a tip and a planar surface has two components. The first component is the force that is produced by the Laplace pressure (pressure difference between meniscus interfaces). The second component is the vertical component of surface tension as given by the following equation **[92]**:

$$F_c = F_P + F_S = \pi x^2 \Delta P + 2\pi \gamma_L x sin(\theta_1 + \alpha) \tag{4.3}$$

Where the pressure difference

$$\Delta P = \gamma_L \left(\frac{1}{x} - \frac{1}{r}\right) \tag{4.4}$$

γ is the surface tension of liquid, *R* is the radius of the adhering particle, *r* is radius of the meniscus, *x* is horizontal distance of intersection between the meniscus and the adhering particle, θ_1 is the contact angle of water of the particle, and α is the angle between the ordinate axis and a radius to the intersection of the particle with the liquid meniscus as shown in Fig.4.24.

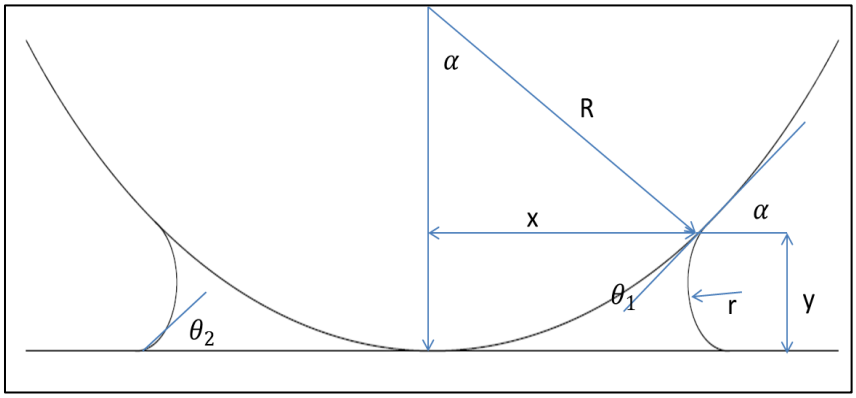

Figure 4.24 Water meniscus geometry

4.4.3. AFM Tip Adhesion on Flat Silicon Substrate

Figure 4.25 shows the effect of humidity on the adhesion between AFM tip and hydrophilic and Hydrophobic silicon planar surfaces. AFM tip size is around 4-10 nm. It can be observed that the adhesion increases with increase in humidity due to the formulation of a capillary neck between the tip and the surface. The increase stopped at a certain humidy value then the adhesion starts to decrease as shown by Fig.4.25a. This behavior can be explained by the following. Based on equation 4.4 as x>r, the curvature of the meniscus is negative, that is, the pressure in the liquid is lower than in the outer vapor phase. It acts upon the cross sectional-area πl^2 leading to an attractive force of $-\pi l^2 \Delta P$. As the humidity increases, the curvature meridional radius (r) becomes larger than azimuthal one (x) as shown by in Fig.4.27a. As a results the Laplace pressure becomes positive and its effect converts to repulsive force **[91]**.

There is no significant effect for humidity adhesion force between tip and hydrophobic surface as shown in Fig.4.25a. Hydrophobic surfaces reduce the probability of vapor condensation especially at low humidity. The non-wetting properties of the surface prevent capillary bridge creation which is on the contrary happened in case of hydrophilic surfaces **[76, 91]**.

The results were compared with published results shown in Fig4.25b **[91]**. There is a large difference in compared values especially in the range of 40-90% relative humidity as well as differences between the humidity threshold value and magnitude of adhesion force. The reasons for such large differences are the difference in tip size and shape as well the morphologies of tested silicon substrate.

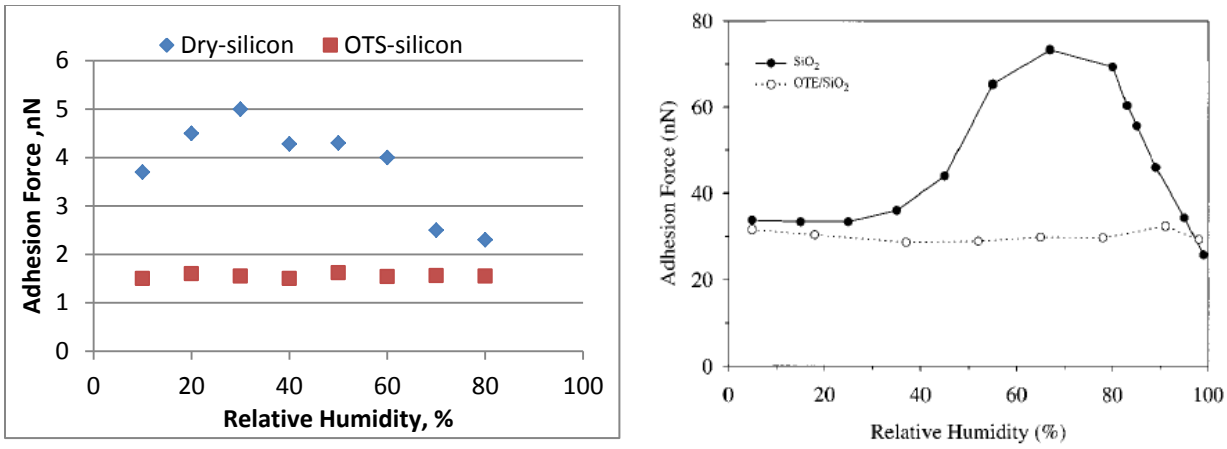

a. **b. Xiao and Qian [91]**

Figure 4.25 Effect of humidity on adhesion between AFM tip and hydrophobic/hydrophilic silicon substrates

4.4.4. 48um Silica Bead Adhesion on Flat Silicon Substrate

Figure 4.26 presents the effect of humidity on adhesion force between 48um silica bead and hydrophobic/hydrophilic plane substrates. It is observed that capillary forces increase with increase in relative humidity. The increase in adhesion in case of hydrophobic surface is relatively lower than that in hydrophilic surface. This is due to the non-wetting properties of hydrophobic surfaces that reduce the probability of vapor condensation especially at low humidity. The difference between AFM tip and silica bead is the diameter. Because of the large diameter of silica bead compared to AFM tip, any more increase in humidity will create larger meniscus. Hence, there is no probability to be the curvature meridional radius r larger than azimuthal one x as shown in Fig.4.27b (i.e. there no way to have pressure repulsive force).

The effect of humidity not just increases the vertical adhesion forces but also the total work of adhesion that is needed to dettached a particle from a surface as shown in Fig.4.28. For a percentage rise in vertical adhesion of 50%. The equivalent increase in work of adhseion is more than 4 folds.

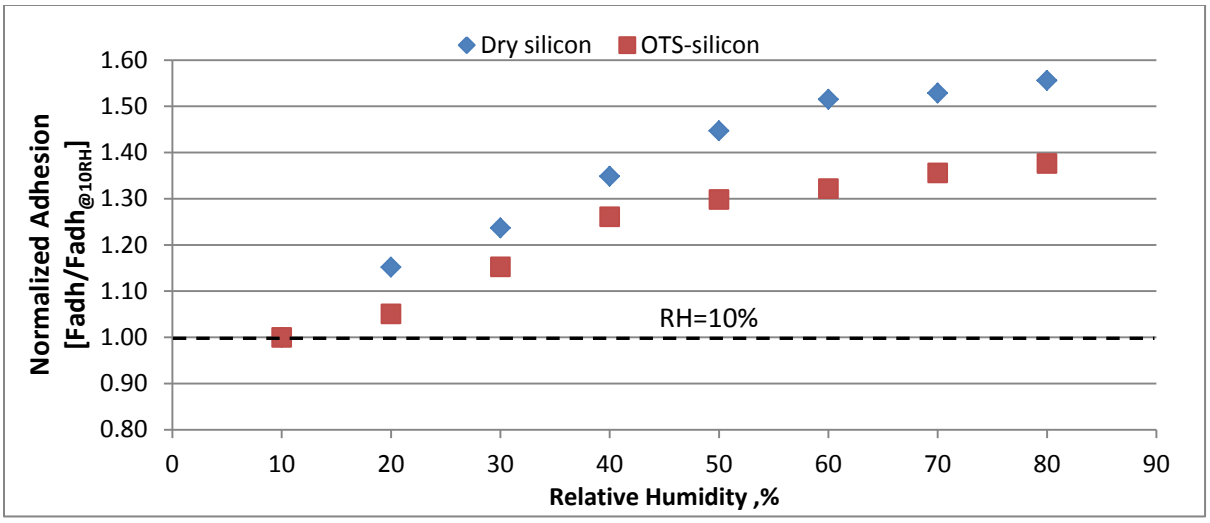

Figure 4.26 Effect of humidity on adhesion between 48um silica bead and hydrophobic/hydrophilic silicon substrates

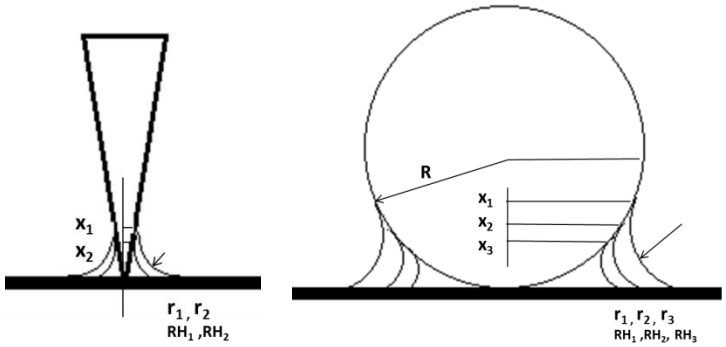

a. **b.**

Figure 4.27 Humidity effect on meniscus curvature

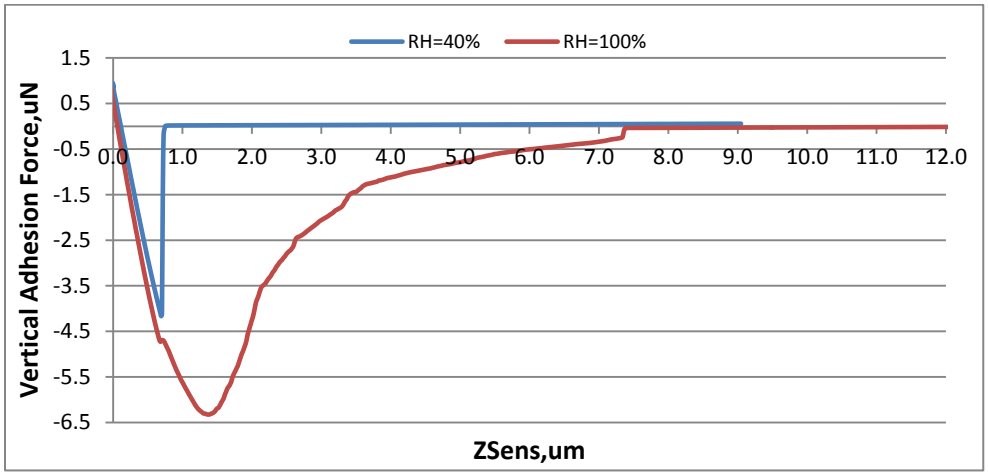

Figure 4.28 Effect of humidity on vertical adhesion curve of 48um silica bead on hydrophilic silicon substrate

4.4.5. Adhesion Forces on Micro-textured Silicon Substrate

Figure 4.29 shows the nature of interaction between 48um silica particle and textured silicon surface. The textured surfaces have uniform 10x10um post size with different post to post distance. The effect of post to post distance on adhesion force magnitude is shown in Fig.4.30. Increasing the space between the posts (i.e. reducing solid fraction, φ) results in smaller real contact area between the particles and surfaces which in turn leads to reduction in adhesion force as indicated by Fig.4.30.

Treating the surface with a low-energy silane (octadecyltricholorosilane –OTS) leads to reduction of interfacial energy as described by JKR and DMT models. The effect of silanization becomes more effective in case of large contact area. Hence, in the case of large post to post distance like 25x25um surface (i.e. low solid fraction), there no much effect for surface silanization on adhesion. Surface silanization, has strong effect on silanized flat silicon substrates as shown in Fig.4.31 ,and small post to post distance textured surface (such as 5x5 um, high solid fraction) as represented in Fig.4.30.

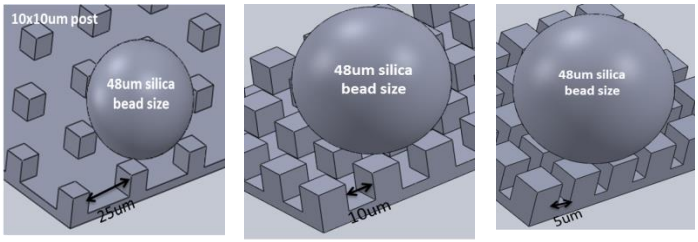

a. 25umx25um **b. 10umx10um** **c. 5umx5um**

Figure 4.29 Effect of surface texturing on area of contact

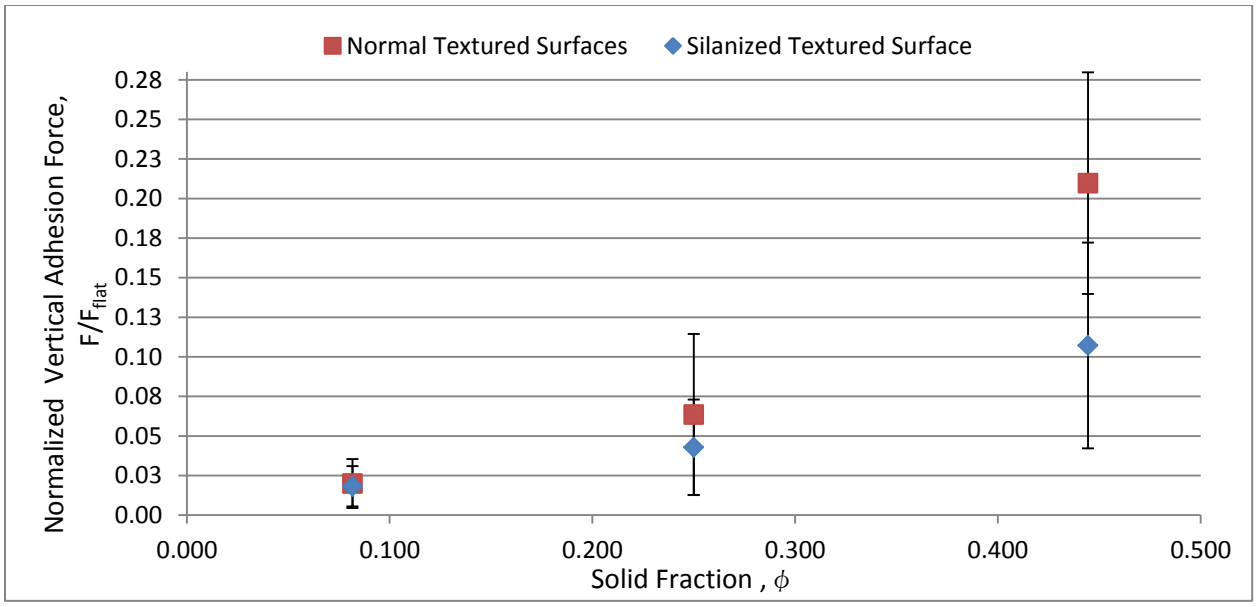

Figure 4.30 Effect of surface texturing and silanizationon on vertical adhesion forces of 48um silica bead

4.4.6. Adhesion Forces on Nano-grass Textured Surface

To achieve more adhesion reduction, the distance between the textures should be smaller than the particle size to avoid particle settlement between the surface patterns. Micro textured surfaces will have no effect on the magnitude of adhesion forces in case of particles size less than its post to post distance. Hence, it is important to design surfaces with nano-morphology. Figure 4.31 shows normalized adhesion forces for different silica bead sizes on nano-grass surface. Creating a nano-grass texture reduces the area of contact between the particles and surface thus resulting in reduction in the magnitude of adhesion forces. It is clear that nano-grass surface prohibit any chance for the particles to settle between the surface textures even the smallest ones with 5 or 10 um beads size. Silanized nano-grass surfaces do not have any effect on the magnitude of adhesion force due to small contact area of interaction.

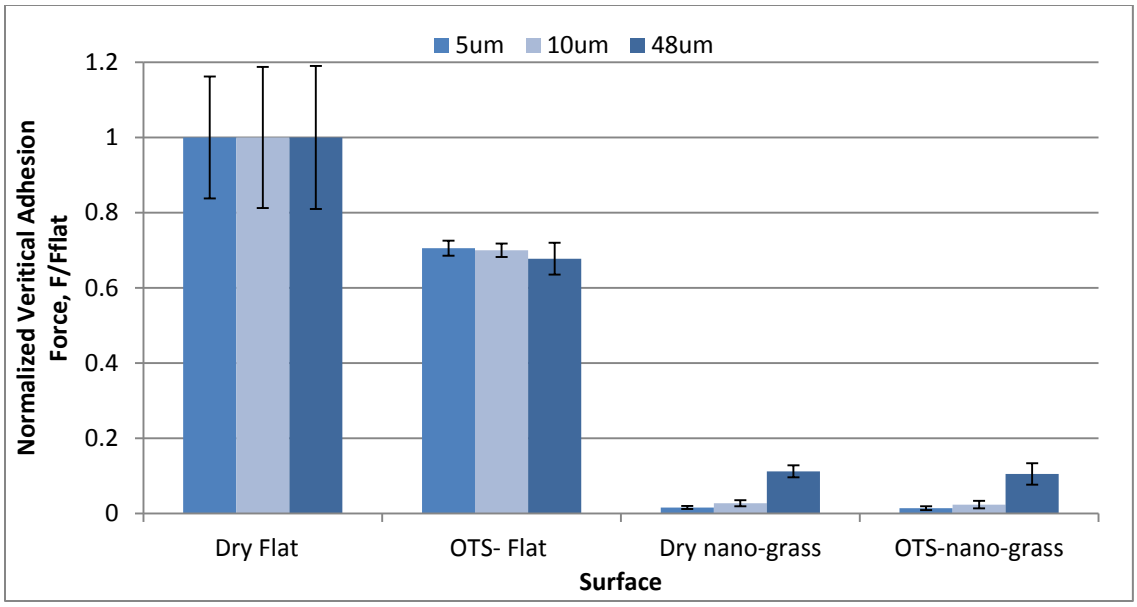

Figure 4.31 Normalized vertical adhesion force between different silica bead size and nano-grass textured surface

4.4.7. Qualitative Friction Analysis on Dry Surfaces

Lateral forces data has been obtained from surface friction images using 48 um silica bead and based on comparing the roughness parameter of each surface. Fiction image normalized roughness values (average roughness, R_a and root mean square roughness, R_q) are plotted in Fig.4.32. It is indicated that silanized surfaces exhibit less friction properties. Creating thin film of silane leads to reduction of the interfacial shear strength between the bead and the surface. On the other hand silanized surfaces have non-wetting properties and can prevent meniscus and capillary formulation **[110-113].** Since, the effect of silanization mainly depends on contact area of particle-surface interaction, it can be seen that there is strong effect of silanization on flat surfaces and weak effect on nano-grass textured surfaces due to their small contact area. However, Figure 4.32 shows that the friction between a 48um bead and micro texture is more than the friction on a flat substrate. This is due to the effect of edge collision **[114]** on the magnitude of friction which exceeded the reduction in the magnitude of friction due to reduction in contact area. The 25x25 um texture surface showed large twisting the cantilever (i.e. high

friction) while bead is moving along surface as shown by Fig.4.33a. The 10x10 um texture has less friction compared to the 5x5um texture, due to the fact that the 10x10 um texture has less contact area compared to the 5x5um texture , even though the 10x10 um texture has more collision edge effect. This indicates that the effect of large contact area in 5x5um texture is stronger than the effect of edge collision in the 10x10 um texture. Nano-grass surface has low friction properties; since it doesn't have collision effect due to the short spaces between the textures. In addition, the contact area between the bead and the nano-grass surface is considered to be very small.

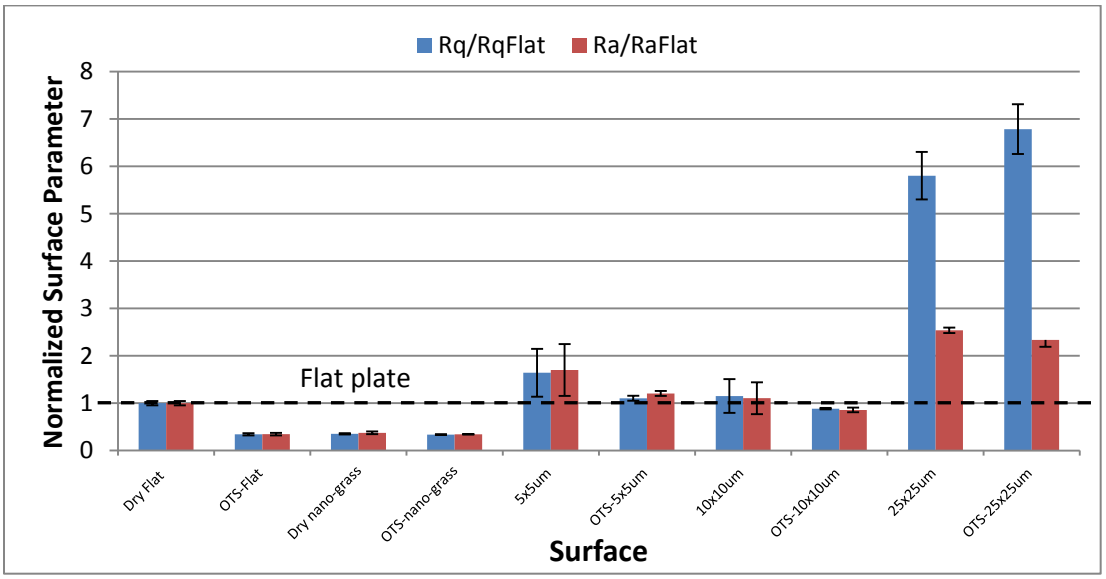

Figure 4.32 Normalized friction image parameters of nano and micro-textured surfaces

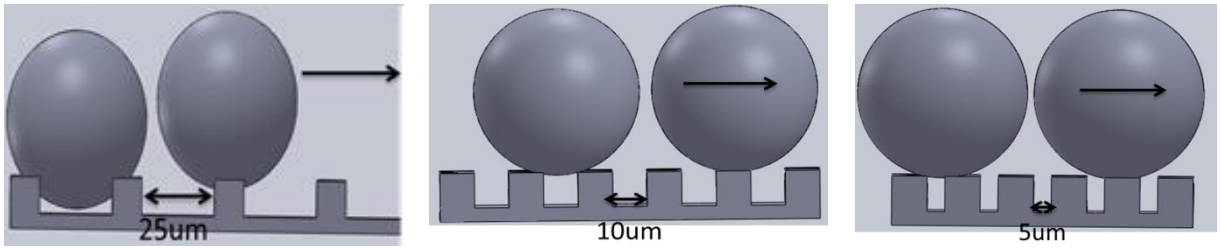

a. 25umx25um b. 10umx10um c. 5umx5um

Figure 4.33 Area of contact and edges collision effect of texture edges

4.4.8. Adhesion on Thin Film of Oil

The force between solid particle and liquid surface is fundamentally different than between solid-solid interaction. The dominant force here is the capillary force .The formulated capillary bridge is resulted from the effects of capillary pressure and surface tension forces. The particle keep under force effect even after retracted from the solid surface beneath the liquid film. The following describe particle-oil film interaction. In the beginning, the particle is far from the surface so there is no deflection effect on AFM cantilever. As the particle starts approaching towards the surface, some type of oil deformation occurs due to Van der Waal forces, surface tension and gravity between the particle and oil film **[42, 99, 100, 115]**. This interaction affect jump to contact point, measurement of film thickness and lead to distort force curve **[116]** as shown in Fig.4.34b (point 2, red line). Once the particle touched the surface, a zero deflection of cantilever is obtained, and the distance between 2(the point of film contact) and 3 represent approximately the film thickness **[96]** as shown in Fig.4.34b. Then, the cantilever deflect reversely till reaches threshold point which is determined based on cantilever sensitivity and spring constant to guarantee that the bead touched the substrate. Now the process is reversed to detach the probe from the surface, so the cantilever is pulled up and due to meniscus formulation around the bead which result from the surface tension forces and Laplace pressure **[96]**, cantilever start to deflect. Point 5(Fig.4.34b) represent the maximum deflection which also determines the maximum vertical adhesion force. Cantilever still under necking effect, but the forces become less; due to a decrease in the wetting area and increase in the radius of meniscus curvature. The neck becomes thinner and this means less surface tension force. In the meantime the effect of Laplace pressure becomes downward; since the radius of curvature becomes larger

than the radius of wetting area. The cantilever continues moving up. At the same time the neck of oil becomes even thinner till it breaks and the cantilever becomes free again.

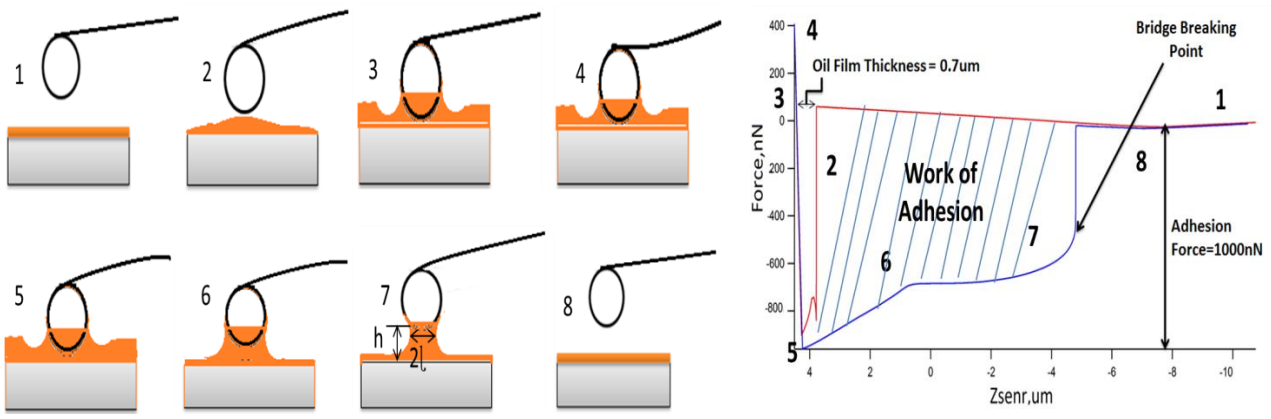

a. b.

Figure 4.34 Adhesion force behavior between particle and thin film of oil

Because of necking effect, the cantilever continued under meniscus force effect and it needs large distance to completely retract as represented in Fig.4.35. Hence, it is worth to look not just at the maximum adhesion force (i.e. maximum deflection), but also at the work of adhesion (i.e. area above the curve Fig.4.34b). The work of adhesion includes all adhesion forces that affect the cantilever while it is moving up. Work of adhesion depends on oil film thickness, bead size, surface morphology, and oil properties such as viscosity and surface tension.

$$W_I = \int_0^{h_i} F_I\,(z)dz \qquad (4.5)$$

Where $F_I(z)$ is the adhesion force , which varies with the vertical location of the cantilever, h_i is stand-off height , which is the distance between the free surface of impregnated liquid and cantilever probe.

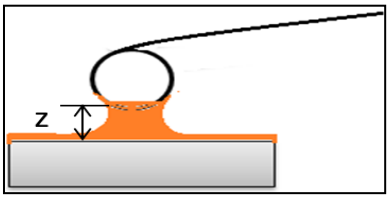

Figure 4.35 Lubricant bridge between the particle and oil surface

4.4.9. Adhesion Forces and Work of Adhesion on LIS

Figure 4.36 shows a plot of vertical adhesion forces curves for different textured surfaces using a 48um silica bead. The plot indicates that oil wicking leads to stabilize the oil inside the surface textures, and this in turn reduces the interaction between colloid and liquid film.

Also , it can be observed that there are two type of curves, the concave down curve (i.e. large slope) for Nano-grass which indicates quick capillary neck breakage, and the concave up curves (i.e. small slope) for micro-textured. The concave up curve curves in the case of micro-textured surface is due to slower movement of cantilever compared to nano-textured. This slower movement is due to the fact that the cantilever needs to across a large distance because of the larger amount of oil in micro-textured surface.

Vertical adhesion decreases by cantilever moving up, due to reduction of surface tension force as a decrease of wetting area. On the other side, pressure force becomes even less due to increase in the radius of curvature and at some point of cantilever movement, the pressure force effect becomes downward.

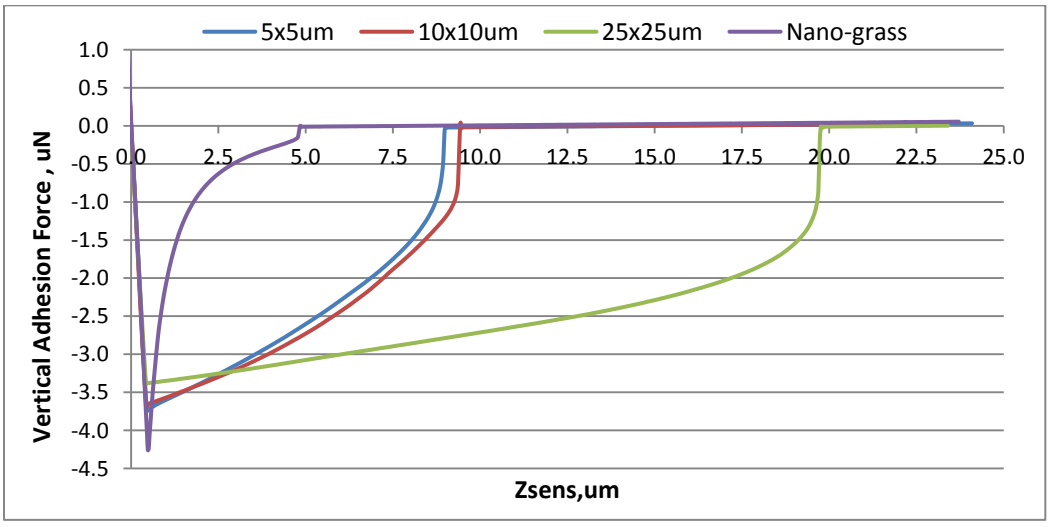

Figure 4.36 Vertical adhesion force curves for different micro/nano-textured surface using 48um silica beads

Figures (4.38&4.39) shows the plot of normalized work of adhesion and vertical adhesion force for different micro-textured surface using 48um silica beads. The plot indicates that vertical adhesion on LIS is less than that one on smooth flat silicon substrate due to the following reasons. Texturizing the surface leads to reduction in the area of interaction between the bead and the surface and hence reduction in adhesion forces. The effecrive surface energy of silica bead and silicon oil is smaller than in case of dry interaction of silica bead-silicon substrate.

Vertical adhesion on LIS decreases with increase the space between the texture posts due to the following. The bead is under the effect of three forces. So the required force to pull up the bead is:

$$F_{pulling} = F_{\sigma} + W_{bead} - F_h sin\theta \tag{4.6}$$

Where F_{σ} is the capillary force resulted from the meniscus , W is the weight of bead , F_h is hydrostatic force as represneted in Fig.4.37a&b. The difference between the tested textures is the amount of displaced oil from the texture. The displaced oil accumulates around the bead and generates hydrostatic forces which help to puch the bead upward as shown in Fig.4.39. Hydrostatic force is given by:

$$F_h = \bar{P}.A \tag{4.7}$$

Where $\bar{P} = \gamma.h$ is the hydrostatic pressure at centroidal point , γ is specific wieght of fluid , h is the height of fluid behind the bead , and A is area wetted by the fluid.

Hydrostatic force depends on the displaced volume from the texture. The volume of formulated oil meniscus equal half of volume of sequeezed oil from the texture. Hydrostatic forces increase with increase meniscus volume (i.e. height). The amount of displaced oil

increases with increase in the space between texture posts. And as a result, more hydrostatic is suggested in low solid fraction surfaces (i.e. large post to post space)

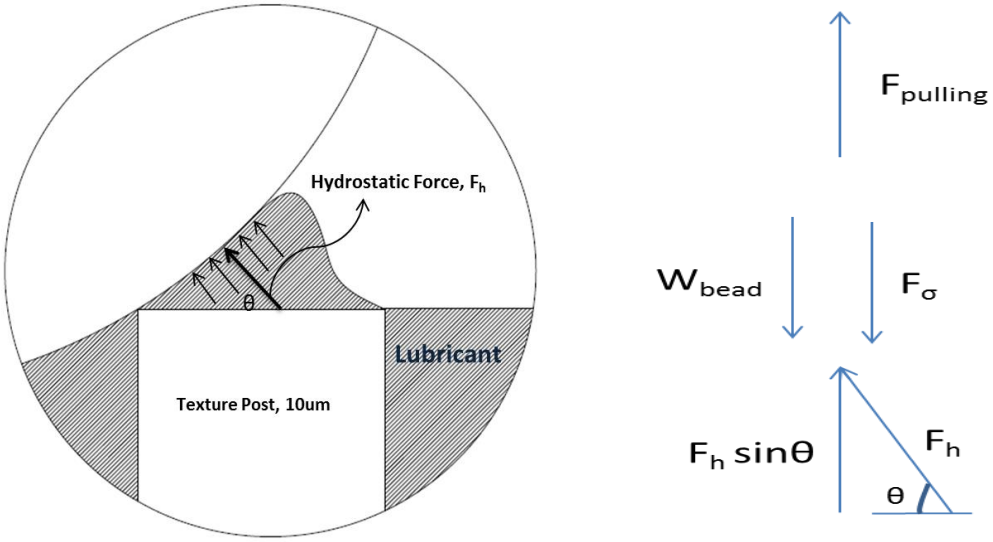

a. **b.**

Figure 4.37 Hydrostatic forces on the bead surface

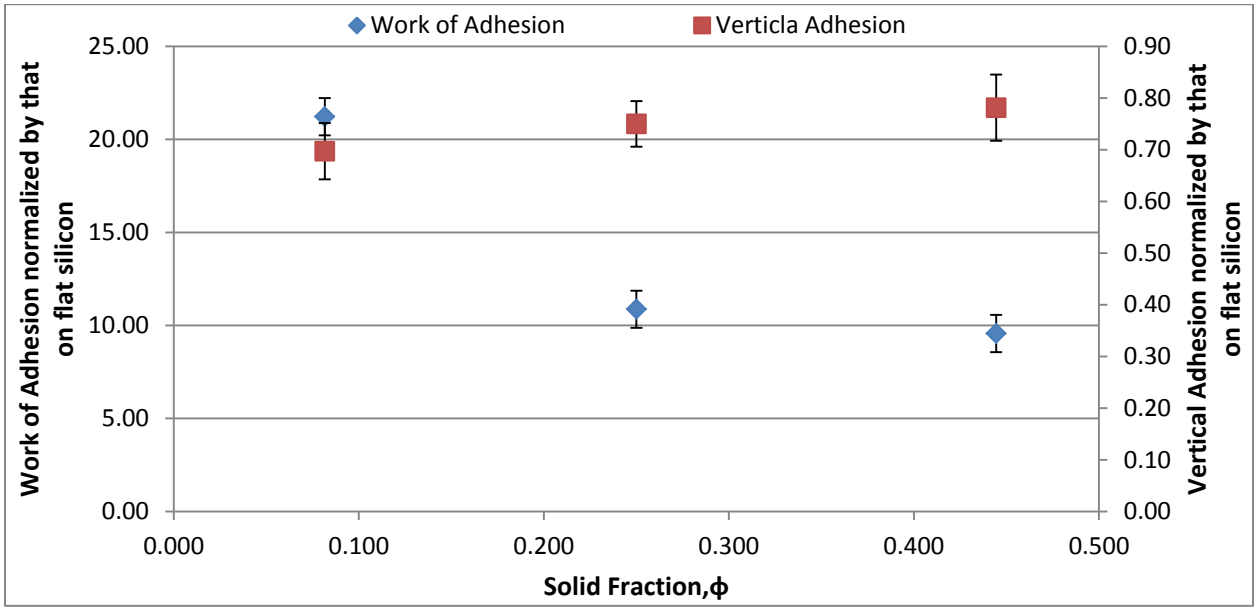

Figure 4.38 Normalized vertical adhesion force and work of adhesion on oil impregnated surfaces by that on flat smooth silicon substrate using 48um silica bead

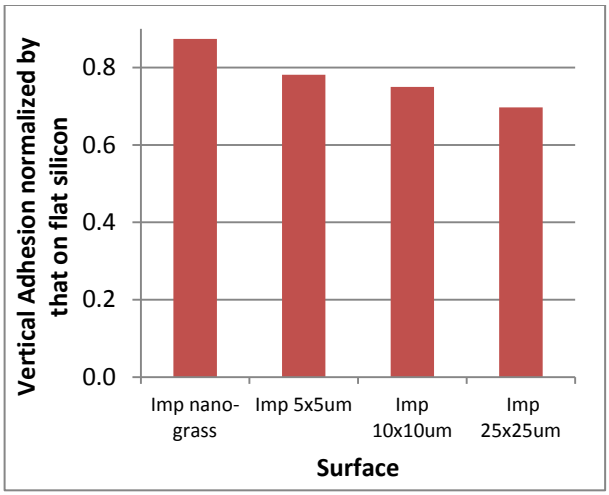

a.

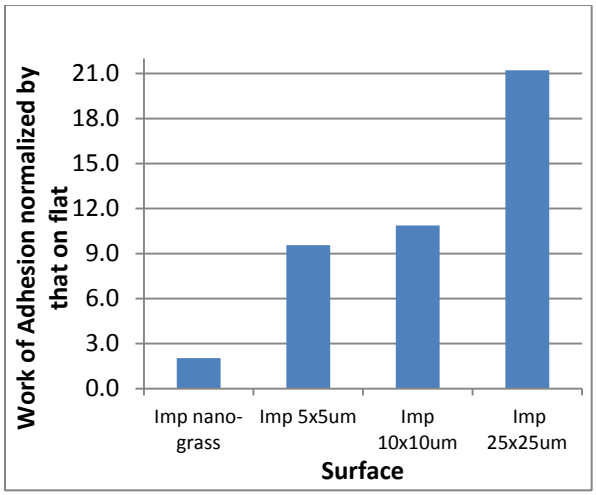

b.

Figure 4.39 Normalized vertical adhesion force and work of adhesion on oil impregnated surfaces by that on flat smooth silicon substrate using 48um silica bead

Figure 4.40 shows the relation between work of adhesion/vertical adhesion forces and silica particle size. The plot indicates that there is a linear relation between vertical adhesion force and bead size. The particle size determines the behavior of force; since gravity effect, surface tension force, and the amount of oil displaced from the textures mainly depend on particle size.

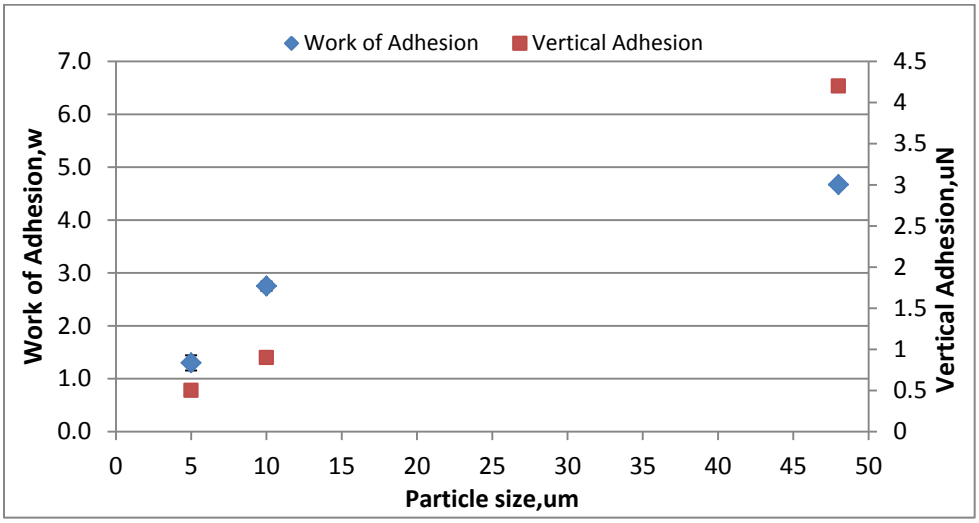

Figure 4.40 Vertical adhesion and work of adhesion on impregnated nano-grass textured surface using different silica bead size

4.4.10. Qualitative Friction Analysis on LIS

Figure 4.42 shows qualitative friction study on nano/micro-textures lubricant impregnated surfaces. The friction measurements have been carried out using 48um silica bead. The impregnated lubricant is silicon oil with 10 cs viscosity. Silicon oil has positive spreading coefficient and this means that oil will completely wet the surface. During sample oil impregnation process, the samples were withdrawn at a rate V such that the capillary number, Ca = $\mu V/\gamma$, corresponding to an impregnating lubricant with viscosity μ and surface tension γ, was less than 10^{-5}. This ensured that no much excess lubricant remain on the post tops. ESEM image of the impregnated texture shows the silicone oil trapped in the texture between the posts and suggests that the film that wets the post tops is thin as shown in Fig.4.41.

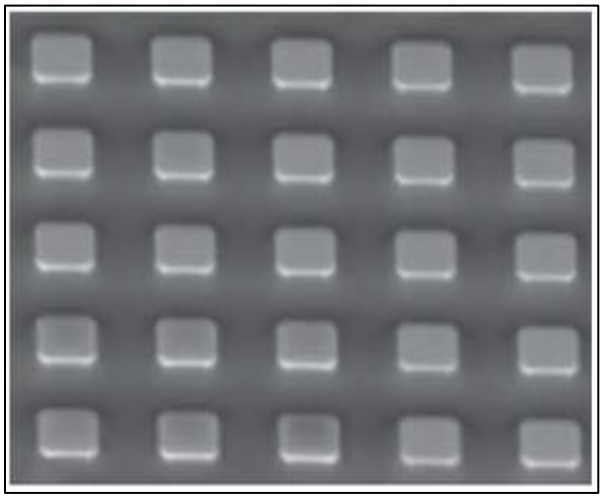

Figure 4.41 ESEM image for 10x10um oil impregnated surface

Friction is a dissipative process. During relative motion, energy is required to overcome interfacial adhesion **[117]** and collision effect of surface asperities **[114]**. The interfacial adhesion depends on the physical and chemical of the contacts surfaces. In case of dry contact the magnitude of friction required to overcome the adhesion force is presented in the following equation **[117]**:

$$F_a = A_r \tau_a \tag{4.8}$$

In case of composite surfaces (i.e. have two phases, solid and liquid) such as lubricant impregnated surfaces the magnitude of friction forces result from the adhesion is dependent on fraction areas of solid and liquid phases **[117]** given by:

$$F_a = A_r[\alpha\tau_a + (1-\alpha)\tau_l] \tag{4.9}$$

Where, τ_a and τ_l are average shear strengths of the dry contact and of the liquid film, respectively; α is the fraction of un-lubricated area.

The coefficient of friction for oil is less than that for solid surface. Hence, oil impregnation causes a drastic reduction in surface friction. Based on eq.4.9 increasing the fraction area of lubricant should lead to more friction reduction. Figure 4.42 shows that increasing the post to post space (i.e. increase lubricant fraction area) lead to more surface friction especially in case of 25x25um texture. The reason for that include: Increasing the spaces between the posts means more amount of oil is impregnated inside the texture. An amount of oil will be pushed out of the texture when particle lands on the surface as explained in section 4.4.9. The squeezed oil formulates a meniscus between the particle and the surface which leads to enhancing the friction force **[112, 117]**. The magnitude of meniscus contribution in friction relies on the size of formulated meniscus which depends on the amount of squeezed oil form the textures. In case of 25x25um texture large meniscus is formulated due the large amount of squeezed oil compared to the other textures as shown in Fig.4.43.

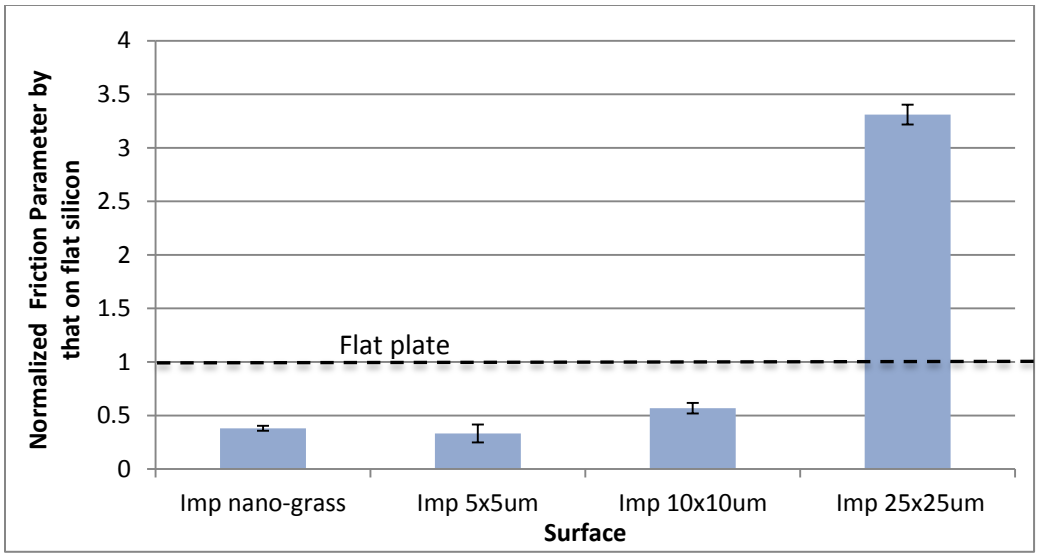

Figure 4.42 Normalized Friction image parameter by that on flat smooth silicon substrate

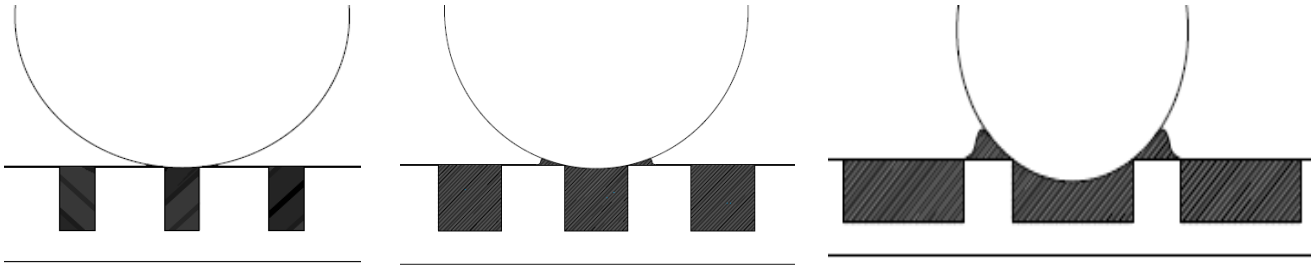

a. 5x5um **b. 10x10um** **c. 25x25um**

Figure 4.43 The size of formulated meniscus

4.4.11. Humidity Effect on Adhesion on Wet and Dry Textured Surfaces

Figure 4.44 shows the effect of vapor condensation at high humidity level on vertical adhesion force between 48um silica bead and different flat/nano/micro-textured hydrophilic/hydrophobic surfaces.

As mentioned above , increasing humidity causes a drastic increase in vertical adhesion between 48um silica bead and flat hydrophilic and hdrophobic surfaces. 50% increase in adhesion has been observed on hyrophilic flat surface due to vapor condensation at 100% RH. Adhesion on hydrophibic flat surfaces at 100% RH is less than that on hyrophilic surfaces. This

is due to the effect of surface silanization which in turn relatively hinder the meniscus formulation.

In case of nano and micro-textured surfaces , it is shown that the meniscus forces are the dominant ones at high humidity. An increase of 2-5 folds in vertical adhesion is observed on both nano/micro hydrophibic /hydrophilic surfaces.

Anand et. al. [64] reported that at high humidity water droplets can condense within the textures of hydrophobic surfaces , impale the vapor pockets and strongly pin to the surfaces as shown in Fig.4.45. The condensate water film promotes water bridge formulation between the particle and the surface. The poor mobility of water droplet (i.e.wenzel droplet) and the coalescence between the droplets suggest more adhesion force.

Anand et. al.[64] also reported that for lubricant impregnated surfaces ,the condensed droplet remain a float on lubricant film without implaing into the surface textures, in addition to that the water droplet keep moving and sliding on lubricant film as shown in Fig.4.46. Hence, there is no effect for the humidity and vapor condensation on vertical adhesion forces and no water brigde between the particle and surface.

However , the size of condensded water vapor or its exact location with respect to the silica bead during adhesion test are not well defined. So, a distortion in force curves and disparity in adhesion mangitude have been observed. This is due to the nature of formulated meniscus between the bead and condensed water on the surface as shown in Fig.4.47a&b.

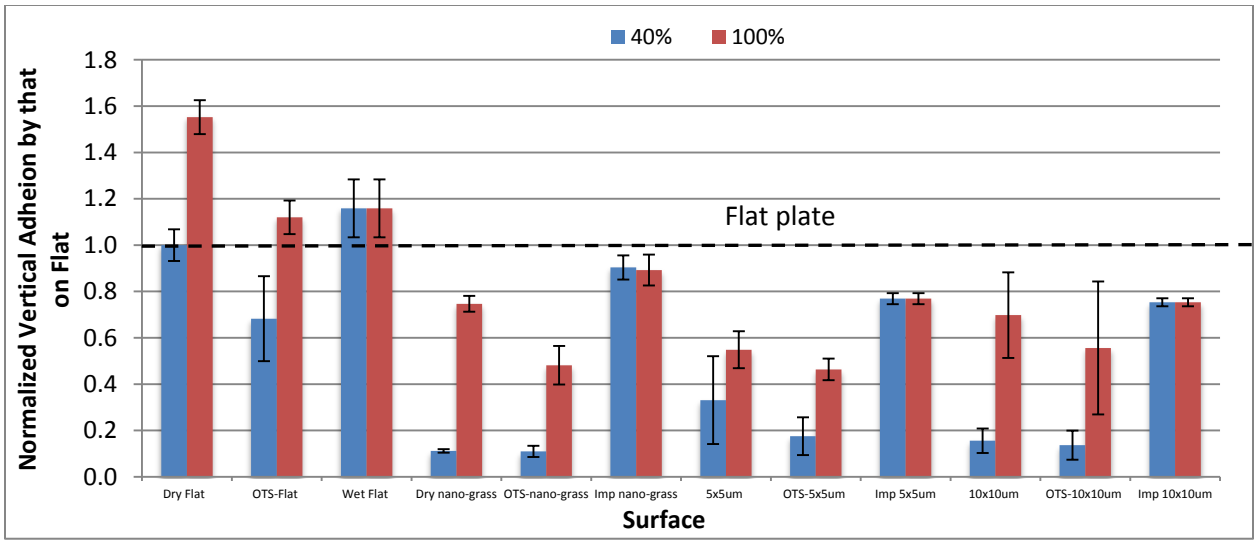

Figure 4.44 Normalized vertical adhesion force by that on flat smooth silicon substrate at two level of humidity

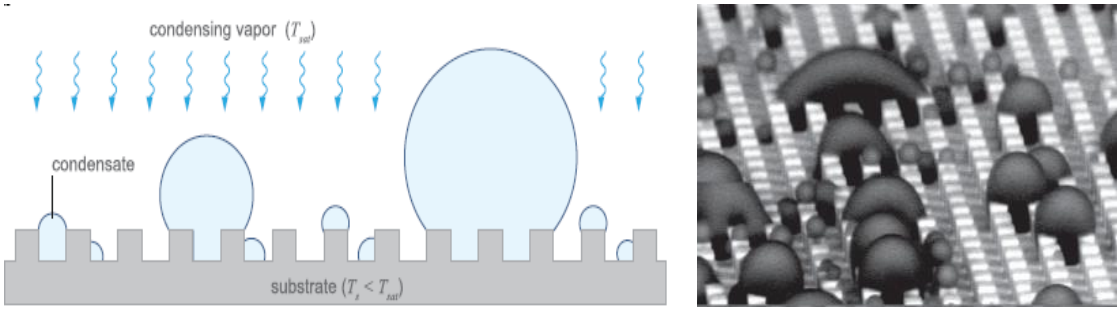

a. **b.**

Figure 4.45 Condensation of water vapor on dry hydrophobic surfaces[64]

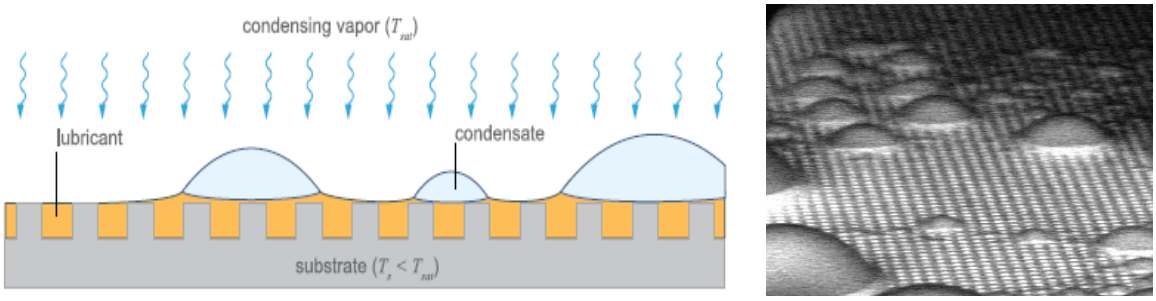

a. **b.**

Figure 4.46 Condensation of water vapor on lubricant impregnated surfaces[64]

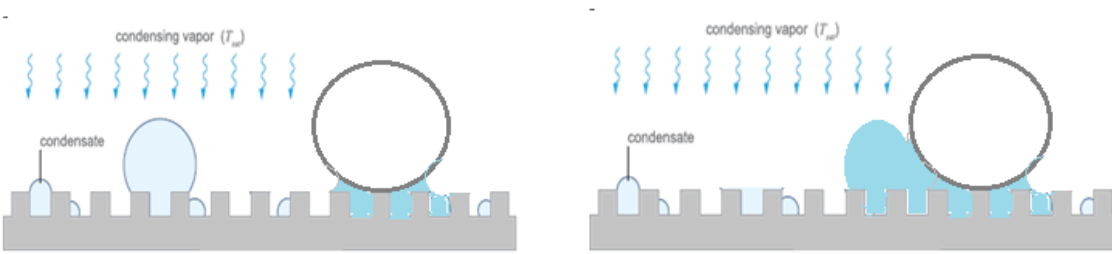

a. **b.**

Figure 4.47 The size of condensed water vapor and its location

CHAPTER 5

CONCLUSIONS

The effect of dust on PV module performance and potenial mitigation techiques have been studied. Based on the study results; the following can be concluded:

1. Around 15% reduction in the PV module power output due to dust fouling after a duration of 5 weeks of outdoor exposure without cleaning.
2. More than 30% reduction in the spectral transmisivity of plane PV module glass cover.
3. Anti-reflective coating enhances the optical properties of PV module glass cover and hence PV module performance
4. Dust particles have irregular and various forms but in general tend to be spherical in shape.
5. Oxygen has the highest concentration followed by calcium, and silicon elements. Calcite and quartz compounds occupied more than 50% of the dust particles content.
6. Most of particles have a diameter less 2μm with presence of few large particles (≥10μm).
7. Adhesion and friction forces of silica particles on flat surfaces do increase with increase in particle size.
8. Texturing the surface with rough peak to peak distance less than the particles size lead to drastic reduction in adhesion forces but not necessary friction forces.
9. Silica particle adhesion strength on lubricant impregnated textured silicon surfaces is lower than those on dry flat silicon surfaces.

10. The vertical particle-adhesion force strength on LIS is dependent on texture and decreases with increasing the spaces between texture posts.
11. Decrease the spaces between texture posts causes an increase in work of adhesion of silica particle on LIS.
12. Silica particle vertical adhesion strength on lubricant impregnated textured silicon surfaces is larger than those on dry textured surfaces.
13. Lubricant impregnated surfaces showed lower friction properties compared to dry flat/textured surfaces.
14. At high humidity level dry hydrophobic surfaces showed a drastic increase in the vertical adhesion.
15. The adhesion properties of LIS doesn't affect with humidity or vapor condensation.

Recommedations:

The effect of dust fouling on the performance of PV systems is an important problem and at the same time is very complex. The current study sheds some light on some aspects of such a problem and by no means it is complete. Hence, further studies beside which is being reported in the literature need to be conducted ;in order to fullly understand the nature of such problem and find practical solution for it. A number of aspect need to be further studied include:

1. The economic effect of dust fouling and the feasibility of employing the mitigation methods.
2. Effect of humidity on friction forces.
3. Effect of oil viscosity and spreading coefficient on adhesion mechanism.
4. Reducing the effect of meniscus forces (i.e. reduce surface tension).

5. Studying the adhesion of small particles (<5um).
6. Utilization of the nano-particles for manipulating the lubricant properties such as refractive index, surface tension and conductivity.
7. Application of electrostatic or magnatic field on LIS.

REFERENCES

[1] Alnaser, W. and N. Alnaser, *The status of renewable energy in the GCC countries.* Renewable and Sustainable Energy Reviews, 2011. **15**(6): p. 3074-3098.

[2] Adinoyi, M.J. and S.A. Said, *Effect of dust accumulation on the power outputs of solar photovoltaic modules.* Renewable Energy, 2013. **60**: p. 633-636.

[3] Kaldellis, J. and A. Kokala, *Quantifying the decrease of the photovoltaic panels' energy yield due to phenomena of natural air pollution disposal.* Energy, 2010. **35**(12): p. 4862-4869.

[4] Onyegegbu, S., *Performance of photovoltaic cells in an equatorial climate.* Solar & wind technology, 1989. **6**(3): p. 275-281.

[5] Tian, W., et al., *Effect of urban climate on building integrated photovoltaics performance.* Energy conversion and management, 2007. **48**(1): p. 1-8.

[6] Gonzalez, M. and J. Carrol, *Solar Cells Efficiency variations with varying atmospheric conditions.* Solar Energy, 1994. **53**(5): p. 395-402.

[7] Mekhilef, S., R. Saidur, and M. Kamalisarvestani, *Effect of dust, humidity and air velocity on efficiency of photovoltaic cells.* Renewable and Sustainable Energy Reviews, 2012. **16**(5): p. 2920-2925.

[8] Mani, M. and R. Pillai, *Impact of dust on solar photovoltaic (PV) performance: Research status, challenges and recommendations.* Renewable and Sustainable Energy Reviews, 2010. **14**(9): p. 3124-3131.

[9] Goossens, D., Z. Offer, and A. Zangvil, *Wind tunnel experiments and field investigations of eolian dust deposition on photovoltaic solar collectors.* Solar Energy, 1993. **50**(1): p. 75-84.

[10] Goossens, D. and E. Van Kerschaever, *Aeolian dust deposition on photovoltaic solar cells: the effects of wind velocity and airborne dust concentration on cell performance.* Solar Energy, 1999. **66**(4): p. 277-289.

[11] Meyer, E.L. and E.E. van Dyk, *Assessing the reliability and degradation of photovoltaic module performance parameters.* Reliability, IEEE Transactions on, 2004. **53**(1): p. 83-92.

[12] Ettah, E., et al., *The Effect of Relative Humidity on the Efficiency of Solar Panels in Calabar, Nigeria.* Universal Journal of Management and Social Sciences, 2012. **2**(3): p. 8-11.

[13] Omubo-Pepple, V., C. Israel-Cookey, and G. Alaminokuma, *Effects of temperature, solar flux and relative humidity on the efficient conversion of solar energy to electricity.* European Journal of Scientific Research, 2009. **35**(2): p. 173-180.

[14] Touati, F., et al., *Effects of Environmental and Climatic Conditions on PV Efficiency in Qatar.*

[15] Katkar, A., N. Shinde, and P. Patil, *Performance & Evaluation of Industrial Solar Cell wrt Temperature and Humidity.* International Journal of Research in Mechanical Engineering and Technology, 2011. **1**(1): p. 69-73.

[16] Gwandu, B. and D. Creasey, *Humidity: a factor in the appropriate positioning of a photovoltaic power station.* Renewable Energy, 1995. **6**(3): p. 313-316.

[17] Tan, C.M., B.K.E. Chen, and K.P. Toh, *Humidity study of a-Si PV cell.* Microelectronics Reliability, 2010. **50**(9): p. 1871-1874.

[18] Jiang, H., L. Lu, and K. Sun, *Experimental investigation of the impact of airborne dust deposition on the performance of solar photovoltaic (PV) modules.* Atmospheric Environment, 2011. **45**(25): p. 4299-4304.

[19] Rabii, A., M. Jraidi, and A. Bouazzi. *Investigation of the degradation in field-aged photovoltaic modules*. 2003: IEEE.

[20] Kempe, M.D., *Modeling of rates of moisture ingress into photovoltaic modules.* Solar Energy Materials and Solar Cells, 2006. **90**(16): p. 2720-2738.

[21] Zhang, X., et al., *Superhydrophobic surfaces: from structural control to functional application.* Journal of Materials Chemistry, 2008. **18**(6): p. 621-633.

[22] Boinovich, L.B. and A.M. Emelyanenko, *Hydrophobic materials and coatings: principles of design, properties and applications.* Russian Chemical Reviews, 2008. **77**(7): p. 583.

[23] Pang, H., J. Close, and K. Lam. *Study on Effect of Urban Pollution to Performance of Commercial Copper Indium Diselenide Modules*. 2006: IEEE.

[24] Asl-Soleimani, E., S. Farhangi, and M. Zabihi, *The effect of tilt angle, air pollution on performance of photovoltaic systems in Tehran.* Renewable energy, 2001. **24**(3): p. 459-468.

[25] Said, S., *Effects of dust accumulation on performances of thermal and photovoltaic flat-plate collectors.* Applied Energy, 1990. **37**(1): p. 73-84.

[26] Ibrahim, A., *Effect of shadow and dust on the performance of silicon solar cell.* J. Basic. Appl. Sci. Res, 2011. **1**(3): p. 222-230.

[27] Mohandes, B.M.A., L. El-Chaar, and L. Lamont, *Application study of 500 W photovoltaic (PV) system in the UAE.* Applied Solar Energy, 2009. **45**(4): p. 242-247.

[28] Boykiw, E., *The Effect of Settling Dust in the Arava Valley on the Performance of Solar Photovoltaic Panels.* 2011.

[29] Elminir, H.K., et al., *Effect of dust on the transparent cover of solar collectors.* Energy conversion and management, 2006. **47**(18): p. 3192-3203.

[30] Hegazy, A.A., *Effect of dust accumulation on solar transmittance through glass covers of plate-type collectors.* Renewable energy, 2001. **22**(4): p. 525-540.

[31] Qasem, H., et al., *Dust effect on PV modules.* 2011.

[32] El-Shobokshy, M.S. and F.M. Hussein, *Degradation of photovoltaic cell performance due to dust deposition on to its surface.* Renewable energy, 1993. **3**(6): p. 585-590.

[33] Kaldellis, J., P. Fragos, and M. Kapsali, *Systematic experimental study of the pollution deposition impact on the energy yield of photovoltaic installations.* Renewable Energy, 2011. **36**(10): p. 2717-2724.

[34] El-Shobokshy, M., A. Mujahid, and A. Zakzouk, *Effects of dust on the performance of concentrator photovoltaic cells.* IEE Proceedings I (Solid-State and Electron Devices), 1985. **132**(1): p. 5-8.

[35] Kumar, E.S., B. Sarkar, and D. Behera, *Soiling and Dust Impact on the Efficiency and the Maximum Power Point in the Photovoltaic Modules.* International Journal of Engineering, 2013. **2**(2).

[36] Zorrilla-Casanova, J., et al., *Analysis of dust losses in photovoltaic modules.*

[37] Hee, J.Y., et al., *The Effect of Dust on Transmission and Self-cleaning Property of Solar Panels.* Energy Procedia, 2012. **15**: p. 421-427.

[38] Garg, H., *Effect of dirt on transparent covers in flat-plate solar energy collectors.* Solar Energy, 1974. **15**(4): p. 299-302.

[39] Nahar, N. and J.P. Gupta, *Effect of dust on transmittance of glazing materials for solar collectors under arid zone conditions of India.* Solar & wind technology, 1990. **7**(2): p. 237-243.

[40] El-Shobokshy, M.S. and F.M. Hussein, *Effect of dust with different physical properties on the performance of photovoltaic cells.* Solar Energy, 1993. **51**(6): p. 505-511.

[41] Verma, L.K., et al., *Self-cleaning and antireflective packaging glass for solar modules.* Renewable Energy, 2011. **36**(9): p. 2489-2493.

[42] Jing, L., et al., *A thin liquid film and its effects in an atomic force microscopy measurement.* Chinese Physics Letters, 2009. **26**(8): p. 086802.

[43] De Gennes, P.-G., F. Brochard-Wyart, and D. Quéré, *Capillarity and wetting phenomena: drops, bubbles, pearls, waves*. 2004: Springer.

[44] Kappl, M., *Surface and interfacial forces*. 2009: John Wiley & Sons.

[45] Wenzel, R.N., *Resistance of solid surfaces to wetting by water.* Industrial & Engineering Chemistry, 1936. **28**(8): p. 988-994.

[46] Wenzel, R.N., *Surface Roughness and Contact Angle.* The Journal of Physical Chemistry, 1949. **53**(9): p. 1466-1467.

[47] Cassie, A. and S. Baxter, *Wettability of porous surfaces.* Transactions of the Faraday Society, 1944. **40**: p. 546-551.

[48] Lafuma, A. and D. Quéré, *Superhydrophobic states.* Nature materials, 2003. **2**(7): p. 457-460.

[49] Cao, L., *Superhydrophobic Surface: Design, Fabrication, and Applications*. 2011, University of Pittsburgh.

[50] Wong, T.-S., et al., *Bioinspired self-repairing slippery surfaces with pressure-stable omniphobicity*. Nature, 2011. **477**(7365): p. 443-447.

[51] Smyth, K., et al. *Dynamic wetting on superhydrophobic surfaces: Droplet impact and wetting hysteresis*. in *Thermal and Thermomechanical Phenomena in Electronic Systems (ITherm), 2010 12th IEEE Intersociety Conference on*. 2010: IEEE.

[52] Quéré, D., *Non-sticking drops.* Reports on Progress in Physics, 2005. **68**(11): p. 2495.

[53] Dorrer, C. and J. Rühe, *Some thoughts on superhydrophobic wetting.* Soft Matter, 2009. **5**(1): p. 51-61.

[54] Miwa, M., et al., *Effects of the surface roughness on sliding angles of water droplets on superhydrophobic surfaces.* Langmuir, 2000. **16**(13): p. 5754-5760.

[55] Dhiman, R., et al., *Droplet mobility on lubricant-impregnated surfaces.* 2012.

[56] Lafuma, A. and D. Quéré, *Slippery pre-suffused surfaces.* EPL (Europhysics Letters), 2011. **96**(5): p. 56001.

[57] Yan, Y., N. Gao, and W. Barthlott, *Mimicking natural superhydrophobic surfaces and grasping the wetting process: A review on recent progress in preparing superhydrophobic surfaces.* Advances in colloid and interface science, 2011. **169**(2): p. 80-105.

[58] Park, Y.B., et al., *Self-cleaning effect of highly water-repellent microshell structures for solar cell applications.* J. Mater. Chem., 2010. **21**(3): p. 633-636.

[59] Verma, L., et al., *Self-cleaning and antireflective packaging glass for solar modules.* Renewable Energy, 2011. **36**(9): p. 2489-2493.

[60] Smith, J.D., et al., *Droplet mobility on lubricant-impregnated surfaces.* Soft Matter, 2013. **9**(6): p. 1772-1780.

[61] Liu, H., et al., *Organogel-based Thin Films for Self-Cleaning on Various Surfaces.* Advanced Materials, 2013.

[62] Kim, P., et al., *Liquid-infused nanostructured surfaces with extreme anti-ice and anti-frost performance.* ACS nano, 2012. **6**(8): p. 6569-6577.

[63] Rykaczewski, K., et al., *Mechanism of Frost Formation on Lubricant-Impregnated Surfaces.* Langmuir, 2013. **29**(17): p. 5230-5238.

[64] Anand, S., et al., *Enhanced condensation on lubricant-impregnated nanotextured surfaces.* ACS nano, 2012. **6**(11): p. 10122-10129.

[65] Xiao, R., et al., *Immersion Condensation on Oil-Infused Heterogeneous Surfaces for Enhanced Heat Transfer.* Scientific reports, 2013. **3**.

[66] Johnson, K., K. Kendall, and A. Roberts, *Surface energy and the contact of elastic solids.* Proceedings of the Royal Society of London. A. Mathematical and Physical Sciences, 1971. **324**(1558): p. 301-313.

[67] Derjaguin, B., V. Muller, and Y.P. Toporov, *Effect of contact deformations on the adhesion of particles.* Journal of colloid and interface science, 1975. **53**(2): p. 314-326.

[68] Hecht, L., *Particle Adhesion to Solid Surfaces.* Journal of the IES, 1990. **33**(2): p. 33-37.

[69] Ramakrishna, S.N., et al., *Controlling adhesion force by means of nanoscale surface roughness.* Langmuir, 2011. **27**(16): p. 9972-9978.

[70] Drelich, J., G.W. Tormoen, and E.R. Beach, *Determination of solid surface tension from particle–substrate pull-off forces measured with the atomic force microscope.* Journal of Colloid and Interface Science, 2004. **280**(2): p. 484-497.

[71] Tabor, D., *Surface forces and surface interactions.* Journal of Colloid and Interface Science, 1977. **58**(1): p. 2-13.

[72] Rabinovich, Y.I., et al., *Adhesion between nanoscale rough surfaces: II. Measurement and comparison with theory.* Journal of Colloid and Interface Science, 2000. **232**(1): p. 17-24.

[73] Cooper, K., et al., *Analysis of contact interactions between a rough deformable colloid and a smooth substrate.* Journal of Colloid and Interface Science, 2000. **222**(1): p. 63-74.

[74] Gotzinger, M. and W. Peukert, *Dispersive forces of particle–surface interactions: direct AFM measurements and modelling.* Powder Technology, 2003. **130**(1): p. 102-109.

[75] Zhou, H., M. Götzinger, and W. Peukert, *The influence of particle charge and roughness on particle–substrate adhesion.* Powder Technology, 2003. **135**: p. 82-91.

[76] Fukunishi, A. and Y. Mori, *Adhesion force between particles and substrate in a humid atmosphere studied by atomic force microscopy.* Advanced Powder Technology, 2006. **17**(5): p. 567-580.

[77] Jones, R., et al., *Adhesion forces between glass and silicon surfaces in air studied by AFM: Effects of relative humidity, particle size, roughness, and surface treatment.* Langmuir, 2002. **18**(21): p. 8045-8055.

[78] Ripperger, S. and K. Hein, *Measurement of adhesion forces between particles and rough substrates in air with the vibration method.* Kona, 2005: p. 121.

[79] Shimada, Y., Y. Yonezawa, and H. Sunada, *Measurement and evaluation of the adhesive force between particles by the direct separation method.* Journal of pharmaceutical sciences, 2002. **92**(3): p. 560-568.

[80] Mizes, H., et al., *Small particle adhesion: measurement and control.* Colloids and Surfaces A: Physicochemical and Engineering Aspects, 2000. **165**(1): p. 11-23.

[81] Ding, W., *Micro/nano-particle manipulation and adhesion studies.* Journal of Adhesion Science and Technology, 2008. **22**(5-6): p. 457-480.

[82] Otsuka et al., *Measurement of the Adhesive Force between Particles of Powdered Materials and a Glass Substrate by Means of the Impact Separation Method. III.: Effect of Particle Shape and Surface Asperity.* Chemical & pharmaceutical bulletin, 1988. **36**(2): p. 741-749.

[83] Kulvanich, P. and P. Stewart, *Fundamental considerations in the measurement of adhesional forces between particles using the centrifuge method.* International journal of pharmaceutics, 1987. **35**(1): p. 111-120.

[84] Podczeck, F., *Optimization of the operation conditions of an Andersen-Cascade impactor and the relationship to centrifugal adhesion measurements to aid the development of dry powder inhalations.* International journal of pharmaceutics, 1997. **149**(1): p. 51-61.

[85] Czarnecki, J. and T. Dabroś, *Attenuation of the van der Waals attraction energy in the particlesemi-infinite medium system due to the roughness of the particle surface.* Journal of Colloid and Interface Science, 1980. **78**(1): p. 25-30.

[86] Rabinovich, Y.I., et al., *Adhesion between nanoscale rough surfaces: I. Role of asperity geometry.* Journal of Colloid and Interface Science, 2000. **232**(1): p. 10-16.

[87] Cooper, K., A. Gupta, and S. Beaudoin, *Simulation of the adhesion of particles to surfaces.* Journal of Colloid and Interface Science, 2001. **234**(2): p. 284-292.

[88] Rumpf, H. and F. Bull, *Particle technology*. Vol. 116. 1990: chapman and hall London.

[89] Butt, H.J. and M. Kappl, *Normal capillary forces.* Advances in colloid and interface science, 2009. **146**(1): p. 48-60.

[90] Ata, A., Y.I. Rabinovich, and R.K. Singh, *Role of surface roughness in capillary adhesion.* Journal of Adhesion Science and Technology, 2002. **16**(4): p. 337-346.

[91] Xiao, X. and L. Qian, *Investigation of humidity-dependent capillary force.* Langmuir, 2000. **16**(21): p. 8153-8158.

[92] Rabinovich, Y.I., et al., *Capillary forces between surfaces with nanoscale roughness.* Advances in colloid and interface science, 2002. **96**(1): p. 213-230.

[93] Nosonovsky, M. and B. Bhushan, *Capillary effects and instabilities in nanocontacts.* Ultramicroscopy, 2008. **108**(10): p. 1181-1185.

[94] Çolak, A., et al., *Surface adhesion and its dependence on surface roughness and humidity measured with a flat tip.* Applied surface science, 2012. **258**(18): p. 6938-6942.

[95] Ally, J., et al., *Detachment Force of Particles from Air− Liquid Interfaces of Films and Bubbles.* Langmuir, 2010. **26**(23): p. 18135-18143.

[96] Ally, J., et al., *Interaction of a microsphere with a solid-supported liquid film.* Langmuir, 2010. **26**(14): p. 11797-11803.

[97] Law, B. and F. Rieutord, *Electrostatic forces in atomic force microscopy.* Physical Review B, 2002. **66**(3): p. 035402.

[98] Bonaccurso, E., F. Schönfeld, and H.-J. Butt, *Electrostatic forces acting on tip and cantilever in atomic force microscopy.* Physical Review B, 2006. **74**(8): p. 085413.

[99] Quinn, D.B., J. Feng, and H.A. Stone, *Analytical Model for the Deformation of a Fluid–Fluid Interface Beneath an AFM Probe.* Langmuir, 2013. **29**(5): p. 1427-1434.

[100] Nan, L., et al., *Combined effect of surface tension, gravity and van der Waals force induced by a non-contact probe tip on the shape of liquid surface.* Chinese Physics Letters, 2005. **22**(8): p. 2012.

[101] Binnig, G., C.F. Quate, and C. Gerber, *Atomic force microscope.* Physical review letters, 1986. **56**(9): p. 930.

[102] Butt, H.-J., B. Cappella, and M. Kappl, *Force measurements with the atomic force microscope: Technique, interpretation and applications.* Surface science reports, 2005. **59**(1): p. 1-152.

[103] Ducker, W.A., T.J. Senden, and R.M. Pashley, *Direct measurement of colloidal forces using an atomic force microscope.* Nature, 1991. **353**(6341): p. 239-241.

[104] Hutter, J.L. and J. Bechhoefer, *Calibration of atomic-force microscope tips.* Review of Scientific Instruments, 1993. **64**: p. 1868.

[105] Eaton, P.J. and P. West, *Atomic force microscopy*. 2010: Oxford University Press New York.

[106] Bennett, H. and J. Porteus, *Relation between surface roughness and specular reflectance at normal incidence*. 1961, DTIC Document.

[107] Stover, J.C. and E.L. Hegstrom. *Scatter metrology of photovoltaic textured surfaces*. in *SPIE Solar Energy+ Technology*. 2010: International Society for Optics and Photonics.

[108] Farshchi-Tabrizi, M., et al., *On the adhesion between fine particles and nanocontacts: An atomic force microscope study.* Langmuir, 2006. **22**(5): p. 2171-2184.

[109] Heim, L.-O., et al., *Adhesion and friction forces between spherical micrometer-sized particles.* Physical Review Letters, 1999. **83**(16): p. 3328.

[110] Song, Y., et al., *Adhesion and friction properties of micro/nano-engineered superhydrophobic/hydrophobic surfaces.* Thin Solid Films, 2010. **518**(14): p. 3801-3807.

[111] Zhang, X., et al., *Adhesion and friction studies of microsphere-patterned surfaces in contact with atomic force microscopy colloidal probe.* Colloids and Surfaces A: Physicochemical and Engineering Aspects, 2012. **401**: p. 90-96.

[112] Burton, Z. and B. Bhushan, *Hydrophobicity, adhesion, and friction properties of nanopatterned polymers and scale dependence for micro-and nanoelectromechanical systems.* Nano letters, 2005. **5**(8): p. 1607-1613.

[113] Jallo, L.J., et al., *Prediction of inter-particle adhesion force from surface energy and surface roughness.* Journal of Adhesion Science and Technology, 2011. **25**(4-5): p. 367-384.

[114] Zhang, X., et al., *Tribological behavior of micro/nano-patterned surfaces in contact with AFM colloidal probe.* Applied surface science, 2011. **258**(1): p. 113-119.

[115] Ledesma-Alonso, R., D. Legendre, and P. Tordjeman, *Nanoscale deformation of a liquid surface.* Physical Review Letters, 2012. **108**(10): p. 106104.

[116] Forcada, M.L., M.M. Jakas, and A. Gras-Martí, *On liquid-film thickness measurements with the atomic-force microscope.* The Journal of chemical physics, 1991. **95**: p. 706.

[117] Bhushan, B., *Introduction to tribology*. 2013: Wiley. com.

VITAE

Name :Husam Mohammad Wahid Walwil

Nationality :Jordanian

Date of Birth :4/17/1988

Email :husam.mw@gmail.com

Address :KFUPM , Dhahran 31261,KSA

Academic Background

M.S (Mechanical Engineering)

Jan 2014

King Fahd University of Petroleum and Minerals,

Dhahran 31261, Saudi Arabia.

B.S (Mechanical Engineering)

Jan 2011

Birzeit University,

Ramallah, Palestine